Pion Absorption on Xenon in the Region of the $\Delta(1232)$ Resonance

by

Nikolas Kellogg Gregory

A.B. in Physics
Grinnell College
May 1990

S.M. in Physics
Massachusetts Institute of Technology
Sept 1995

Submitted to the Department of Physics
in partial fulfillment of the requirements for the degree of
Doctor of Philosophy
at the
MASSACHUSETTS INSTITUTE OF TECHNOLOGY
June 1999

Signature of Author ....
Department of Physics
May 13, 1999

Certified by ....
Robert P. Redwine
Professor of Physics
Thesis Supervisor

Accepted by ....
Professor Thomas J. Greytak
Professor
Associate Department Head for Education

Pion Absorption on Xenon in the Region of the $\Delta(1232)$ Resonance

by

Nikolas Kellogg Gregory

Submitted to the Department of Physics
on May 13, 1999, in partial fulfillment of the
requirements for the degree of
Doctor of Philosophy

Abstract

The absorption of π^+ mesons at 118, 162, and 239 MeV on Xenon has been studied using the Large Acceptance Detector System (LADS) at the Paul Scherrer Institute in Villigen, Switzerland. LADS has a solid angle coverage of over 98% of 4π steradians and an energy threshold of less than 20 MeV for protons, making it an excellent detector for studying multi-nucleon final states following $\pi^\pm$ absorption. The total absorption cross sections at the three energies are, in millibarns: 602 ± 140, 772 ± 150, and 668 ± 70. In addition, the breakup of the cross section into channels with different numbers of energetic final state nucleons has been determined.

Thesis Supervisor: Robert P. Redwine
Title: Professor of Physics

Acknowledgments

Too many people have influenced me and aided me in preparing me for writing this thesis to all be mentioned and all of them deserve thanks, but certainly some deserve special mention.

First, I would like to thank my parents Dick and Doree, who instilled in me the intellectual curiosity that led me to study physics.

I would like to thank my office mates, Jeff Martin, Taeksu Shin, Mark Sutter, Bryan Tipton, and especially Wilson Fong for his friendship during my tenure here at M.I.T. I owe Mark Sutter a debt for his willingness to be a sounding board for my data analysis ideas and for "proof-reading" my analysis. I also would like to thank my collaboration members on this side of the pond Kevin Wilson, Art Mateos and David Rowntree. You three have been a great aid to me in my graduate school career. David especially deserves mention for his help in formulating the uncertainties. On the other side of the pond I would like to thank Quentin Ingram, Albert Lehmann, for his discussions about the data, as well as his willingness to go eat *rosti* at any opportunity, and Danek Kotlinski, for his invaluable aid and wisdom in analyzing the heavy target data.

Bob Redwine deserves recognition for his patience with me as well as for the support that he has given me during the stay here at M.I.T.

Finally, I would like to thank my wife Laura. She has been especially tolerant and patient with me during my graduate student years and words cannot express my gratitude.

Contents

List of Figures

List of Tables

Chapter 1

Introduction

1.1 Discovery of the μ and π

The pion has been a particle of considerable interest ever since Hideki Yukawa [1] proposed the existence of a massive particle to be responsible for the nuclear force in analogy with the photon being the particle exchanged in the electro-magnetic force in 1935. While the EM potential has a $1/r$ behavior because of the exchange of a massless boson, the form of the potential is, with the exchange of massive boson,

$$\phi(r) \sim \frac{e^{-\frac{mc}{\hbar}r}}{r}. \tag{1.1}$$

From the distances involved in the strong force (~1fm), it is possible to estimate the mass of the exchanged particle. Solving the exponent in the equation above for m we obtain $m = \hbar c/1\text{fm} \approx 200\text{MeV}$. In addition, since Yukawa's particle was supposed to cover all nuclear interactions, it must also be responsible for beta decay.

In 1937 Anderson and Neddermeyer,[2] and Street and Stevenson[3, 4], measured a "penetrating" component of cosmic radiation. These particles did not follow the Bethe-Heitler theory of radiation. In fact, Anderson and Neddermeyer had to conclude that they had detected particles with the same charge as the electron, but with a mass that was in between that of the electron and the proton. Street and Stevenson saw similar effects and improved upon the Anderson and Neddermeyer results by determining that the mass of the particle causing the penetrating radiation was $130m_e \sim 70$ MeV.

Because the mass of this particle was close to the mass of the particle proposed by Yukawa, it was naturally identified with the Yukawa particle. All that remained was to confirm that this was indeed the sought-after particle responsible for the strong interactions between nucleons. In the early 1940s, it was shown by Tomonaga and Araki[5] that Yukawa particles should behave differently in matter depending on their charge. Specifically, the positive particles should come to rest in between the atoms in matter and decay, while the negative particles should be trapped in a very close orbit by the atoms in matter. Because the particles are supposed to be responsible for the nuclear force, the negative Yukawa particles would be absorbed by the nucleus long before they could decay in matter.

Evidence was mounting, though, that this newly discovered particle was not in fact the object hypothesized by Yukawa. The particle was interacting weakly at lower (sea level) altitudes in comparison with the apparent large production cross section at high (mountaintop) altitudes. The discovered particle was "dethroned" as the Yukawa particle when Conversi *et al.*[6] demonstrated that the particle did not behave according to the theory proposed by Tomonaga and Araki. Conversi and his collaborators found when the material in which the negative meson stopped was iron, that the negative particles did not decay (presumably the particles were absorbed by the Fe nucleus). When the material stopping the negative particles was carbon though, the negative particles did decay rather than be absorbed by a carbon nucleus.

In 1947 though, Lattes *et al.*[7] published the findings of photographic emulsion experiments done at 5500m in the Bolivian Andes and at 2800m in the Pyrenees. In these experiments, they found events in which one detected cosmic meson decays into another meson. The range of the secondary meson was nearly constant indicating a two-body decay of the primary meson. This decay was referred to as a μ-decay by Lattes *et al.* and the secondary mesons were represented by the symbol μ. The primary mesons were represented by the symbol π. Experiments on the π-meson demonstrated that it behaved very much like Yukawa's particle (except that it was not responsible for β-decay). The π-meson also decayed into a μ-meson and a neutrino. At the time of the pion's discovery, any particle which had a mass between that of the electron and the nucleon was referred to as a meson. In modern language, a meson is a strongly interacting boson and the μ in fact is part of the lepton family.

After the discovery of the charged pion, evidence was mounting that a neutral particle with a mass near that of the charged pion existed. The evidence was the increase in photon production during the bombardment of a beryllium target with protons in an experiment by Bjorkland *et al.*[8] and in a cosmic-ray photo emulsion experiment by Carlson *et al.*[9]. Direct confirmation of the two-photon decay of the neutral meson was obtained by Steinberger *et al.*[10]. The picture of the pion seemed to be more or less complete – *i.e.* an isospin 1 triplet.

1.2 Properties of the Pion.

After the discovery of the charged pion, one of the first properties to be measured was its mass which, while initially determined quite poorly, has now been measured to be 139.56995 ± 0.00035 MeV [Particle Data Booklet July 1998]. Early measurements were done by measuring the momentum and the energy of the charged pion. Later the mass of the π^+ was determined using $\pi \rightarrow \mu$ decay and more refined range measurements by Barkas *et al.* [11]. The earliest measurement of the π^- mass was also determined using a measurement of the energy of the γ in the reaction $\pi^- p \rightarrow n\gamma$ for mesic-hydrogen atoms by Panofsky *et al.*[12]. Similarly, the mass of the neutral pion was determined to be 135 MeV by measuring the energy of the gamma rays from the reaction $\pi^- p \rightarrow \pi^0 n$ [12]. The mass of the charged pion has since been measured with much greater precision using the atomic x-rays from the capture of a π^- on nuclei. See for example Jeckelmann *et al.*[13].

The boson nature of the π^- had been established by the processes $\pi^- p \rightarrow n\gamma$ and $\pi^- p \rightarrow n\pi^0$ occurring for the π^- at rest. The fact that the π^0 decays into two photons established that it has a spin of 0 or greater than 1. Still to be firmly established were the spin and the parity of the pion.

The parity of the charged pion was determined to be odd by examining the reaction of captured π^-s on deuterium ($\pi^- d \rightarrow nn$, $\pi^- d \rightarrow nn\gamma$, $\pi^- d \rightarrow nn\pi^0$). If $\pi^- d \rightarrow nn$ occurs, the π^- cannot be a scalar. This is because the initial state is $J^\pi = 1^+$ (the pion is absorbed in an s-wave orbital) and the Pauli principle requires that the neutrons be in a specific J=1 state ($^3P_1$), which has odd parity. Also, the π^0 should have the same parity as the charged pion if $\pi^- d \rightarrow nn\pi^0$ is not observed. This is due to the fact that the existence of a $^3P_1$ nn state simultaneous with a p-wave for the π^0 is suppressed because of phase space limitations.

As an aside, the parity of the neutral pion can be observed directly. A small fraction of the time a π^0 will decay via $\pi^0 \rightarrow \gamma\ e^- e^+$, with the pair of electrons being called a Dalitz pair. An even smaller fraction of the time, a π^0 will decay into two Dalitz pairs. By studying the correlations of the planes of Dalitz pairs, it is possible to directly measure the parity of the π^0. This was done in 1959 by Plano *et al.*[14].

The spin of the charged pion was determined using the principle of detailed balance and was done by measuring the reaction $\pi^+ d \to pp$, and measuring the inverse reaction $pp \to \pi^+ d$. Detailed balance then relates the two cross sections at the same center-of-mass energy in the center-of-mass system by the relation

$$\frac{d\sigma_{pp\to\pi^+ d}}{d\Omega} = \frac{(2S_d+1)(2S_\pi+1)q^2}{(2S_p+1)^2 p^2}\frac{d\sigma_{\pi^+ d\to pp}}{d\Omega}, \tag{1.2}$$

where S_π, S_p, and S_d are the spins of the pion, proton and deuteron respectively, p is the momentum of either proton, and q is the momentum of the pion of the πd system as suggested by Marshak[15] and Cheston[16]. This was done by Clark *et al.*[17] and Durbin *et al*[18], which fixed the spin of the charged pion at 0.

What resulted from of all this early experimental work is that the pion is a pseudoscalar (spin 0, odd parity) isospin triplet consisting of π^+, π^0, π^-. The pion's properties are summarized in Table 1.1.

Properties of the Pion					
Pion	J^π	T	Mass (MeV/c^2)	Mean Life (sec)	Decay Mode
$\pi^\pm$	0^-	1	139.567	2.6×10^{-8}	$\mu\nu_\mu$ 99.9%
π^0	0^-	1	134.974	8.4×10^{-17}	2γ 98.8%

Table 1.1: Fundamental properties of the pion.

Properties of the Δ					
	J^π	T	Mass (MeV/c^2)	Width(MeV)	Decay Mode
Δ	$\frac{3}{2}^+$	$\frac{3}{2}$	1232	120	$N\pi$ 99.4%

Table 1.2: Fundamental properties of the $\Delta(1232)$.

1.3 Pion–Nucleon Interactions

To first order, the pion in the nucleus can be thought of as interacting with individual nucleons. That is, the quasi-free approximation is made. To make predictions, the πN interaction on free nucleons must be understood. In the intermediate energy region (80-300 MeV), the most prominent feature is the $\Delta(1232)$ resonance. In the quark picture of the nucleon, the Δ is the first excited state and corresponds to a spin flip of one of the constituent quarks resulting in an isospin 3/2 ($T = 3/2$), spin 3/2 ($J = 3/2$) state of the nucleon. The properties of the Δ are summarized in Table 1.2.

In the intermediate energy regime, the Δ dominates the πN interaction and allows for several predictions. First, if one decomposes the following reactions

$$\sigma(\pi^+p \to \pi^+p) : \sigma(\pi^-p \to \pi^-p) : \sigma(\pi^-p \to \pi^0n), \tag{1.3}$$

into isospin channels as follows,

$$\sigma(\pi^+p \to \pi^+p) = f_{3/2}^2, \tag{1.4}$$

$$\sigma(\pi^-p \to \pi^-p) = \frac{4}{9}f_{1/2}^2 + \frac{1}{9}f_{3/2}^2, \text{ and} \tag{1.5}$$

$$\sigma(\pi^-p \to \pi^0n) = \frac{2}{9}f_{1/2}^2 + \frac{2}{9}f_{3/2}^2, \tag{1.6}$$

where f_T is the scattering amplitude for a state with isospin T, then at the resonance, the $T = \frac{1}{2}$ can be ignored and one obtains the ratio $\sigma_{\pi^+p\to\pi^+p} : \sigma_{\pi^-p\to\pi^-p} : \sigma_{\pi^-p\to\pi^0n}$ of 9:1:2. Figure 1-1 shows the cross sections for the above reactions. The solid lines are the calculated contributions from the $\Delta(1232)$ resonance.[19]

Second, assuming that the π^+p scattering occurs in an isospin 3/2 state, the cross section can be predicted at the resonance and should be equal to

$$\sigma(j,l) = 2\pi\left(\frac{\hbar}{q_{cm}}\right)[2j+1], \tag{1.7}$$

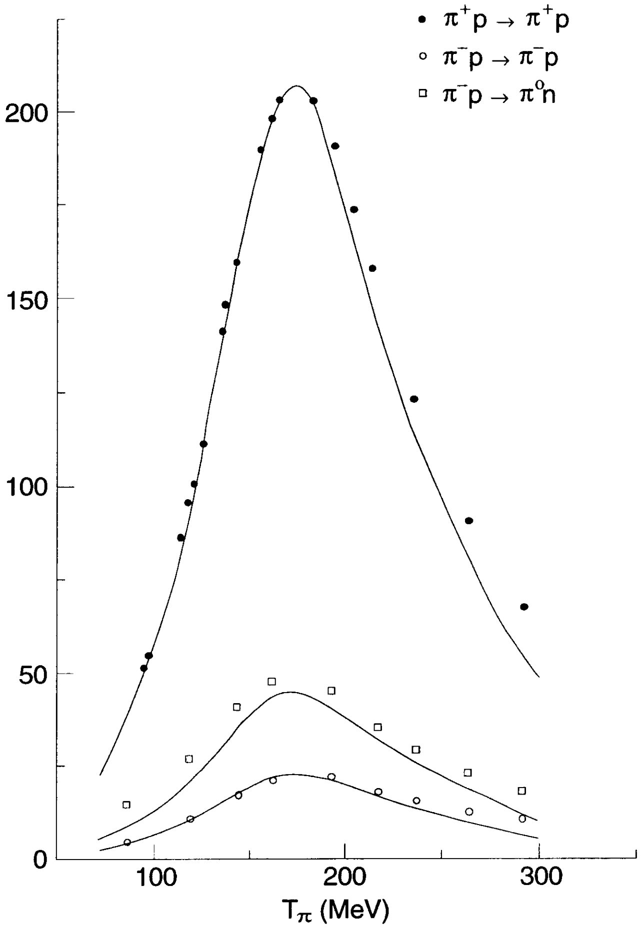

Figure 1-1: The energy dependence of the πN cross section. From Moniz [19].

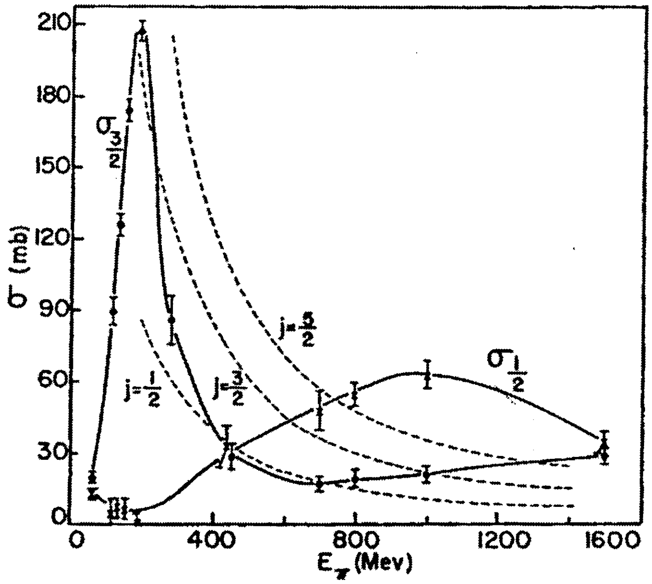

Figure 1-2: The experimental values for πN scattering in the states of pure isospin 1/2 and 3/2. The dashed curves represent the upper limits on the cross sections for scattering in pure states (j, l) as given by equation 1.7. From Gell-Mann and Watson.[20]

where q_{cm} is the momentum of the pion in the $\pi - N$ CM system and j is the angular momentum of the Δ.[20] The expected cross section is 190 mb, which is quite close to the experimentally observed cross section (see Figure 1-2).

Finally, because the Δ resonance dominates πN scattering processes for pion kinetic energies less than 300 MeV, it is possible to predict the shape of the πN differential cross section near the energy of the Δ resonance. If one assumes that the scattering follows the process $\pi + N \rightarrow \Delta \rightarrow \pi + N$, then, due to angular momentum considerations, the spatial wave function must be proportional to the $l = 1$ Legendre polynomial and the differential cross section near the resonance therefore has the form

$$\sigma(\theta_{CM}) \propto 1 + 3\cos^2\theta_{CM}. \tag{1.8}$$

1.4 Pion–Nucleus Interactions

Once the pion has more than an individual nucleon with which to interact, many more reaction channels are available and the total pion interaction cross section can be decomposed in the following manner:

$$\sigma_{total} = \sigma_{el} + \sigma_{inel} + \sigma_{CEX} + \sigma_{rad} + \sigma_{abs}, \tag{1.9}$$

where σ_{el} is the cross section for elastic scattering and refers to the process in which the pion scatters from the entire nucleus. σ_{inel} is the cross section for inelastic scattering and refers to processes where the pion loses energy in the interaction (*e.g.* quasi-elastic scattering from an individual nucleon or pion induced pion production). Charge-exchange, σ_{CEX}, refers to the processes in which the charge states of the initial and final pion differ. Absorption processes, σ_{abs}, are processes in which there is no pion in the final state. Finally, radiative reactions, σ_{rad}, refer to those processes in which a photon is emitted as a direct consequence of pion reaction process. The radiative reactions are important in light nuclei for stopped pion capture, but can usually be ignored in the reactions of pions in flight.

1.4.1 Pion Absorption on the Deuteron

Energy and momentum conservation forbid the absorption of a pion on a free nucleon. Even within the nucleus the absorption on a single nucleon is strongly suppressed because the momentum required by the nucleon ($\sim$ 500MeV) is much greater than typical nucleon momenta in the nucleus. The smallest system on which the pion can be absorbed is a system of two nucleons and the only bound state with two nucleons is the deuteron.

The reaction $\pi d \rightarrow pp$ is quite well measured experimentally and there are at least 200 experimental results for the reaction below 1 GeV. Two main features characterize the total pion absorption cross section: one feature is the large peak at an incident pion kinetic energy of about 140 MeV due to the Δ resonance; the other is the rise of the cross section near threshold. In fact, the data can be modeled quite well simply by incorporating these two main features and including a small normalization offset, which was done by Ritchie[21]. An improvement of the parameterization which takes into account an enhancement in the cross section around 800MeV incident pion kinetic energy was also done by Ritchie[22].

1.4.2 Pion Absorption on Nuclei – Early Work

In *Meson Physics*[23], written by Marshak and published in 1952, the early work on the properties of what then were called mesons (both μ and π) was presented. Besides the initial confusion of the μ with Yukawa's particle, in these early years much work was devoted to simply understanding the nature of the pion. While quite a bit of good work was done, the limiting factor was the lack of good pion sources. Machines at Columbia, Berkeley, and Cornell produced lower energy ($T_\pi \leq 100\text{MeV}$) pion beams. The source for higher energy beams was cosmic rays which, in addition to poor beam definition, had essentially no energy definition. Therefore, experiments using "natural" pion sources tended to look for characteristics like total elastic and total inelastic cross sections.

Because of the low intensity beams from accelerators as well as the relatively low reaction cross sections for pions in flight, many of the early pion experiments were done on stopped pions. Specifically, a low energy π^- would be captured by a nucleus in a high energy orbit, decay down to lower orbits through the emission of x-rays and Auger electrons and eventually would be absorbed by the nucleus with the resulting release of the pion's rest energy.

Most of the stopped pion experiments also were done in photographic emulsions and the absorption of a pion usually resulted in a "star" of charged particles whose identity and energy would then be determined. The photographic emulsion work was done by

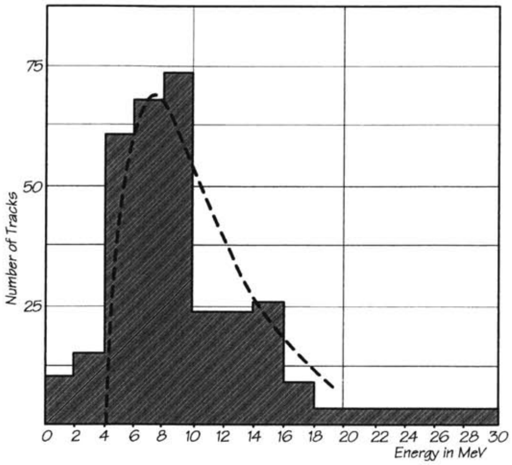

Figure 1-3: The distribution of protons with energy $<$ 30 MeV following stopped pion absorption in photographic emulsion. The data are from Ref. [27]. The line is from evaporation theory.

Perkins[24], Adelman and Jones[25], Cheston and Goldfarb[26], Menon *et al.*[27], and Adelman[28]. The frequency distribution of the number of prongs for each star gave an average number of charged particles per star to be 1.6, suggesting a multi-nucleon absorption process as absorption on a *pn* or *pp* pair would emit 0 or 1 charged particles respectively. Analysis of the proton energy spectrum from the emulsion work revealed that it could be fit by the spectrum produced by the evaporation of nucleons from a nucleus with $\sim$ 100MeV of excitation (see Figure 1-3). What was not determined in the early emulsion studies was whether the entire nucleus shared the energy of the absorbed pion or whether the nucleus was left in an excited state after the emission of one or two higher energy neutrons. Two of the experiments, Adelman[28] and Chester and

Goldfarb[26], however, observed higher energy protons $T_p > 30$ MeV, whose abundance could not be explained by the high energy tail from the evaporation spectra. Both experiments observed that about 10% of the π^- absorption events led to the high energy protons indicating (in today's understanding) absorption on a pp pair.

The other studies done during this period with stopped mesons were the investigations of the nature of the absorption of the stopped pion. The processes considered were hadronic absorption (what is now called pion absorption *i.e.* $\pi^- d \rightarrow nn$), radiative absorption (emission of a high energy photon *i.e.* $\pi^- d \rightarrow nn\gamma$), and mesic absorption (what is now called charge exchange *i.e.* $\pi^- d \rightarrow nn\pi^0$). In the experiments by Panofsky[12], it was determined that about 2/3 of the absorptions were hadronic and 1/3 were radiative and essentially none were from mesic absorption. This was not unexpected from parity considerations as mentioned earlier in Section 1.2. In heavier nuclei such as carbon, the upper limit for radiative absorption of stopped negative pions was determined to be about 1%.[29, 23] In addition, on heavier nuclei, mesic absorption of stopped pions when not forbidden by energy considerations was greatly suppressed due to phase space considerations because of the small amount of kinetic energy available to the π^0.

The studies of the reactions of pion in flight should not be dismissed as unhelpful. In fact, the first measurements of the $\pi^+ d \rightarrow pp$ absorption cross section by Clark *et al.*[17] and Durbin *et al.*[18] were what established that the spin of the charged pion was zero. Also, work done by Bernardini *et al.*[30, 31] on π^- absorption in photographic emulsion for pion energies up to 110 MeV indicated that pion absorption was increasing in importance relative to elastic scattering as the incident pion energy increased. Bernardini and Levy[32] determined, in an emulsion experiment with 70 MeV π^+, that the average number of prongs per star was 3.2, a difference from the 1.6 prongs per star for the π^-. This result was not totally unexpected as the conversion of one of the neutrons to a proton from the absorption of the π^+ would bias the results to a visible star. Bernardini *et al.* found in the π^- data that 85% of the stars had a proton which carried away > 30 MeV and that 30% of the tracks had two protons of energy > 30 MeV, an indication that more than two nucleons were involved in pion absorption.

Finally, an interesting result from the early accelerator experiments was the measurement of the total pion reaction cross section. Bernardini *et al.*[31] and Bradner and Rankin[33] determined that, with respect to pion interactions, the nucleus behaved like a black disk – *i.e.* the cross section was geometrical. This result implied that the mean free path of the pion was small in comparison to the nuclear size when in nuclear matter.

1.4.3 The Development of Two Nucleon Absorption (2NA) Dominance

The period of time from 1953 until 1969 saw the refinement of experimental techniques and a move away from photographic emulsion studies to experiments with bubble cham-

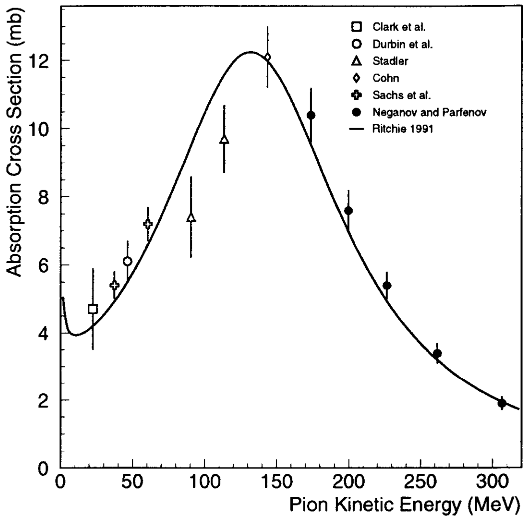

Figure 1-4: The total absorption cross section on ^{2}H for π^+ of various energies. The data are from Refs. [35, 36, 37, 38]. The line is the parameterization by Ritchie[22].

bers and cloud chambers with better statistics and to experiments with counters "tuned" to investigate specific particle emissions following pion absorption. This period of time is reviewed by Koltun [34].

Continuation of the work started by Clark *et al.*[17] and Durbin *et al.*[18] was done by several groups which helped to establish the nature of pion absorption through the study of the deuterium absorption cross section in the late 1950s [35, 36, 37, 38]. These works established the existence of a broad resonance peaking around 140 MeV, which has since been extensively studied, and as stated earlier, has been parameterized by Ritchie[22] (see Figure 1-4). In 1958, Neganov and Parfenov[38] published the results of a counter experiment which was done with enough precision to determine that the differential cross section had the form $d\sigma/d\Omega = A + B\cos^2\theta$.

Experiments during this period, though, were still primarily done with stopped pions as the quality of pion beams had not yet improved enough to provide stable high fluxes to readily allow studies of the absorption of pions in-flight. Obviously though, the π^+ experiments were done in-flight. The emulsion and photographic studies of the late 1950s and early 1960s on stopped pions forwarded the work of the early 1950s in that the experiments tended to focus on the classification of "stars" and "prongs". An example is that Demeur *et al.*[39] found that 35% of the events were not associated with any fast particles "prongs" detected, indicating that the energy was carried away by neutral particles. The emulsion experiments could generally distinguish between absorption on "light" (C, N, and O) nuclei and "heavy" (Br and Ag) nuclei. Demeur *et al.*[39] found that the most probable number of emitted fast charged particles was 3 for light nuclei and 1 for heavy nuclei. While Demeur *et al.* and the Azimov *et al.*[40] emulsion work agree on the most probable number of charged particles, they do not agree on the actual distribution of prong number.

One of the problems with the "star" experiments was that they could separate the different charge species but not isotopes. Therefore p, d, and t were all classified as "protons" and Demeur *et al.*[39] in a bubble chamber experiment estimated that 20% of the light nuclei break up into "protons" and alphas only (*i.e.* complete disintegration). This is somewhat inconsistent with the results of Ammiraju and Lederman[41] who studied C and N separately in a diffusion cloud chamber. They found that at least 30% of the light nuclei disintegrate into protons and alphas (and neutrons). Yet another later experiment, this one in diamond layers in emulsion by Fedotov[42], found the number to be about 60%. Clearly there were large uncertainties with numbers extracted from photographic studies and the results from earlier photographic analyses generally allowed for qualitative conclusions only.

The improvements in the middle to late 1960s of both experimental techniques and beam intensity allowed for quantitative conclusions from bubble chamber and emulsion experiments including particle identification and the angular correlation of particles involved in an absorption. The volume of photographs which had to be analyzed to provide adequate statistics tended to affect the accuracy of the results, especially for higher energy particles (e.g protons $>$ 60 MeV), though there were several measurements of proton [40, 42] and neutron [43, 44] spectra for lower energy particles.

Experiments with counters allowed for better statistics as well as higher particle energies. Anderson *et al.*[45] had one of the most complete experiments during this period. Using neutron time-of-flight counters, Anderson *et al.* obtained neutron spectra with neutron energies up to 130 MeV for stopped π^- in C, Al, Cd, Pb, and U. They found that the mean number of neutrons per absorption rose from 2.8 for Carbon to 5.0 for Uranium. Based on a statistical theory of nucleon emission by Le Couteur[46, 47], the spectra at very low energies could be fit assuming it was the result of nucleon evaporation from a nucleus of temperature θ using:

$$N(E_n) \propto E_n^{5/11} e^{-E/\theta}. \tag{1.10}$$

Anderson *et al.* found values for θ of 1.7 – 3.1 MeV, depending on the nucleus. After subtracting the evaporation spectra, the mean number of neutrons emitted per absorption was about 2 for all targets. If the energy spectra of the neutrons are plotted the high energy shape is consistent with an exponential dependence (see Figure 1-5).

Similarly, the high energy spectrum of single protons with $E_p \leq 100$ MeV following the absorption of a stopped π^- on ^{16}O, measured by Fowler[48], was consistent with an exponential dependence. In fact both the neutron and the singles protons spectra were consistent with $N(E) \propto \exp(-E/E_0)$ with $E_0 = 45$ MeV (see Figure 1-6). The singles spectra indicated that the absorption process, perhaps, was statistical with the blip being the mean number of emitted neutrons per absorption determined in Anderson *et al.*

While it would be extremely interesting today if there were strong evidence that the energy of the absorbed pion was shared equally with the entire nucleus in view of the fact that the pion is strongly interacting, very early emulsion studies [24] already fueled

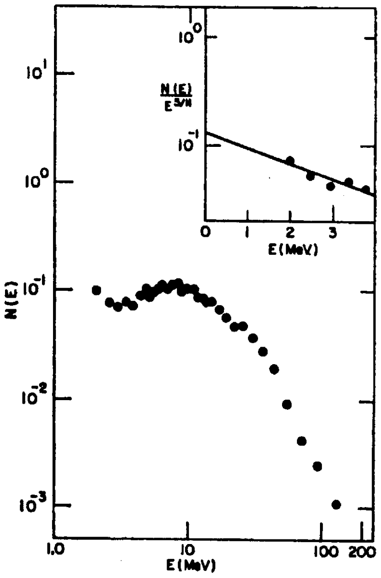

Figure 1-5: Log-log plot of the neutron energy spectrum from carbon. The inset is a semi-log plot of the low energy part of the spectrum divided by $E^{5/11}$. From Ref. [45]

discussion that some sort of two-nucleon absorption(2NA) process might play a large role in π absorption.

Further establishing a two-nucleon nature of pion absorption, the counter experiment of Ozaki *et al.*[50] on stopped π^- on Carbon and Aluminum examined nn and pn pairs. They found that nn pairs were more probable than pn pairs by a ratio of 4 in Aluminum and 5 in Carbon indicating (in today's understanding) the enhancement of absorption on T=0 pairs over T=1 pairs. They also found that the nucleon pairs were much more likely to be emitted with a relative angle of 180° rather than 90°, again indicating the sharing of energy by only two nucleons.

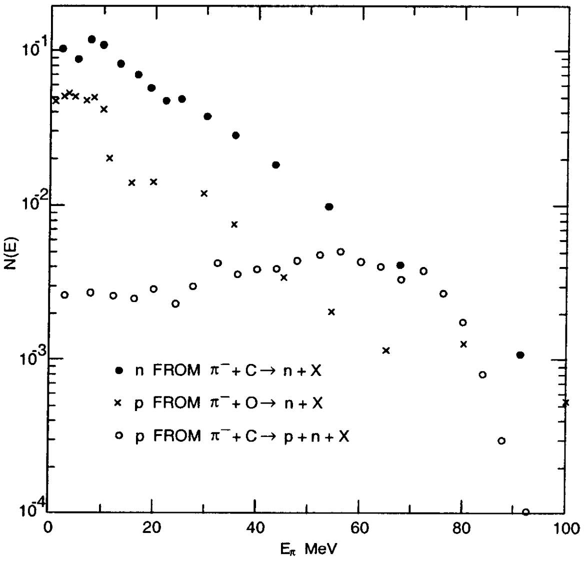

Figure 1-6: Semi-log plot of the energy of the emitted particles following stopped pion absorption. The closed circles form the singles neutron spectra from Ref. [45]. The crosses form the singles proton spectra from Ref. [48]. The open circles form the *pn* coincidence spectra from Ref. [49].

Evidence of 2NA also presented itself in studies of absorption of pions in flight. Balandin *et al.*[51], for example, measured the mean number of protons (in reality p, d, or t) in a bubble chamber experiment for $\pi^{\pm}$ on carbon with $E_{\pi} \sim 40 - 70$ MeV and obtained 2.2 "protons" per absorption for π^{+} and 1 proton for π^{-}.

Another stopped pion experiment (Nordberg *et al.*[49]) used counters to measure the nn and pn emission in a stopped π^{-} on many nuclei. They also obtained proton energy spectra for absorption on ^{12}C and ^{16}O. The peaks of these spectra were located at about 60 MeV (1/2 of the energy available from the absorption of the pion) (see Figure 1-6). Nordberg *et al.* also produced relative angular distributions and found a strong peaking at $\Delta\theta = 180°$. They also found that absorption on a pn pair was at least twice as likely as absorption on a pp pair and that emission of a correlated nn or pn pair accounted for 20-80% of the absorption in light nuclei.

Investigations of absorption of pions in flight also produced evidence that the energy and momentum of the absorbed pion was shared by two nucleons. One emulsion experiment by Afanasev and Ostrumov, in 1965[52], found that for the reaction $^{14}\mathrm{N}(\pi^{+}, 2p)3\alpha$ at pion energies of 70-80 MeV the distribution of the relative lab angle of the two protons was peaked at 140°. Also, because Afanasev and Ostrumov detected all of the charged particles emitted, the mean energy of the 3α system could be measured. They found that the mean energy of the 3α system corresponded to an excitation of 13 MeV. Clearly then, most of the energy of the system was carried off by the protons. In fact, they found that the momentum of the $2p$ system favored the direction of the incoming π^+.

Several experiments in the mid-to-late 60s by Charpak *et al.*[53, 54, 55, 56] and Burman and Nordberg[57] improved upon the counter experiments investigating the absorption of pions in flight by measuring not only the direction of emitted particles but the momenta as well. In addition, Davies *et al.* performed a neutron time-of-flight experiment.[58] These experiments investigated differential quantities like missing mass (the energy of the residual nucleus)[54, 58, 57] and it was found that in general the ground-state of an A-2 nucleus is readily distinguished from excited states.

While a very definite picture was emerging as to the nature of pion absorption, absorption on a $2N$ pair, there was some muddying of the waters. In 1965, Vaisenberg *et al.*[59] published the results of an experiment which presented evidence of absorption modes other than $2N$. They were able to separate, in an emulsion experiment, the emitted protons, deuterons and tritons. What was seen was a sizable fraction of deuterons and tritons which was interpreted as evidence for π absorption on α-particles.

A slightly later experiment by Witten *et al.*[60] measured the spectrum on high energy protons (E_p >140 MeV) from the absorption of 68 MeV π^+ on carbon, finding a peak in the spectrum at E_p =180 MeV. The maximum proton energy was $\sim$ 190 MeV, leaving the residual ^{11}B in its ground state. The peak was interpreted as single nucleon absorption on the $p_{3/2}$ shell of ^{12}C.

1.4.4 The Advent of the Meson Factories

The investigations into pion absorption were about to take a turn for the better in the 1970s. At the beginning of this decade the pion factories were just coming online, promising stable, monochromatic, high-intensity pion beams. These facilities were (in order of appearance) the Los Alamos Meson Physics Facility (LAMPF) - based on an 800 MeV proton linear accelerator, the Tri-University Meson Facility (TRIUMF) - based on a 520 MeV proton cyclotron, and the Swiss Institute for Nuclear Physics (SIN), now known as the Paul Scherrer Institute (PSI) - based on a 590 MeV proton cyclotron. These machines promised and delivered meson beams of unprecedented quality. The early half of the decade is reviewed well (if in overly flowery language) by J. Hüfner[61] in 1975.

During this period, experimental techniques improved to an extent that statistically significant measurements of many differential quantities could be done. In the Favier *et al.*[62] experiment, one of the first benefitting from the improved experimental techniques, the authors performed a survey of two-nucleon absorption over numerous nuclei at an incident pion kinetic energy of 76 MeV, and determined differential quantities such as missing mass, recoil momentum, recoil angle and Treiman-Yang angle.

For the Favier *et al.* study, the missing mass ΔM_R, which is also the excitation energy of the residual system, was defined as the mass of the residual $A-2$ system minus the minimum possible mass for such a system (bound state or free $A-2$ nucleon system):

$$\Delta M_R = [(E_\pi + M_A - E_{p_1} - E_{p_2})^2 - (\vec{p}_\pi + \vec{p}_{p_1} + \vec{p}_{p_2})^2]^{\frac{1}{2}}, \tag{1.11}$$

where $E_i^2 = m_i^2 + p_i^2$ etc. is the total energy of particle i. The Treiman-Yang angle was defined in the system where the incoming pion is at rest as follows:[63]

$$\cos\phi_{TY} = \frac{(\vec{p}_A \times \vec{p}_R) \cdot (\vec{p}_1 \times \vec{p}_2)}{|\vec{p}_A \times \vec{p}_R||\vec{p}_1 \times \vec{p}_2|}, \tag{1.12}$$

where $\vec{p}_A$ and $\vec{p}_R$ are the vectors of the target and residual system in the pion's rest frame and $\vec{p}_1$ and $\vec{p}_2$ are the vectors of the outgoing nucleons in the pions rest frame. The Treiman-Yang defines the angle between the plane defined by the target and residual system and the plane defined by the outgoing nucleons. The distribution in the Treiman-Yang angle will be isotropic if the two nucleon absorption picture holds. Specifically, if one of the following applies: 1. The two-nucleon cluster is spin zero; 2. the two-nucleon cluster is in an s-state relative to the rest of the nucleus, ϕ_{TY} will be isotropic. As such, the Treiman-Yang angle is a useful tool for investigating the importance of two-nucleon absorption.

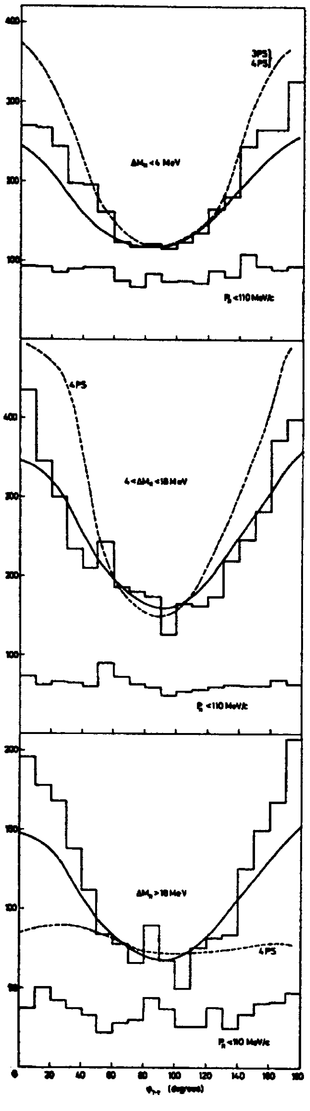

Figure 1-7: The Treiman-Yang angle for the absorption of 76 MeV π^+ on ^{4}He. The dashed curve is phase space, the solid curve is theory from Ref. [64]. The three plots show ϕ_{TY} for various values of ΔM_R. All lines are arbitrarily normalized. From Favier *et al.*[62]

Favier *et al.* measured ϕ_{TY} for numerous targets. The results for ^{4}He are shown in Figure 1-7. The data are compared with phase space and theory curves from Lazard *et al.*[64] as well as plotted for $p_R < 110 MeV/c$. Geometry limited the acceptance for the high recoil momentum data so it must be compared with predictions. The low recoil momentum data do indeed appear to be flat, consistent with quasi-free two-nucleon absorption. The fact that the theory curve fits the data better than phase space was taken as an indication that initial- and final-state interactions are important.

Also plotted in Favier *et al.* were missing mass spectra for the nuclei studied which are shown here in Figures 1-8 and 1-9. Peaks corresponding to absorption on different shells of the target nuclei are seen in the data. Particularly interesting is the missing mass spectra of ^{6}Li, which is shown in Figure 1-8. Very clearly seen is the peak corresponding to absorption on a loosely bound quasi-deuteron, leaving ^{4}He in the ground state, which is located at $\Delta M_R = 0$ MeV. The peak at $\Delta M_R \sim 20$ MeV may correspond to absorption with at least 1 nucleon in the s-shell or, if modeling ^{6}Li as a d-cluster bound to an α-cluster in a relative s-state, this peak appears to be absorption on the α.

Figure 1-9 shows the missing mass spectra for various heavier nuclei. Again, there typically is a strong peak corresponding to leaving the residual nuclei in the ground state. The right side of the figure has the missing momentum p_R limited to less than 110 MeV/c and the data are compared to calculations by Balashov *et al.*[65] (dashed curves) of the

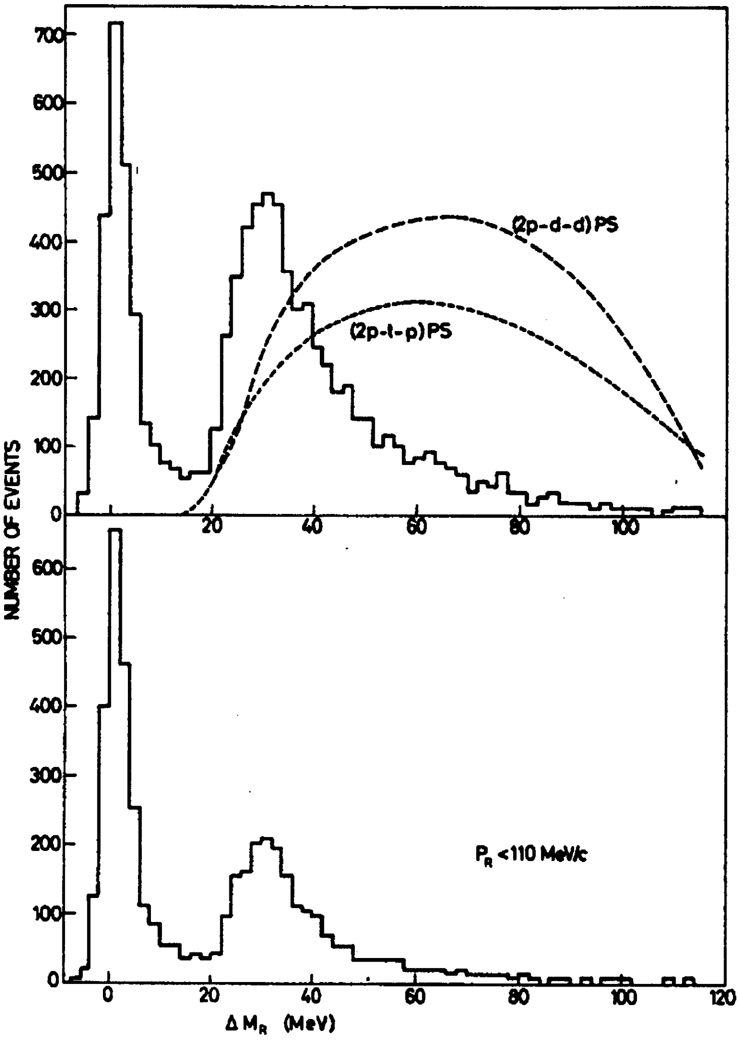

Figure 1-8: The missing mass spectra of ^{6}Li($\pi^+, 2p$)^{4}He with respect to the ground state of ^{4}He. The top figure does not have p_R limited. The lower figure is for $p_R < 110$ MeV/c. From Favier *et al.*[62]

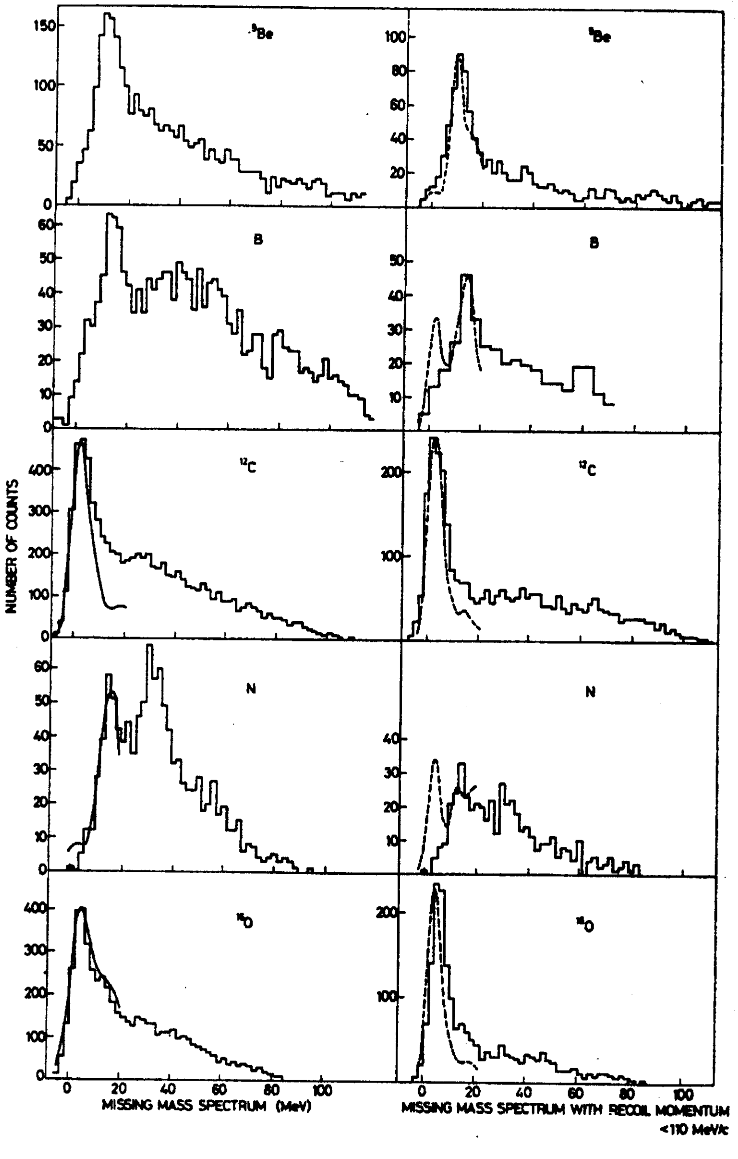

Figure 1-9: The missing mass spectra for $(\pi^+, 2p)$ on Be, B, C, N, and O with respect to the ground states of the residual nuclei. The right side has the restriction $p_R < 110$ MeV/c, the left side does not. From Favier *et al.*[62]

effective number of deuterons with $L = 0$ folded with their resolution function. The left side has no restriction on p_R and the data are compared to calculations by Kopaleishvili *et al.*[66, 67], again folded with their resolution function. Both theoretical curves are arbitrarily normalized.

At this stage of pion absorption experiments, the hope was to use pion absorption in a manner similar to electron scattering to obtain information on the structure of the nucleus. Therefore, for Favier *et al.*, the most interesting events were the quasi-free absorption events, but they did have indications of more goings-on. Either initial-state interactions of the pion or final-state reactions within the target nuclei could be the cause of the degradation of the missing mass spectra with increasing A. Since the more complicated events could not help with understanding the structure of the nucleus, they constituted an "annoying background". Of course, it is these events that currently are of so much interest, which is discussed below.

In 1973, Bellotti *et al.*[68] published the results of a bubble chamber experiment investigating the absorption of 130 MeV π^+ on carbon. This work was the first to measure a total pion absorption cross section with any precision, and arrived at a value for absorption on carbon of 189 ± 19 mb. This number is about 50% of the total inelastic cross section. Bellotti *et al.* also attempted to determine the branching ratios for the absorption process. Most interestingly, they found that only about 10% of the absorption cross section comes from undisturbed QFA. An additional 10% or so comes from QFA where a significant amount of energy is imparted to the residual nucleus, with the rest coming from some other process or processes. The authors presumed that it was absorption on an α cluster. What is not determined is how the pion is absorbed on the α; the nature of bubble chamber experiments prevents this. Another difficulty with interpreting the total absorption cross section is that the $0c$ and $1c$ prongs were not included in the analysis because of SCX contamination and it is not clear whether this was included in their error bar.

In an effort to better understand the absorption process, Jackson *et al.* performed a single-arm experiment with 100- and 200- MeV $\pi^{\pm}$ on Al, Ni and Ta targets.[69] They found that the proton spectra were similar for both π^+ and π^- with a ratio of absolute yields of ~3:1. Jackson *et al.* also found that the yields followed an $A^{2/3}$ dependence except for an anomaly at 100 MeV at forward angles where the target dependence was closer to $A^{1/3}$. While there is no explanation for the 100 MeV anomaly, there were two explanations offered for the 3:1 σ_{π^+}:σ_{π^-} ratio. One is that absorption on a T=1 pair is favored; the other is that absorption occurred not on a two nucleon pair, but rather on a more complex object. For example the 3:1 ratio would occur naturally if the process were $\pi + \alpha \rightarrow 4N$.

1.4.5 The Modern Era of Pion Absorption and the Investigation of Multi-Nucleon Absorption Processes

The modern period of pion absorption is discussed in several reviews including those by Ingram [70] and Redwine [71] who cover the general state of pion interactions with nuclei for the years up to the mid 1980s, the reviews of Ashery[72] and Weyer[73] who cover pion absorption specifically, and a book by Ericson and Weise [74] which covers the entire topic of pion physics in great detail. What emerged from the earlier studies of pion absorption studies is a picture of pion absorption consisting of mostly a two-nucleon process that is isospin dependent. While the focus had shifted during the previous decade from using pion absorption as a probe of nuclear structure to investigating directly the nature of pion absorption with nuclear matter, it was still believed that an understanding of pion absorption (2NA with possibly ISI and/or FSI messing things up a bit) was obtainable in short order. This was about to change.

In 1980, McKeown *et al.*[75] published the results of an experiment measuring the number of nucleons involved in pion absorption on targets ranging from carbon to tantalum by measuring the proton singles spectra. Taking a cue from particle and heavy-ion physics, the experimenters performed a rapidity analysis of their data to determine the total mass of the absorbing system. Rapidity is a measurement of the velocity of the proton parallel to the incident beam and is defined as follows:

$$y \equiv \tanh^{-1} \beta_{\|} = \tanh^{-1} \frac{p_{\|} c}{E}. \tag{1.13}$$

When y is plotted against $p_{\perp}$, the perpendicular component of the proton's momentum, it is expected that contours of constant cross section will be symmetric around a value of $y{=}y_0$, which corresponds to the number of nucleons involved in the process by assuming that y_0 represents the velocity of the center of mass of the pion plus the nucleons which are involved in the absorption. y_0 is determined as follows:

$$y_0 = \tanh^{-1} \beta_{c.m.} = \tanh^{-1} \frac{p_\pi c}{E_\pi - M_{abs} c^2}, \tag{1.14}$$

where $M_{abs} = MN$, N being the number of nucleons involved.

Performing this type of analysis (see Figure 1-10) McKeown *et al.* determined that the number of nucleons involved rose from about three on carbon to almost six on tantalum. Figure 1-11 shows the number of nucleons involved averaged over the incident pion energies. These results could not be explained by a process involving only two nucleons causing the question of the process of pion absorption to be opened once again. There are at least two difficulties with the analysis. First, to extract the number of nucleons involved, the rapidity plot must be symmetric about the determined value of y_0, which

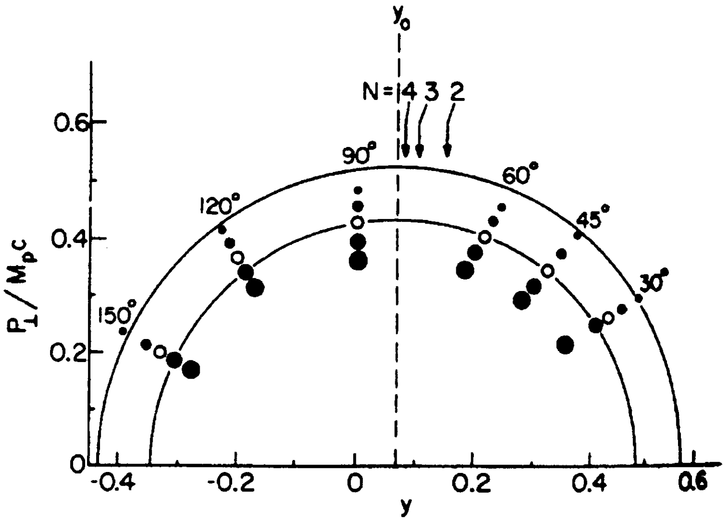

Figure 1-10: Rapidity Plot for 220 MeV π^- on ^{181}Ta. From McKeown *et al.*[75].

it was not, although the reported error bars incorporate the asymmetry. Second, it is difficult to correct for the number of charged particles involved, because the measurement was done using a single-arm small solid angle system. As a gross example, suppose that the process consists of only two modes, one involving 3 protons, the other involving 100 protons. Also assume that both modes are isotropic and equally likely, then the 100 proton mode would be seen about 30 times more often than the 3 proton mode, skewing the multiplicity results since one can not *a priori* correct for the different modes.

Also measured in the early 80s were the total absorption cross sections in work by Nakai *et al.*[76], Navon *et al.*[77] and Ashery *et al.*[78] (see Figure 1-12). Nakai *et al.*'s work measured the total absorption cross section by detecting the nuclear γ-

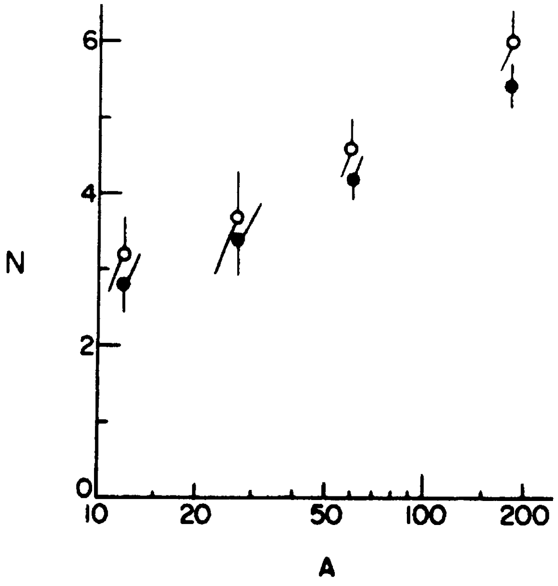

Figure 1-11: The average numbers of nucleons participating in the absorption process. From McKeown *et al.*[75].

rays following the reaction. The Navon *et al.* and Ashery *et al.* experiments were transmission/scattering measurements where the total pion reaction cross section was determined *via* a transmission experiment and the scattering measurement determined the amount of reaction cross section that came from the scattering of the pion. The charge exchange part also had to be estimated and subtracted to get a measure of the absorption cross section. These works helped to establish the power law dependence of the total absorption cross section with increasing mass number as well as other features of the absorption cross section, such as the pion's absorption cross section's strong resonance behavior[78] (see Figures 1-13 and 1-14).

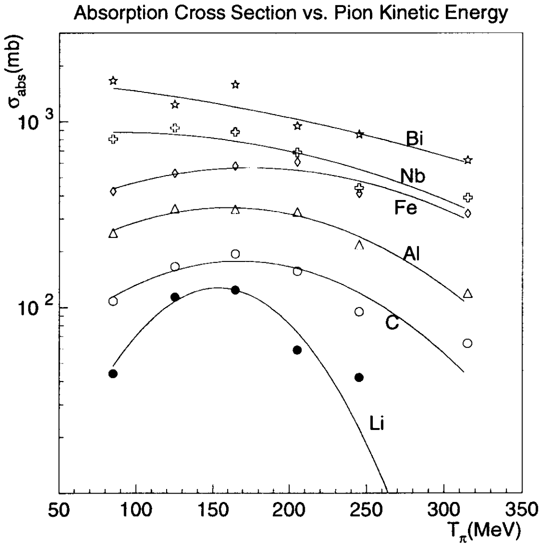

Figure 1-12: Plot of the pion absorption cross section *vs.* incident pion kinetic energy for various target nuclei. The data are from Ashery *et al.*[78]. The lines are to guide the eye.

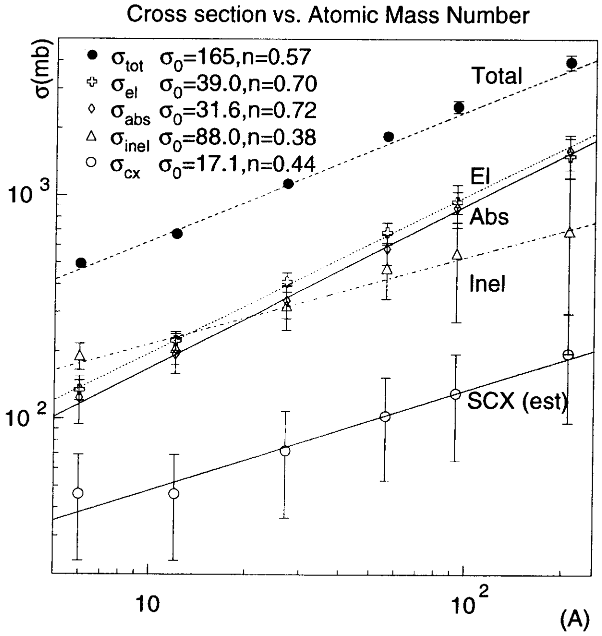

Figure 1-13: Plot of the pion cross sections *vs.* target atomic mass number for $T_\pi = 165$ MeV showing the amounts of each process seen to contribute to the total pion reaction cross section. The data are from Ashery *et al.*[78]. The lines are fits to $\sigma = \sigma_0 \times A^n$.

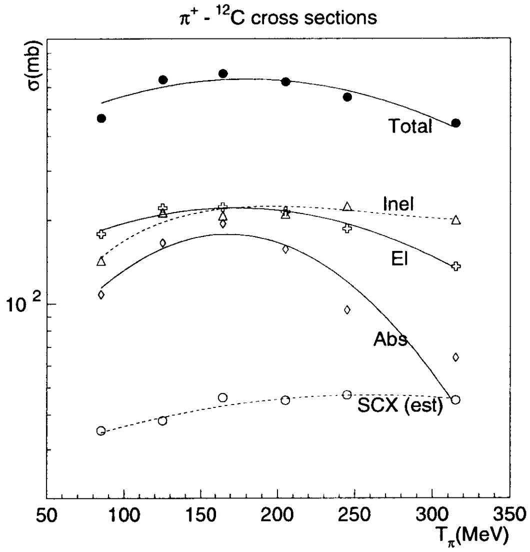

Figure 1-14: Plot of the pion cross sections *vs.* incident pion kinetic energy for pion reactions on carbon showing the amounts of each process seen to contribute to the total pion reaction cross section. The data are from Ashery *et al.*[78]. The lines are to guide the eye.

While measurements of the total absorption cross section were important and presented useful information, the multiplicity results of McKeown *et al.*[75] really drove the field of pion absorption. Experiments were run to try to determine more precisely what was involved in the process of pion absorption. Was two-nucleon absorption really the end of the story and could everything be explained by initial- and final-state interactions or was there new and different physics yet to be discovered?

One of the first results from this new group of experiments was that of Gotta *et al.*[79]. In this experiment of stopped pion absorption on ^{3}He, Gotta *et al.* performed a kinematically complete measurement which enabled the group to perform an analysis in unprecedented detail on a light nucleus. Gotta *et al.*'s analysis made extensive use of a Dalitz plot wherein the kinetic energy of one particle is plotted against the kinetic energy of another particle. This method of analysis results in the final kinematics of a 3-body final state being fully defined at any point in the allowed area of a Dalitz plot (see Figure 1-15). In a Dalitz plot, events with a relative angle of 180° between any two particles fall on the perimeter of the kinematically allowed region. Events in which the energy is shared more or less equally among all three particles would fall in the central region of the Dalitz plot. Gotta *et al.* found no evidence of 3NA in absorption of stopped pions, indicated by the dearth of events in the central region of the Dalitz plot, but evidence of FSI was seen.

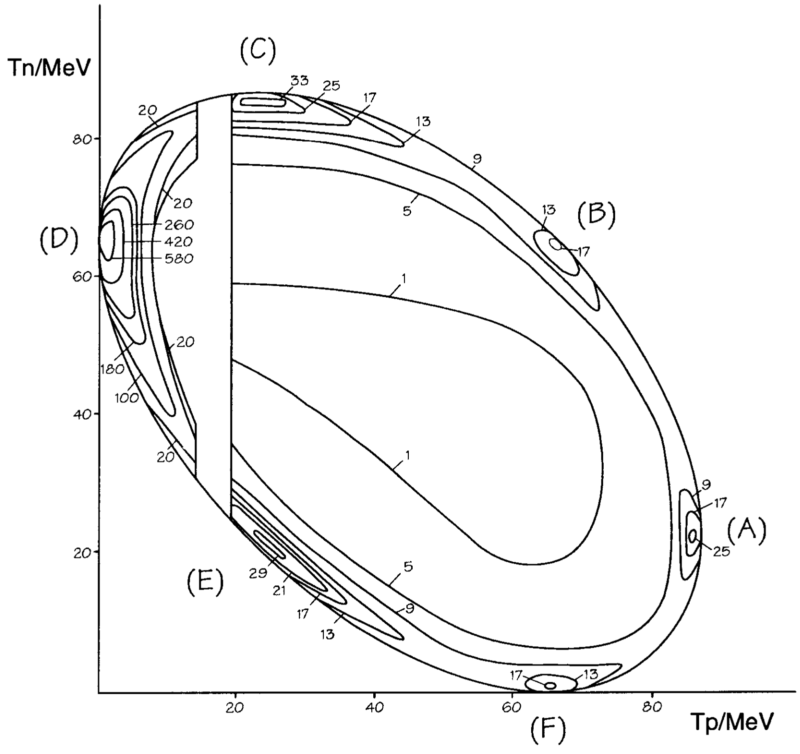

Figure 1-15: Dalitz plot from Gotta *et al.*[79]. The regions marked D, B, and F correspond to QFA on a *pp*-pair, a *pn*-pair and a *pn*-pair respectively. The regions marked A, C, and E correspond to classical *nn*-FSI, *np*-FSI, and *np*-FSI respectively following QFA.

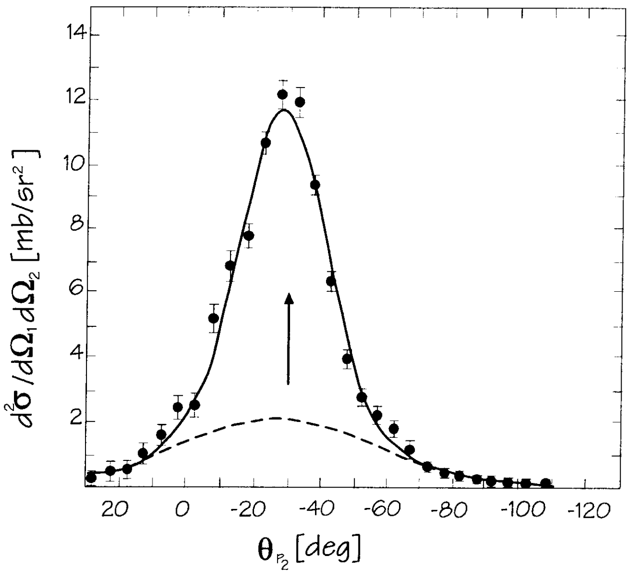

Figure 1-16: The angular correlation for the reaction $^{12}C(\pi^+, 2p)$. The arrow marks the angle for the reaction $\pi^+ d \rightarrow pp$ and the curves are gaussian fits to the data. From Altman *et al.*[80].

The early eighties also saw other investigations of pion absorption. In 1983, Altman *et al.* published the results of a two-arm experiment studying pion absorption on carbon[80]. Using an analysis method which was soon to cause some controversy, Altman *et al.* analyzed the $p-p$ angular correlation to identify undisturbed QFA. The analysis was done by fitting the $p-p$ angular correlation with two gaussians: one narrow, one broad. See Figure 1-16. The narrow gaussian was associated with undisturbed QFA, and the broad gaussian with other more complicated processes such as FSI and multi-nucleon absorption (MNA). After correcting for losses in the narrow gaussian from FSI, Altman *et al.* found that QFA accounted for less than 25% of the total absorption cross section.

The next year the same collaboration published results of pion absorption on ^{16,18}O[81] and using the same two-gaussian analysis technique found that cross shell 2NA is suppressed. About this time, Ritchie *et al.*[82] published a reanalysis of the earlier Altman data[80]. In their reanalysis, they determined that the two-gaussian analysis severely underestimated the amount of QFA and that, in fact, a broad gaussian could be produced by absorption on $L = 2$ clusters. The reanalysis also showed that no other "background" processes were necessary to explain the experimental data. But the reanalysis left some issues unresolved; when doing the full DWIA analysis on absorption on carbon, Ritchie *et al.* found that they could reproduce only Altman's narrow gaussian and that the broad gaussian from $l = 2$ clusters was actually included in Altman's narrow gaussian.

The two gaussian analysis was used again in a later paper by Altman *et al.*[83] in their more complete survey of pion absorption on several heavier nuclei and it was found that undisturbed QFA accounted for only 10% of the pion absorption cross section on carbon and decreased to 2% for absorption on bismuth. Other groups did similar analyses on other nuclei [84, 85, 86] and found results of about 50% of the total pion absorption coming from from 2NA (*e.g.* QFA possibly followed by FSI) in contradiction to the Altman *et al.* results. In addition, the earlier Burger *et al.*[84] results indicated that fewer than 30% of the pions scattered before being absorbed. Finally, these later papers (*e.g.* Burger *et al.*), through careful analysis, demonstrated the validity of using the two gaussian approach to isolate undisturbed QFA by showing that the yield in the narrow gaussian was independent of the cut in excitation energy used.

Over this same period of time other investigations were underway to try to measure what the other reactions involved in pion absorption could be. In 1985, Backenstoss *et al.* published the results of a kinematically complete experiment of pion absorption on ^{3}He[87]. By comparing the angular distribution of the p from $\pi^{+3}He \rightarrow ppp$ with the results of three-body phase space (see Figure 1-17) they deduced the existence of a genuine 3NA mechanism. They also determined that, while a 3NA process existed, it accounted for $\sim$ 25% of the total absorption cross section on ^{3}He at this energy. The authors also suggested that their results along with the results of stopped pions by Gotta *et al.*[79], which show $<$ 10% contribution of 3NA, point to a stronger energy dependence to the three-nucleon mechanism than QFA and may suggest a multi-Δ mechanism.

Also in 1985, Tacik *et al.*[88] published their results of a triple coincidence experiment measuring positive pion absorption on carbon for 228 MeV pions. The goal of the Tacik *et al.* measurement was to observe ISI followed by QFA of the recoil pion. Tacik *et al.* found no evidence that a two-step process ISI-QFA existed and in fact found that their data were best represented by $pppn\alpha\alpha$ phase space. A reanalysis of these data by this group in 1989[89], including two other energies led to the conclusion that processes more complicated than 3NA need not be considered. Later works by Yokota *et al.*[90] and

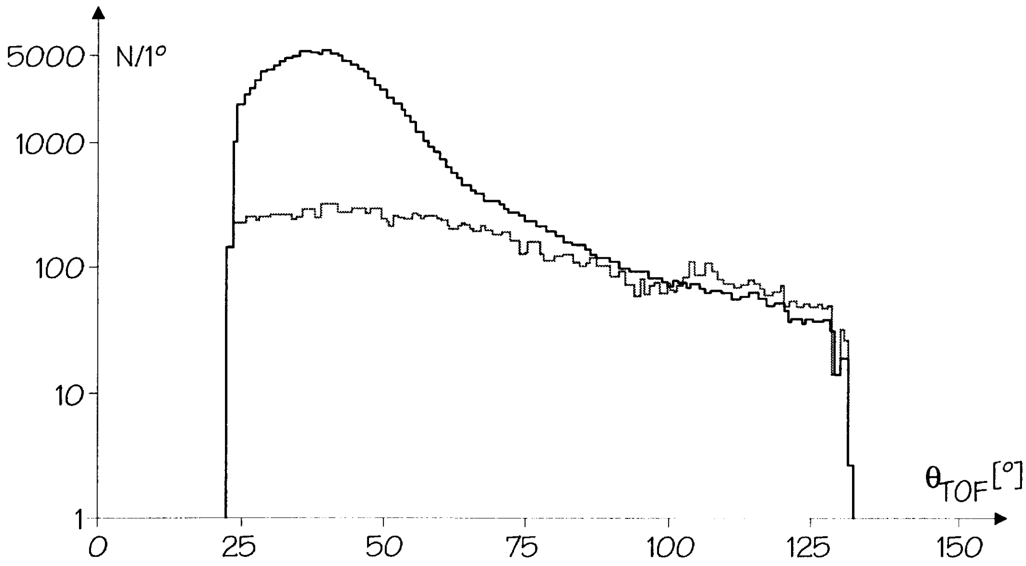

Figure 1-17: The angular distribution of the p from $\pi^{+3}He \rightarrow ppp$. The lower curve is 3N phase space, the solid is data. From Backenstoss *et al.*[87].

Backenstoss *et al.*[91, 92] found evidence of 3NA[90, 91, 92] as well as possibly a 4NA mode[92].

Results were also being published by Smith *et al.* and Mukhopadhyay *et al.*[93, 94] from experiments that were trying to determine the energy dependence of the 2NA:3NA ratio. These collaborations found that both the 2NA and the 3NA cross section had similar energy dependence. Others such as Hyman *et al.*[86] and Mack *et al.*[95] were trying to nail down how much of the total absorption cross section come from 2NA *vs.* all other channels. The values range from 50% [86] to 75% [95] of the total measured cross section coming from a 2NA process when corrected for expected final-state-interactions.

In addition, the search for more exotic absorption measurements continued with Rzehorz *et al.* [96] claiming to see direct evidence of a 4NA process.

Over this same period, it was realized that if as much of the total absorption cross section (25-75%) came from 2NA modified by FSI and ISI as previous results had indicated, there should be some obvious and clear kinematic signatures of such processes happening. In 1987, Brückner published the results of a study of $^{12}C(\pi^+, ppp)X$ using a magnetic proton spectrometer as well as large solid angle plastic scintillator array. The goal of the experiment was to measure possible modifications of the Δ wave function in nuclear matter leading to extended lifetimes. Brückner saw no evidence of this, but in the process saw a broad structure in the coincidence proton's energy spectra associated with the initial scattering off one of the protons by the incident pion (see Figure 1-18).

Also in 1987, Yokota *et al.* published a paper claiming to see direct evidence of ISI and FSI in the (π^-, pp) cross sections on ^{6}Li and ^{12}C at 165 MeV incident pion kinetic energy. What was seen were two peaks in the *pp* angular correlation spectrum, one at 100° which was associated with FSI and another at 170° which the group associated with single charge exchange ISI followed by neutral pion absorption on a *pp* pair. Neither the Brückner *et al.* nor the Yokota *et al.* work attempted to estimate how much ISI or FSI contributed to the total absorption cross section seen, but only reported that such direct evidence was seen.

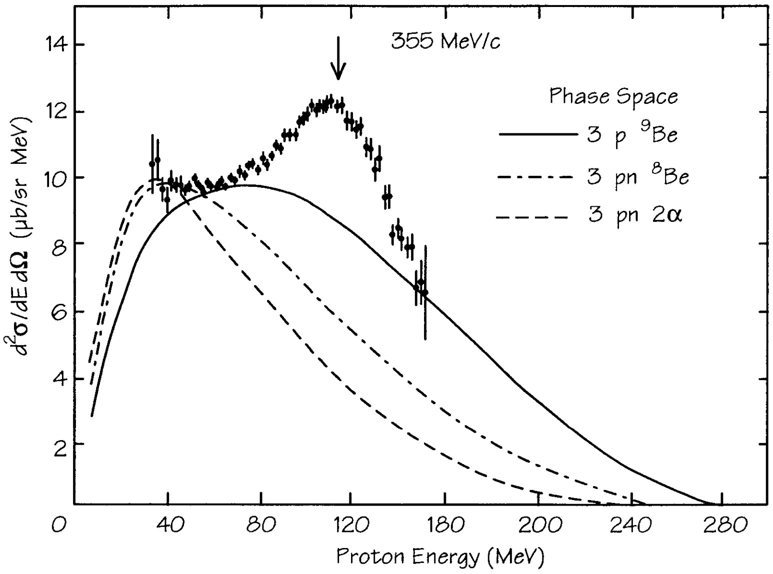

Figure 1-18: Energy spectrum of protons emitted at 8° for an incident π^+ momentum of 355 MeV/c. The curves are phase space calculations. From Ref. [97].

The desire for a better understanding of pion absorption led to large solid angle experiments, which were first done with vertical cylinders of plastic scintillator as in Adimi *et al.*[98] and Bauer *et al.*[99] and were later done with dedicated nearly 4π detector systems *i.e.* BGO-Ball, based at LAMPF, and LADS, based at PSI.

Because of the nature of the experiments (both were vertical plastic $\Delta E - E$ telescope cylinders), the earlier large solid angle measurements suffered from poor angular granularity, which made it difficult to separate genuine multi-nucleon absorption events from multi-step processes leading to more than two energetic particles in the final state. Adimi *et al.* determined that 50% of the total pion absorption cross section on ^{4}He at

T_π = 1124 and 162 MeV could be attributed to 2NA, if corrections were made for FSI. They also determined that 30% of the outgoing protons underwent FSI.

Bauer *et al.*, on the other hand, could not separate genuine 3NA and 4NA processes from events in which ISI or FSI played a part. Because of this, their results were expressed in the number of energetic particles in the final state. They reported an average number of nucleons involved to be $2.5^{+1.0}_{-0.5}$ and that one third of the cross section came from the emission of 3 or 4 nucleons.

To answer the questions of multi-nucleon absorption modes, the nearly 4π detectors BGO-ball and LADS were built. The BGO-ball papers of Ransome *et al.*[100, 101, 102, 103] and Jones *et al.*[104] presented the results of a large-solid angle study of pion absorption on ^{6}Li[100, 101] and for numerous heavy targets[102, 103, 104] for energies around[100, 101, 102, 103] and above[104] the Δ resonance. The analysis of the ^{6}Li data concluded that from 25% to 50% of the total absorption cross section, depending on the incident pion energy, came from 3NA processes with 1 proton unobserved and having absorption on a pnn triplet dominating. Also, because the detected $3p$ cross section was so small, the BGO-Ball collaboration concluded that ISI did not contribute significantly to the absorption mechanism.

The later BGO-Ball results[102, 103, 104] are a little more difficult to interpret. The BGO-Ball detector suffered from poor angular granularity, which meant that momenta could not be determined very precisely. Also, because of the detector's small size, neutrons could not be separated from γs. Both of these factors meant that extensive modeling of the detector with Monte Carlo simulations was required to extract physics quantities from the data. This apparently was not done and the particle multiplicities that were presented were for observed multiplicities only.

The other nearly 4π solid angle detector system used to study pion absorption was the LADS detector based at PSI in Villigen, Switzerland. LADS was built to investigate multi-nucleon absorption nodes on various nuclei. Recently, several results of the LADS collaboration have been published.

The first of these results was the work of Alteholz *et al.*[105], which investigated pion absorption on ^{3}He at 118, 165 and 239 MeV. This work separated the cross section into a part which appeared to have come from 2NA (quasi deuteron absorption) and 3NA (pion absorption in which the three nucleons were involved). It was found that 70% of the total absorption cross section at these energies could be attributed to 2NA.

Further work on ^{3}He by the LADS collaboration refined the measurement of the 3NA process on ^{3}He seeing strong kinematic evidence of ISI[106] and determining that approximately two thirds of the 3NA events came from a phase-space like process while the remaining third was mostly ISI[107].

Later LADS results established that the kinematic signature for ISI was seen in other targets measured by LADS (^{3}He, ^{4}He, N, Ar, Xe)[108, 109] as well as establishing that the 3p cross section was no more than 10% of the total cross sections in N, Ar, Xe and that ISI was a substantial fraction of the 3p cross section only at 239 MeV (30-40%). Otherwise, it was on the order of 10% of the 3p cross section[109].

More detailed studies of pion absorption on ^{3}He and ^{4}He were also done by the LADS collaboration. Lehmann *et al.*[110] studied the *ppp* final state in ^{3}He and ^{4}He and determined that about 1/2 of the *ppp* yield could not be explained by ISI or FSI and slightly later, Lehmann *et al.*[111] looking at *pppn* final states in ^{4}He found that ISI and FSI accounted for no more than 1/3 of the *pppn* yield as well as finding that 4NA yield accounted for 1-8% of the total absorption cross section. In Mateos *et al.*[112] the total and partial absorption cross sections on ^{4}He were determined and presented. While 2NA was the dominant fraction at all pion energies, it was $\leq$60% of the total absorption cross section.

Finally, very recently, Tacik *et al.*[113] published the results from an experiment measuring ^{12}C(π^+,*pp*) and ^{12}C(π^+,*ppp*) at energies above the Δ resonance using the CHAOS spectrometer at TRIUMF. This was what can be classified as a medium solid angle measurement although the measurement was still an in-plane measurement. In the analysis of their data, Tacik *et al.* again changed what they report as the processes contributing to pion absorption. In their analysis, they concluded that they saw no evidence of 3NA and that all of their *ppp* data could be explained by ISI-2NA and 4NA. Their measurement, though, only accounted for about 50% of the total absorption cross section with the rest left unexplained. From the results of the LADS papers [105] it was seen that, out-of-plane events do not behave simply like phase space and in fact are an important part of the measurement.

1.4.6 This Work

From the proceeding discussion, it is seen that there are at least two currently open questions regarding pion absorption. One, what is the behavior of the pion total absorption cross section as a function of the target nucleus mass? Two, what are the processes that contribute to the pion absorption cross section and in what ratios? Also seen is that the large-solid-angle detectors are necessary tools to resolve these questions. This work will attempt to address question one by performing a total absorption measurement, and question two by determining which channels contribute to the pion total absorption cross section. The large-solid-angle measurement will allow for a determination of the total absorption cross section with only small extrapolations over unmeasured regions of phase space. By measuring Xe and comparing to lighter nuclei, the A-dependence of the total absorption cross section will be firmly established, and by performing a breakup of the experimental data into physics channels, valuable information on the processes contributing to the observed cross sections will be obtained.

Chapter 2

Experimental Apparatus and Procedures

The main goal of the LADS experiment was the measurement and quantification of multi-nucleon pion absorption modes in nuclei for pion energies near the $\Delta(1232)$ resonance. To this end, a detector system was built and several experimental runs were performed at the Paul Scherrer Institute (PSI) in Villigen Switzerland. To study multi-nucleon final states the detector must cover a large fraction of phase space; *i.e.* the detector must cover very nearly 4π steradians of geometrical acceptance and have a low energy threshold for particle detection. The detector must also have enough granularity to detect and classify several reaction products simultaneously. Finally, the detector must be able to differentiate between different particle types, whether neutral or charged, on an event by event basis. This chapter will describe the pion facility, the experimental apparatus, LADS, and the associated data acquisition (DAQ) electronics used to gather the data.

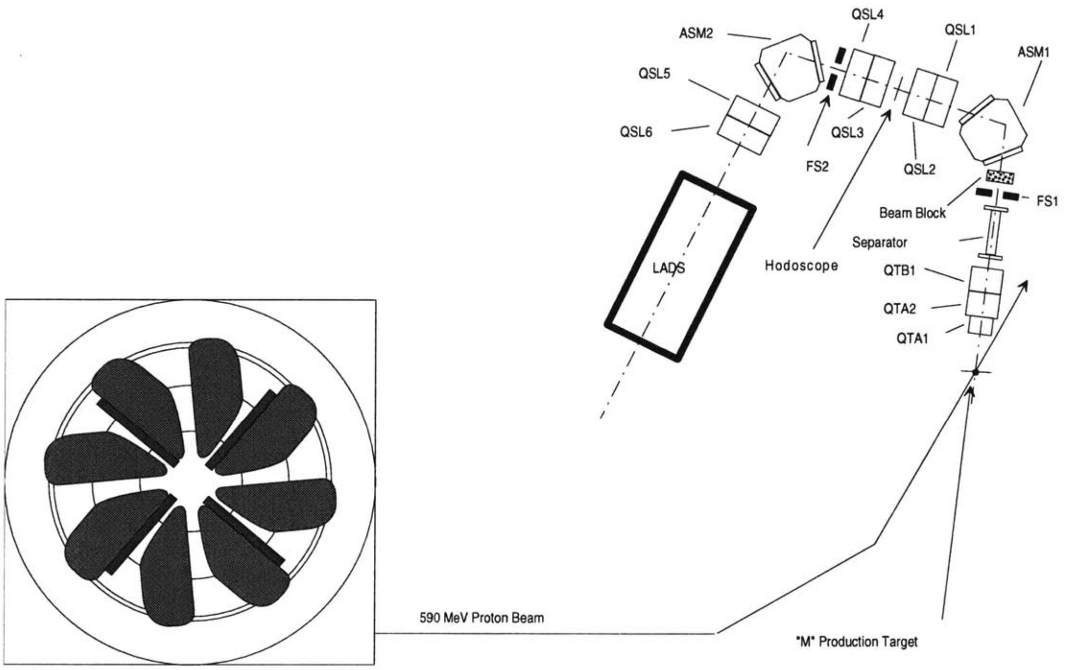

Figure 2-1: A schematic of the PSI Ring Cyclotron showing the πM1 area.

Later chapters will elucidate the procedures used in the data analysis and the assignment of uncertainties to the determined cross sections.

2.1 The Beam Line at PSI

As was stated above, the detector was built and the experiment performed at PSI. Specifically, the experiment was performed as the πM1 channel of the facility. The PSI accelerator was a 590 MeV cyclotron which produced a 1000 - 1500 μA proton beam at the time the experiment was conducted. A portion of the proton beam was directed onto a carbon or beryllium target which, because of the intensity of the proton beam, was spun to prevent it from being locally overheated. Through nuclear reactions, the protons produced pions with a broad energy spectrum. The flux of protons on the target was monitored at the pion production target and the pions streamed into several beam lines where they were momentum selected and focused onto targets in the experimental areas. More information about the PSI cyclotron and pion targets is available in the PSI users guide [114].

During experimental runs, LADS was situated at the end of the πM1 beam line. The πM1 beam line was a high resolution pion channel designed to provide pions with good momentum resolution. The πM1 beam line was optically symmetric about the intermediate focus, where the horizontal magnification of the production target was approximately unity and the beam had a momentum dispersion of $d_x = 7cm/\%$. The dispersion of the beam at the intermediate focus allowed the momentum of the pion to be determined using a hodoscope. The hodoscope used was a detector consisting of uniform vertical plastic scintillator strips, which measured the horizontal position information of the pion beam at the intermediate focus. Knowledge of the x-position of the pion allowed an accurate determination of its momentum; for the πM1 channel, the momentum could be determined to $dp/p = 3 \times 10^{-4}$ (FWHM). The positional information measured by the hodoscope was encoded into a bit pattern and was routed to the LADS electronics shack for use in the trigger and data acquisition.

The optics of the beam line consisted of nine SIN standard quadrupoles and two identical bending magnets designed specifically for the πM1 channel. A 2m electrostatic separator (crossed electric and magnetic fields) built at CERN removed protons from the pion channel and allowed the proton contamination to be reduced from 4:1 to approximately 1:20. The optics of the beam line also allowed the pions to be focused in a region in the center of the LADS detector with a beam spot approximately 1 cm in diameter. More information about the πM1 high resolution pion channel is available in two NIM articles[115, 116].

2.2 The Gas Target

The cross sections LADS was designed to measure are relatively large, but, to reduce background from target's walls and to aid in obtaining high statistics, a thick target was desired. The small amount of space inside LADS did not allow for the bulky plumbing and hardware associated with a cryogenic target. Thus, a high pressure gas target was used to fulfill the desire for a thick target. LADS used a 25.7 cm X 4 cm cigar shaped carbon fiber cylinder, manufactured by Dornier Ltd., to hold a number of target gases.

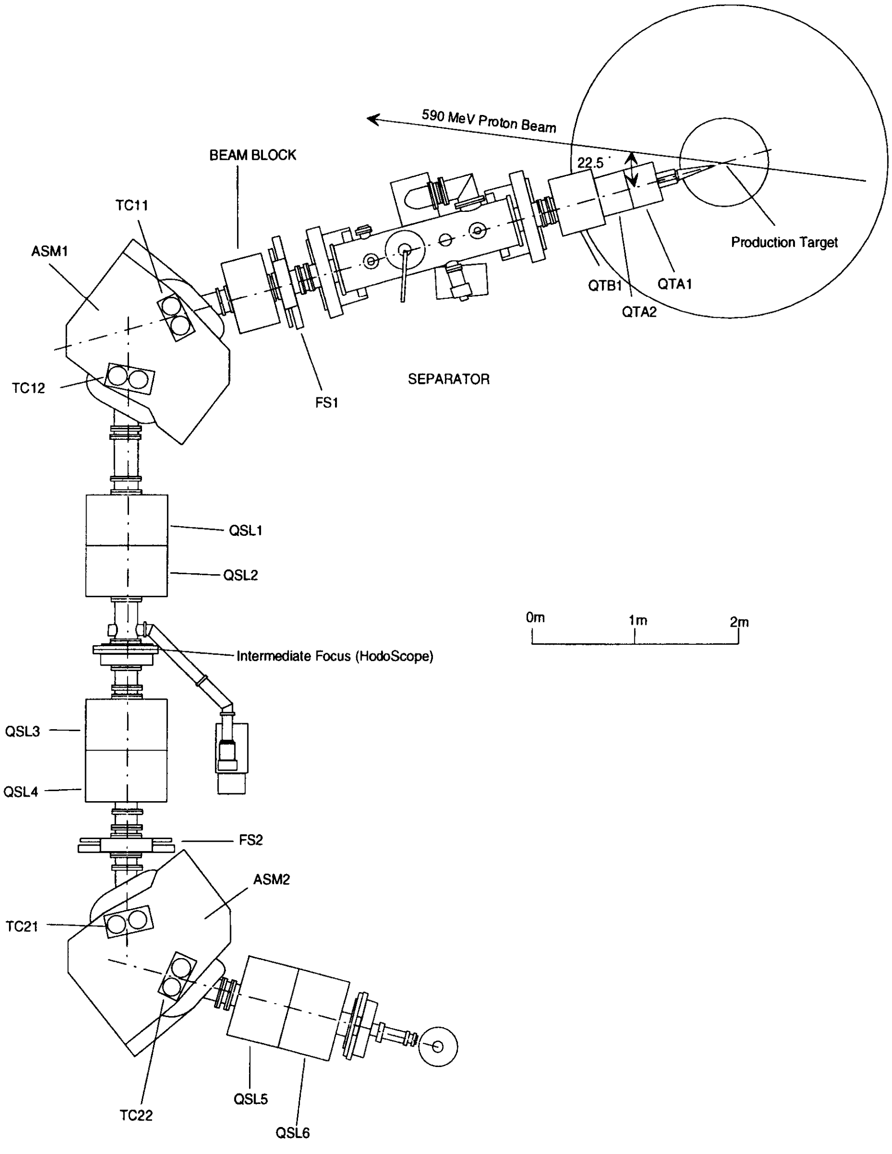

Figure 2-2: A schematic of the πM1 beam line. [114].

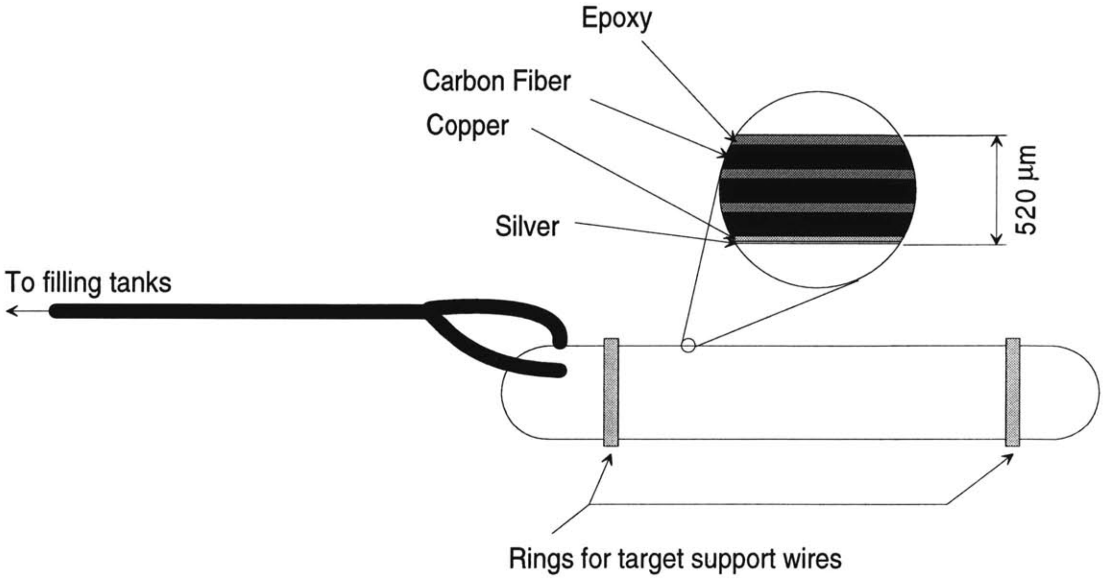

Figure 2-3: A schematic of the LADS target cell.

The cylindrical target geometry complemented the geometry of LADS and enhanced the target thickness. The innermost layer of the target was a 30 μm Cu-Ag lining (10 μm of Ag followed by 20 μm of Cu), which had been galvanically applied to the target walls. The target walls themselves were composed of a carbon fiber and epoxy sandwich which consisted of three layers of carbon fiber glued together with epoxy. The winding of the carbon fiber alternated: one layer was wound in the longitudinal direction and the next layer was wound in the azimuthal direction for a total wall thickness, including the metal layers, of 520 μm (see Figure 2-3). The carbon fiber target had great strength and was capable of withstanding pressures in excess of 120 bar. During data runs, the pressure inside the Xe filled target was about 15 bar.

The target was filled through two 3mm (i.d.) stainless steel pipes attached to both sides of one end of the target and connected to another longer pipe which extended outside the LADS detector volume. The longer pipe was attached to a rail for mounting the target inside LADS. To enable subtraction of the background from the target's walls in the data analysis, it was desired to keep the full and empty target in the same z-position along the beam axis. Therefore, the gas target was emptied and filled while inside LADS. In addition, the target cell had to be aligned accurately for maximum reduction of the carbon background from the target's walls. A theodolite, a device for accurately measuring angles, could be mounted on LADS, usually during target filling, and used for positioning the target so that the beam hit the center. The theodolite was also used to estimate the alignment of the target cell axis relative to the beam axis. If the cell was found to be misaligned or off center from the beam axis, then target support wires were tensioned, relaxed, or displaced to position the target correctly. A simple length measurement determined the position of the target along the the beam axis within LADS.

2.3 The Large Acceptance Detector System

LADS was built to cover very nearly 4π steradians of angular acceptance. The detector consisted of a 28 sector barrel with 14 sector endcaps closing each end (see Figure 2-

4). The first detector elements that a reaction product encountered were two cylindrical wire chambers. The smaller unit consisted of a concentric double chamber (inner and middle) with anode radii of $\sim$60 mm and an active length of $\sim$900 mm; the larger (outer) chamber had an anode radius of $\sim$280 mm and an active length of $\sim$1600 mm. The reaction products then passed through the scintillator portion of LADS. The scintillators were set up to work as $\Delta E - E - E$ telescopes: the reaction products passed through the ΔE portion of a sector of LADS and then encountered the two E-blocks. The cylindrical geometry of the MWPC and capped cylinder geometry of the scintillator package allowed LADS to cover nearly 4π of solid angle. The thickness of the target was a major factor in the energy threshold for charged particle detection; nevertheless, LADS was able to detect protons with a kinetic energy as low as 20 MeV. The main parameters of the LADS detector are given in Table 2.1.

2.3.1 Multi-Wire Proportional Chambers

The purpose of LADS's Multi-Wire Proportional Chambers (MWPCs) was to determine accurately the z and ϕ position of a charged particle when it hit the active area of the chamber. In addition, the MWPCs had to withstand a high beam rate ($\sim$1x10^6 events/s) and, to minimize multiple scattering of the reactions products and preserve the low detection threshold for protons, the MWPCs had to be of low mass. The parameters

LADS's Performance	
Geometrical acceptance	98.5% of 4π sr
Energy threshold for protons	$\approx$ 20 MeV
Maximum measurable proton energy	$>$ 200 MeV
Energy resolution for charged particles	3-5% (FWHM)
Missing Momentum resolution	$<$ 50 MeV/c for 3p events
Vertex resolution from two tracks	1 mm (FWHM)
Angular resolution	$< 1°$
Detection efficiency for neutrons	$\approx$ 35%
Angular resolution for neutrons	$\approx 10°$

Table 2.1: LADS's performance characteristics.

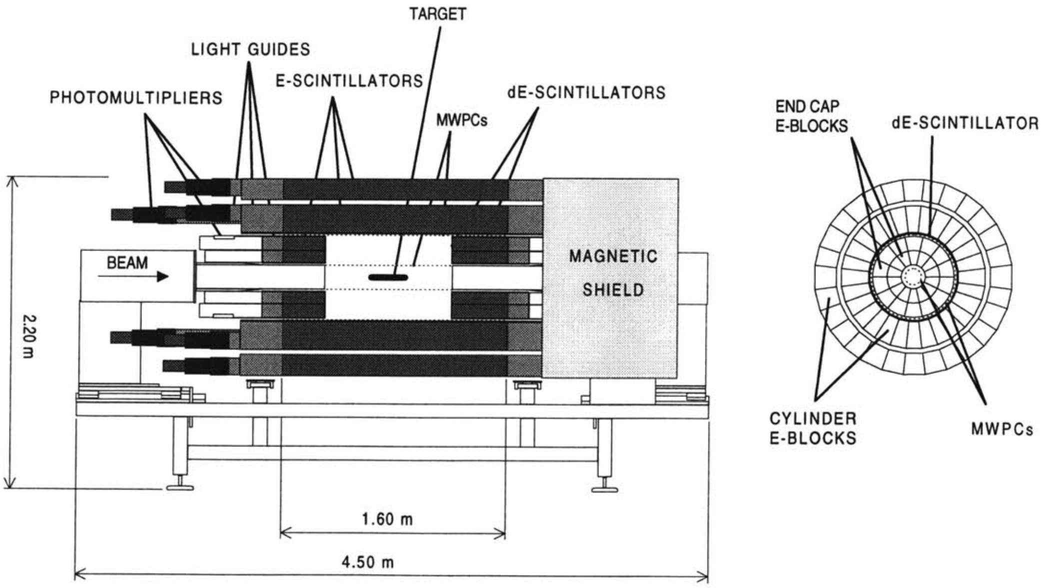

Figure 2-4: The LADS detector.

of the MWPCs used for taking the 1993 data are summarized in Table 2.2. Consistent with the geometry of the LADS detector, the MWPCs were cylindrical. LADS used two MWPCs of essentially the same design: the inner/middle chamber unit with an active anode radius of about 64 mm and the outer chamber with an active anode radius of about 280 mm. The chambers had an active length of 900 mm and 1600 mm for the inner and outer chambers, respectively.

The anode planes of both wire chambers consisted of gold plated 20 micron tungsten-rhenium wires tensioned to 0.6 N which spanned the chambers respective lengths. The distance between wires on each chamber was approximately 2 mm and each wire was positioned to 50 micron accuracy.

Determining the z and ϕ position of a particle detected by the MWPCs required not only that both the anode wires and cathode plane information was read out, but also that the cathode planes were separated into strips to determine the z position. The resolution of the z position of a hit in a chamber had a $1/\sin(\theta)$ dependence where θ was the angle of the cathode strips with respect to the beam axis. The outer chamber had a total of 560 cathode channels with a strip width of approximately 4.4 mm on both the inner and outer cathode planes of the chamber. The cathode strips were wound helically around the chamber at an angle of 45.86° for the inner cathode plane and 44.21° for the outer cathode plane. The pitch of the inner and outer cathode planes was such that cathode strips usually crossed twice. The ambiguity in the crossing was solved by combining the cathode information with the anode wire information.

Because of its small radius, the inner and middle chambers would need an extremely shallow strip pitch to have at most two cathode crossings. The shallow pitch was undesirable because z position resolution would have suffered. The solution was to reduce the effective length of the inner and middle MWPCs by etching a gap in the cathode strips perpendicular to the beam axis at the middle of the chambers. The inner and middle MWPCs were then functionally cut into two chambers, an upstream chamber and a downstream chamber. The inner MWPC had 384 cathode channels and a 3.810/3.83 mm cathode strip width on the inner/outer cathode planes. The cathode strips were helically wound with an angle of 15.09°/24.56° for the inner/outer cathode planes. The middle chamber also had 384 cathode channels, but with a 3.98/3.81 mm cathode strip width on the inner/outer cathode planes and a wind angle of 24.15°/19.86° for the inner/outer planes.

The cathode planes of the MWPCs were made from aluminized mylar which was etched with 0.6 mm wide lines to form the cathode strips. For the outer chamber, which was built for the 1991 run, the mylar was etched with a dental drill attached to a plotter. For the double inner (inner/middle) chamber the foils were etched with a fine thread soaked in a strong base. The cathode planes were glued with Araldit to Rohacell[117]

MWPC Specifications	Middle/Inner Chamber	Outer Chamber
Anode Diameter(mm)	128/112	560
Number of wires	176/144	832
Wire spacing (mm)	2.285/2.444	2.115
Number of cathode strips	384/384	560
Cathode strip width (mm) (outer,inner planes) (Including .6 mm gap)	3.81,3.98/3.83,3.10	4.40,4.40
Strip angles outer,inner planes (deg)	19.86,24.15/24.56,15.09	45.86,44.21
Anode-cathode gap (mm)	3/3	4
Anode HV (+V)	2300/2200	2800
Chamber Thickness (mg/cm^2)	74.2	57.2

Table 2.2: MWPC parameters

and then formed into cylinders. The Rohacell provided strength and support for the cathode planes and gave the chambers rigidity. Finally, the external surfaces were covered with aluminized Kapton to serve as grounding planes. The chamber ends were capped with Stesalit[118] rings between which the anode wires were strung. Because of the length of the outer chamber, the anode wires were supported by a Rohacell support ring at the chamber center to increase wire stability. During their operation, the chambers were flushed continuously at a rate of 20-30 ml/min with a premixed room-temperature mixture of 46.8% C_2H_6, 0.2 % Freon, and 50% Ar.

2.3.2 Scintillator Package

The specifications for the LADS detector included the ability to separate charged particles of different masses and a reasonable neutron detection efficiency and angular resolution. LADS also had to stop protons with an energy of 200 MeV normal to the beam axis and have adequate energy resolution for charged particles. To accomplish this, the cylinder of LADS was constructed of 28 sectors of Bicron NE-102[119] plastic scintillator $\Delta E - E - E$ telescopes bound like a barrel. The endcaps were constructed of 14 sectors of telescope with the ΔE sectors offset from the E-blocks to improve angular granularity in the endcaps. The ΔE scintillators were used for determining if a particle detected by a sector was charged or neutral. The combination of the ΔE and E-blocks was used for particle identification and the sectors were of sufficient thickness to stop 200 MeV protons and to provide a neutron detection efficiency of about 40%

2.3.2.1 Cylinder Scintillators

As stated above, the cylinder was constructed of a ΔE strip and two E-block bars arranged as a scintillator telescope with an active region 1600 mm long. The active region of the E-block scintillators were coupled to Hamamatsu R1250 5" photo multiplier tubes (PMTs) *via* a length of Lucite light guide. The PMT was optically coupled to the light guide using an optical epoxy sealant[120]. The PMT was mechanically supported by four threaded rods screwed into a plate against which the base of the PMT rested. The active regions of the ΔE scintillators were coupled to Hamamatsu R1355 PMTs via ultraviolet transmitting (UVT) light guide. The PMTs were bought as a hybrid detector with a custom made resistive base. The light from the scintillators of the cylinder was collected from both ends for several reasons. Among them, the amount of light collected was made largely independent of the position of the detected particle in the scintillator and using TDC information the position of the particle in the scintillator could be determined without using MWPC information. Also, reading out both ends increased the amount of photons collected by about a factor of two and therefore the uncertainty of the TDC measurement was decreased by about a factor of $\sqrt{2}$.

2.3.2.2 Endcap Scintillators

The endcap scintillators of LADS consisted of inner E-blocks, outer E-blocks, ΔE strips and veto counters. The arrangement of the endcap counters was slightly different from that of the cylinder. The endcap consisted of veto counters wrapped around a steel support cylinder. The inner E-blocks were wrapped around the vetos, while the outer E-Blocks were wrapped around the inner E-blocks. The ΔE counters were placed on the inside end of the inner/outer E-block unit. The ΔE's light guides were the last layer, just outside of the outer blocks, and the entire unit was bound together (see Figure

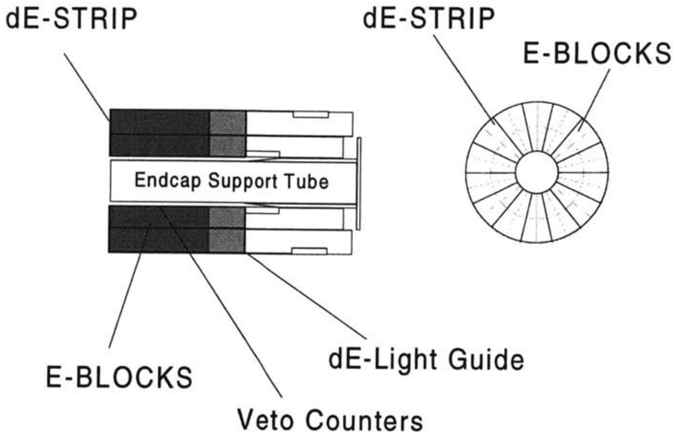

Figure 2-5: A schematic of the LADS endcap showing the position of the ΔE and E blocks.

2-5). The PMTs for the outer *E*-blocks were 3" Phillips XP2313Bs, while 2" Phillips XP2262B PMTs were used for the inner *E*-blocks. Both the inner and outer PMTs used bases manufactured by the Zagreb members of the LADS collaboration. The endcap ΔE PMTs and bases were identical to those used for the cylinder ΔEs.

The veto counters were designed to eliminate events which had signals in the endcaps, but did not have trajectories that traced back through the ΔEs. The 1 mm scintillator strips were coupled to 1/2" Phillips XP1911 PMTs *via* Lucite light guides.

The gains of all of the plastic scintillators/PMTs were monitored using temperature stabilized LEDs which were calibrated to give a constant amount of light. The LEDs were powered by an LED pulser developed at PSI which was capable of pulsing the LEDs at rates up to 10 kHz. The LEDs were run continuously throughout the experiment to monitor the stability of the PMTs and to reduce the gain shift caused by varying signal rates in the PMTs

LADS was not a permanent fixture in the πM1 experimental area; after an experimental run, the detector was moved to a parking area elsewhere in the experimental hall. Moving LADS to a parking area required disconnecting the signal lines and high voltage (HV) lines from the detector elements. Because of the difficulty of wiring the PMTs and the fragility of the mounts of the PMTs, all of the PMT signal and HV connections were achieved through the use of patch panels mounted in the ends of the LADS cylinder.

2.4 Electronics

After the products of a reaction created signals in the MWPCs and/or the scintillators, the signals were processed into a form that could be read by the data acquisition (DAQ) system. The processing required several steps; the signals in the MWPCs had to be converted into hit patterns, and the light collected by the PMTs had to be processed so that the DAQ could determine if a signal in a telescope/segment was caused by a charged or neutral particle, and then collect the total amount of light deposited in the scintillator telescope. It was the signal processing electronics which converted the signals from LADS into a form useable by the DAQ system.

2.4.1 MWPC electronics

The anode wires for the cylindrical MWPCs were read out and encoded using the LeCroy PCOSIII system. Because of space constraints, the charge discriminator cards were not mounted in the chambers, but mounted instead in specially constructed crates. The anode signals were routed to the discriminator cards using a flat shielded cable. The logic signals from the discriminators were routed to the PCOS III delay and latch modules in a PCOS III controller crate. PCOS III encoded the data into hit patterns, which included cluster position and cluster width, and sent the encoded data to a CAMAC crate in the electronics shack where it was collected by the DAQ system.

The cathode signals were routed by the same style of flat shielded cable that was used for the anode signals to LeCroy TRA 1000 current sensitive preamplifiers. The outputs of the preamplifiers were connected to PSI designed postamplifiers in the electronics shack using about 50m of twisted pair cable. The amplified signal was routed and AC coupled to LeCroy 1885 96-channel Fastbus ADC's which had a resolution of 12 bits, a range of 1350 pC, and a conversion time of 275 μs. The cathodes' ADCs were controlled by a

LeCroy SM/I 1821 Segment Manager Interface system processor which sent the data to the DAQ system.

2.4.2 Scintillator Electronics

The signals from the PMT patch panels on the ends of the LADS detector were routed to the electronics shack via 50Ω shielded cables. All of the plastic scintillator signals from the PMTs were connected to a patch panel in the back side of the electronics racks. The E-block signals were then sent to a 10-fold fast amplifier, whose outputs were the inputs of the FDMTs (described below). The ΔE and Veto signals were sent directly from the patch panel in the electronics shack to the inputs of the FDMTs.

FDMT stands for Fast Discriminator/Mean Timer. The FDMTs used in the experiment were double width FASTBUS modules with 32 analog inputs, designed at PSI to accomplish a number of goals. Among these were: fast discrimination using constant fraction discriminators to minimize signal walk, multiple logic signal outputs for use later in the DAQ and trigger, and analog amplifications (attenuation) of nominally 0.3, and 0.4 for input signals. The analog signals were sent to LeCroy 1885 96 channel FASTBUS charge ADCs where the signals were integrated and digitized. Just as for the cathode signals from the MWPCs, the ADCs were controlled by a LeCroy SMI 1821 Controller.

The logical outputs of the FDMTs consisted of a fast "trigger" output, a delayed TDC output and a spare TDC output. The Mean Timer feature of the FDMTs did not perform with enough stability and was removed. The TDC outputs were delayed by about 300 ns with respect to the trigger output, while the fast trigger output was delayed by about 30 ns with respect to the analog signal input. To minimize signal walk, the discriminators creating the logic signals were constant fraction discriminators. In addition, the CFDs had special circuitry to aid in low ($<$ 1000 hz) frequency noise rejection and were designed to go from totally off to totally on in a 1-2 db range. Ideally, for the LADS experiment, the threshold on the discriminators in the FDMTs was set at 15 mV. Typically, there was ± 3 mV range in the trigger level from channel-to-channel. The processing of the logic outputs and creation of the trigger will be discussed later in this chapter. The logic signals from the PMTs were passed to eleven Phillips Scientific 10C6 32-channel FASTBUS TDCs which converted the signals and suppressed empty channels within 8 μs. The logic signals were also fed to three Phillips Scientific 10C8 128-channel FASTBUS latches.

2.4.3 Trigger Electronics

For the DAQ system to read events which occurred in the LADS detector, a trigger was required. The trigger was a logic signal which told the DAQ computer that the current state of the DAQ electronics was consistent with a meaningful event in LADS and that the computer should read the state of the electronics and write the information to some permanent storage media (in our case 8 mm data tapes). Events in LADS could be attributed to many sources other than to a beam pion interacting with the target nuclei; dark current, cosmic rays and defects in the detection hardware could all generate signals in the detector hardware which appeared to be physical events. In addition, some types of events within LADS, while containing "genuine" pion physics, were not interesting in the sense that previous experiments did a good job measuring such events. A trigger was necessary to reject events not caused by a pion incident on the target and to classify events into types which should contain physics of one type or another. Every event of interest which occurred in LADS had an associated trigger and was classified according to the number of charged and neutral particles in the event.

2.4.3.1 Beam Definition

One must be certain that the events read by the DAQ system were in coincidence with a pion in the beam line. Excluding the cases where there may have been two pions in the beam line was also desired. To accomplish these tasks, a logical BEAM was defined as

$$BEAM = S_{Beam} \cdot S_{Time} \cdot \overline{S_{Time}^{Big} \cdot S_{Time}^{Before} \cdot S_{Time}^{After}} \cdot HODO \cdot Veto \cdot Rf \cdot RunGate. \quad (2.1)$$

S_{Beam} was a logic signal generated by a scintillator counter which was used to define the beam within the LADS volume. The counter was a 1 cm diameter plastic scintillator placed along the beam axis in LADS. S_{Beam} generated a signal when a beam pion, or any charged particle, passed though the counter.

S_{Time} was generated by a relatively large scintillator (~100 mm diameter) placed in front of the upstream endcap. The S_{Time} signal was used as the timing reference for an event within LADS. When the outputs of the S_{Time} PMTs were examined on an oscilloscope, two different amplitude bands could be seen. The brighter, smaller band corresponded to pions in the beam line, while the dimmer, larger band was associated with proton contamination in the beam. A discriminator was used to reject the events which were in the proton band. The discriminator output was named S_{Time}^{Big} which was then used in the BEAM trigger to reject events which were caused by proton contamination in the pion beam.

Positron and muon contamination could also occur in the pion beam. If present, these particles would hit the S_{Time} counter before a pion. A short logic pulse (~5 ns) from S_{Time} was required to be in coincidence with the Rf signal from the ring cyclotron in order to reduce the possibility of muon and positron contamination.

The time scale of events within LADS could be as long as 50 ns for low energy neutrons. To ensure that an event did not have more than one beam particle within the

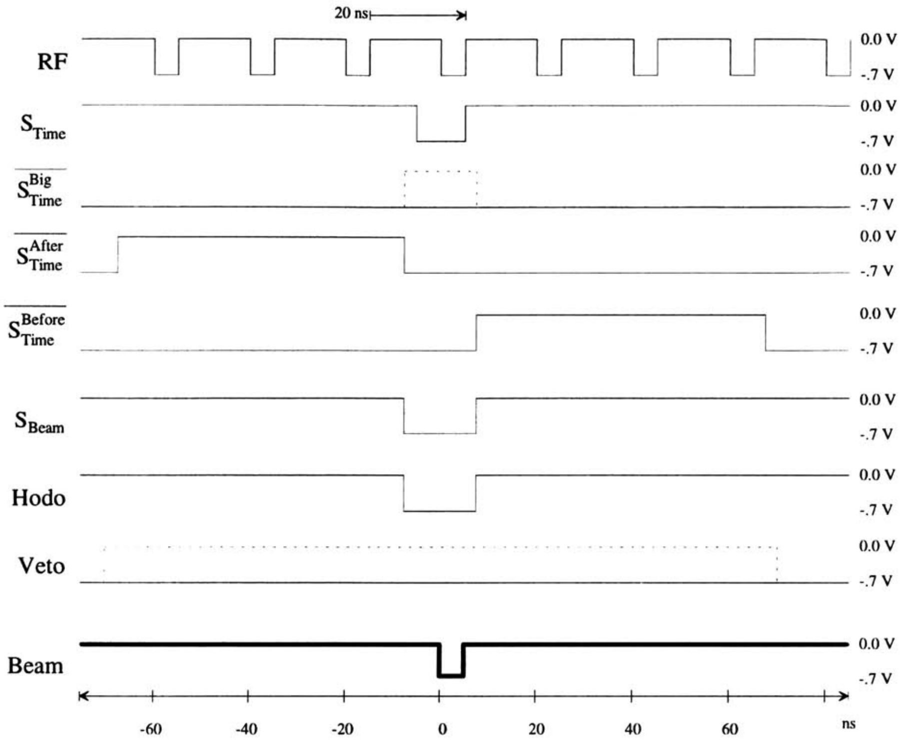

Figure 2-6: A timing diagram for the beam definition.

detector, the S^{Before}_{Time} and S^{After}_{Time} logicals were used. These logicals flagged events which had an S_{Time} signal within ± 60 ns of the BEAM time. The flagged events were rejected.

HODO indicated either that a single particle hit was registered by the hodoscope or that a double hit firing adjacent strips was registered by the hodoscope, reducing the possibility of two beam pions being in the beam line during an event. A schematic of the beam definition timing is shown in Figure 2-6. A signal level of -0.7 V indicates a true state.

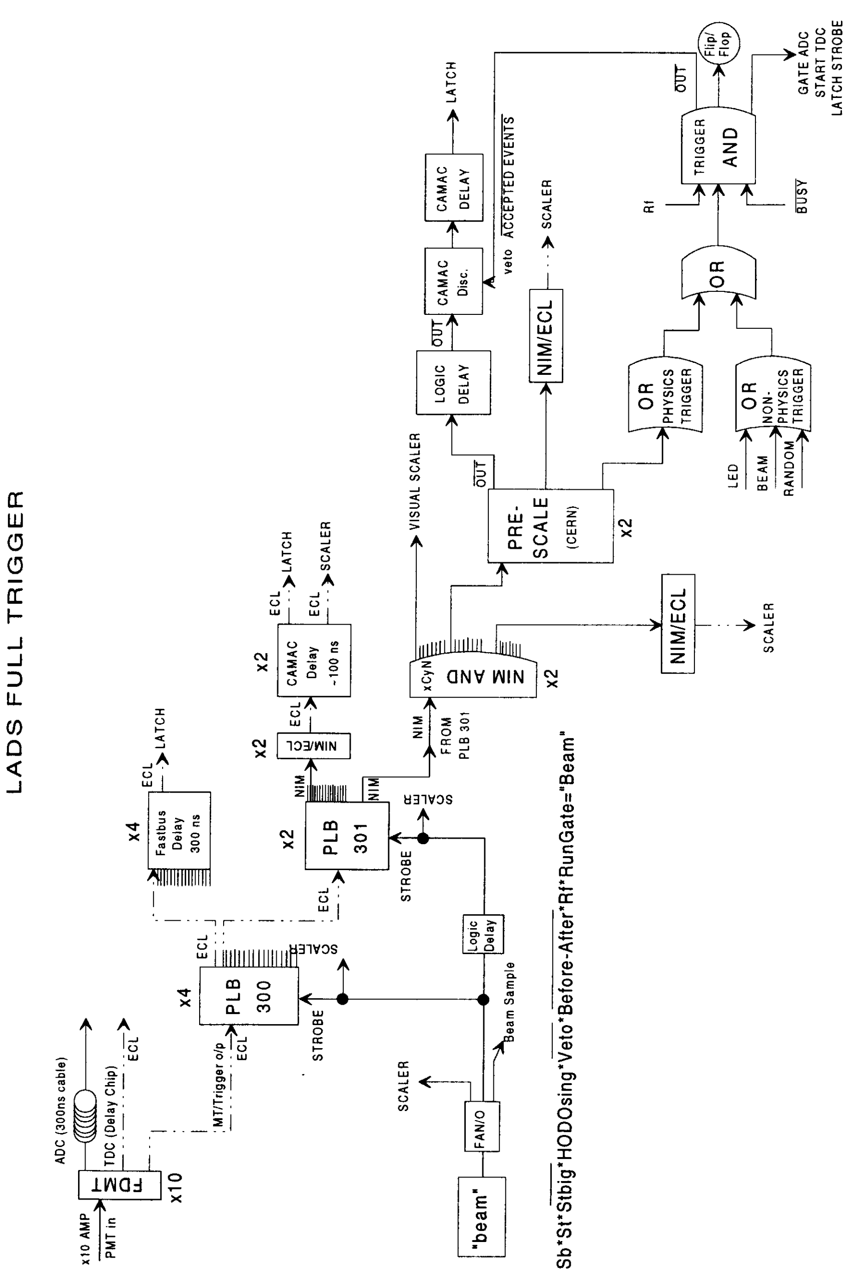

Figure 2-7: The LADS trigger during the 1991 experimental run. The 1993 trigger was similar.

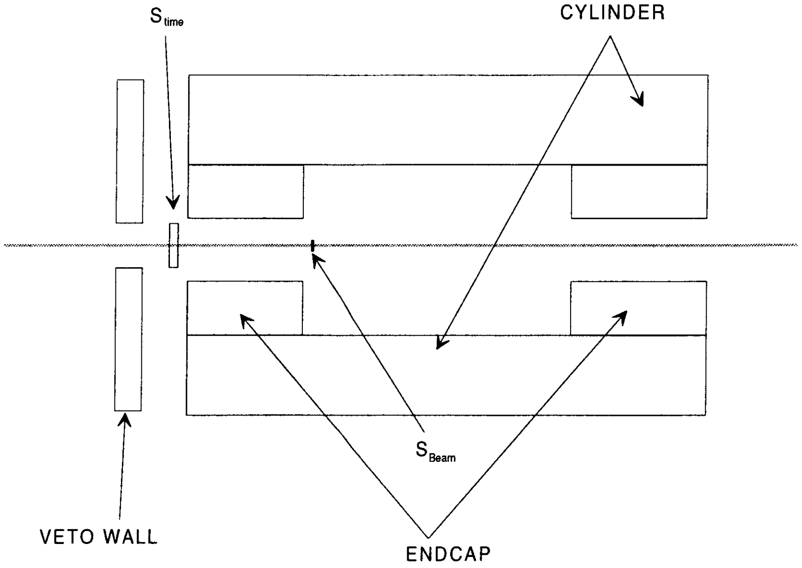

Figure 2-8: A schematic drawing of the LADS detector showing the position of the Veto Wall, S_{Beam}, and S_{Time}.

All particle accelerators experience a phenomenon called beam halo. Halo is caused by many factors including beam particles decaying and beam particles hitting the wall of the beam line. These particles, which make up the halo, are not focused and loosely follow the beam trajectory. Beam halo could cause events within LADS which were determined to be "good"; these events were not useful because they were caused by particles of "unknown" origin and therefore contaminated the analysis. The logical *Veto* was used to reject events that were not coincident with pions that travel through a 120 mm hole in a Pb shielding wall and thus reduced the number of events caused by beam halo. Figure 2-8 shows schematically the positions of the Veto Wall, S_{Time} and S_{Beam}.

2.4.3.2 Event Classification

Because of the large solid angle of LADS and the numerous elements comprising the detector, the event rate exceeded the count rate that could be processed by the DAQ. To help in event selection, the number of charged and neutral particles which comprised the event were determined as well. The amount of charged and neutral particles within an event was an indication of the process that caused the event. By classifying the events according to the number of charged and neutral particles, physics processes were roughly emphasized or deemphasized. The prescaling of event types written to tape accomplished the goal of limiting the data on tape to events that were potentially interesting.

The sheer quantity of electronic hardware used in the gathering of data presented many opportunities for errors to creep into the trigger definition and event classification. As a check, at every stage of the building of the trigger and event classification a sample of the outputs from each stage was sent to scalers and latches. The scalers and latches were reconstructed in software and used to verify that the outputs at each stage were consistent with the inputs. The scalers and latches were also used in the analysis to determine the number of event types which occurred during the experimental run.

The first step in determining the event type was to determine whether the scintillators had fired; this was done with the FDMTs. The logical part of the FDMTs consisted of ECL fast discriminator hybrids developed at PSI. The hybrids had a propagation time of about 20 ns and could go from completely "off" to completely "on" within 2 db of the threshold voltage. The discriminator outputs were split: one set of outputs was sent to the PLB300s (described below) and used to build the event triggers, while the other was sent to the TDCs after a few hundred nanoseconds of delay, and used as the stop signal for the TDCs.

It was the fast discriminator outputs that were routed to PLB300s and used to build the event triggers. The PLB300 was a PSI developed logic module containing Programmable Array Logic (PAL) chips that were set (burned in) to determine if the signals within a detector sector were caused by a charged or neutral particle. The sectors were then classified as charged or neutral and it was also noted whether either upstream or downstream PMTs or both have fired, the latter of which could occur with particles in the cylinder.

After the PLB300s had determined the charge of the particles in LADS, the outputs were routed to PLB301s. PLB301s were also developed at PSI and used EPROMs to count the number of charged and neutral hits (sectors) in the detector. The signals produced were 0c, 1c, 2c, $\geq$3c multiplicities for the charged PLB301 with similar outputs generated by the neutral PLB301. The PLBs were strobed by the logical BEAM signal to give the detector state coincident with a beam pion. The PLB301s produced NIM logic signals as output, which were sent to a NIM AND logic module.

The NIM AND generated the logical event types; these event types were 1c0n, 1c1n, 0c1n, 2c0n, 2c≥1n, 0c≥2n, 1c≥2n, and ≥3c. The output was routed to prescalers which "weighted" events according to the expected physics contained within. Generally, the single particle triggers, *i.e.* those such as 1c0n and 0c1n, were prescaled the most and the multiple particle triggers, *i.e.* 2c≥1n and ≥3c, were prescaled the least. The logical output of the prescalers then was routed to an OR called the physics trigger.

The physics trigger was ORed with a non-physics trigger which consisted of a beam trigger, a random trigger and an LED trigger. The result was the event trigger which signaled to the DAQ computer that something interesting had happened and that the computer should read the information present in the ADCs, TDCs, Latches, etc. To ensure that the DAQ system was ready to take data and that the event trigger was timed correctly, the event trigger was ANDed with the Rf from the cyclotron and the $\overline{busy}$ from the DAQ computer. This combination of event, Rf, and $\overline{busy}$ formed the DAQ trigger which gated the ADCs, served as the TDC start and instructed the DAQ that an event was present and should be written to tape. A diagram of the trigger used in the 1991 experimental run is shown in Figure 2-7. The 1993 trigger was functionally equivalent.

2.4.4 Data Acquisition (DAQ)

All of the data from the ADCs, TDCs, Latches, and Scalers were sent via FASTBUS to the Aleph Event Builder (AEB, STR-501)[121] FASTBUS processor. Each event was approximately 600 bytes long and the AEB buffered the events into 50 event blocks. The 50-event blocks were written by the AEB to dual-ported memory in the FASTBUS-VSB interface (CES FVSBI-9210) from which the data were read, through the VSB bus by a FIC VME processor (CES 8230), and placed in the FIC's data memory. The VME was connected to a VAXstation 4000/90 using a Turbochannel to VME interface (DEC MVIB/3VIA) that could perform programmed transfers (PIO) initiated by the VAXStation or DMA transfers initiated by the VME. The main DAQ process wrote the data to a high density 8500 Exabyte drive. Typical operating rates of the DAQ were 600 events/s. The DAQ was monitored by two other VAXStation 4000/90s: one running the analyzer programs to allow online analysis of the data, the other monitoring data quality for shifts and jumps in the acquired data. In the 1993 experimental run, about 200 5Gb tapes were produced. The data acquisition setup used in 1991 is shown in Figure 2-9.

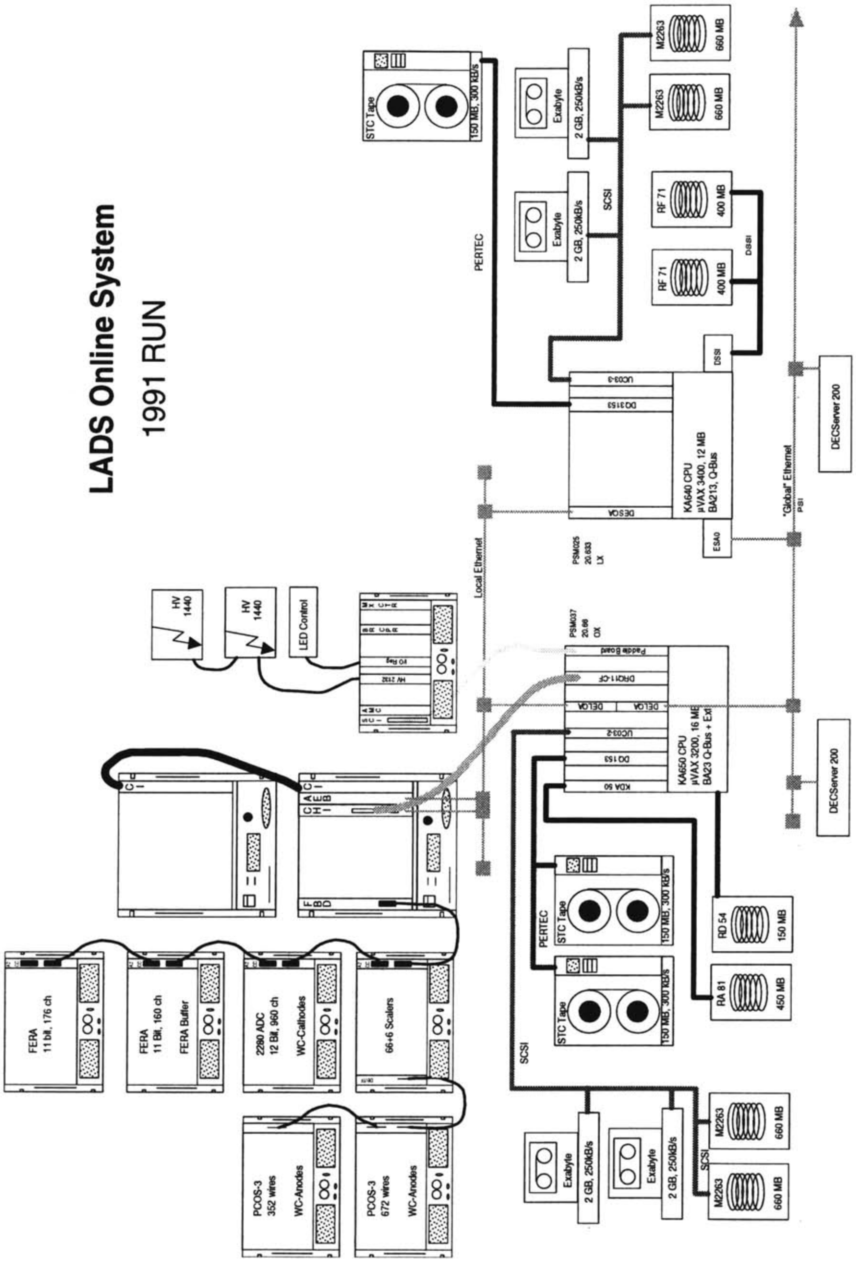

Figure 2-9: The DAQ setup used in 1991, the 1993 was similar.

Chapter 3

Data Analysis Tools and Calibration

The best data in the world taken on the best detector in the world are worthless if they can not be subsequently analyzed. LADS is no exception. In fact, there usually is interest in examining the data as they are taken online to run consistency checks and monitor detector performance. Analyzer programs are written to accomplish this. For LADS, data analysis was accomplished through the use of two programs, LADYBIRD and LARK. LARK was a front-end program which allowed the researcher to actively communicate with LADYBIRD, and LADYBIRD was the analyzer program that processed the data and extracted the physics quantities of interest. Both programs were run in a DEC VMS environment (either Alpha or VAX), and in total consist of about 500 subroutines. LARK will not be further discussed here, as the important features of the analysis came from LADYBIRD.

LADYBIRD read in the data online from the data stream and off-line from 8mm tape into one large ($\sim$ 26,000 element) array called the xl_d, which was held in a common block to allow access from the various analyzer subroutines. Various tests could be set on the data in the xl_d including tests of specific bits and geometrical cuts – such as linear, hyperbolic and ellipsoidal – of one variable against another. Also, any tests could be combined with logical NOT, AND, OR and XOR to make more complex test patterns. These tests were evaluated on an event-by-event basis and the results were used to fill histograms if the outputs of specific tests were true. In addition, LADYBIRD incremented software scalers every time a test was true. To aid the researcher, LADYBIRD's runtime behavior could be changed by setting various switches to allow for efficient analysis of the data.

There was a significant amount of code that formed the infrastructure of LADYBIRD. This code was responsible for handling the communication of processes involved and the movement of data among global memory locations, as well as the above described tests. This code will not be elaborated on further. Instead, I will describe what was known as the physics package of LADYBIRD. The general components of LADYBIRD are represented in Figure 3-1.

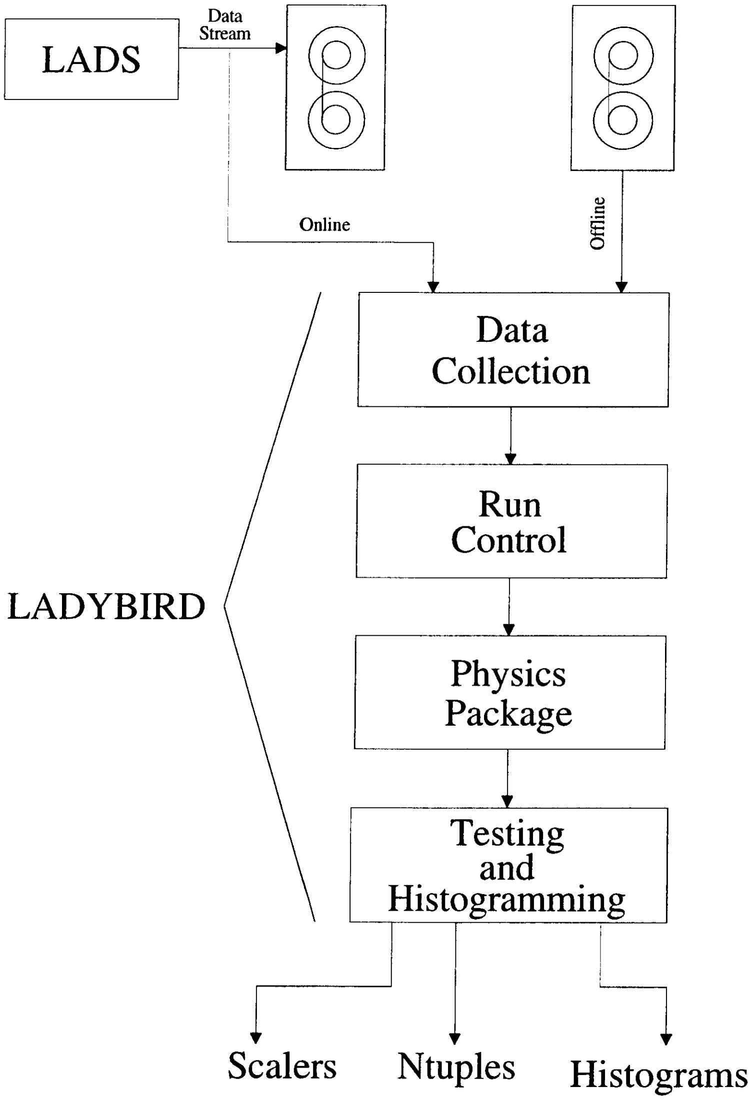

Figure 3-1: The major components of the LADYBIRD package.

3.1 Processing of an event.

LADYBIRD could perform analysis both online during data taking, as well as offline for a more complete analysis of the data. When analyzing online, LADYBIRD examined only a sample of the data being sent to the DAQ, since the main purpose of analyzing online was to monitor data quality and ensure that no major disasters had happened. Offline time was a little more flexible and in this case every event from tape was read and analyzed. In both cases, though, there was a common treatment of the data that happened for each event. For each event, the data were preprocessed to ensure data quality. Next, hits in the plastic scintillators were converted to particles and the particles' trajectories were reconstructed. At this point, the particles were identified, energy loss calculations were performed, and finally, kinematic information was calculated. This is summarized in Figure 3-2.

3.1.1 Data preprocessing

When offline, the data were read from tape and copied to the xl_d. Correction subroutines were run on the data to fix any cabling mistakes made during the experimental runs and consistency checks were performed to verify that the hardware was performing correctly. These checks included comparing the output of the latches to the multiplicities of fired counters and verifying that the trigger performed correctly.

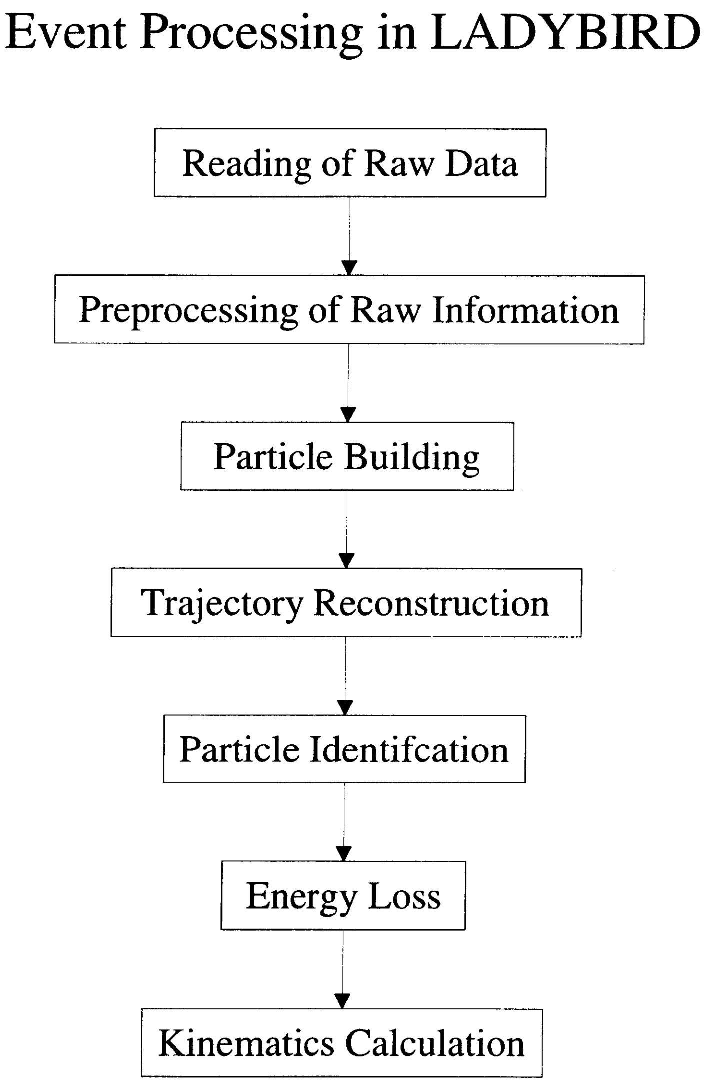

Figure 3-2: The processing steps for each event processed by LADYBIRD.

The plastic information read from tape (the raw scintillator signals) were converted into calibrated values. In addition, it was required that the counter in question provide full information. This meant that for each counter in question, each ADC and TDC which should have fired had an associated signal. So for the cylinder plastics, both ADCs and both TDCs must have had measured signals.

Also during event preprocessing, the values from the TDCs were converted into nanosecond values and in the case of cylinder counters, a mean time was calculated for later use. The raw ADC values were converted into calibrated light values, and for cylinder counters the geometric mean of the upstream and downstream ADCs was used to determine the light deposited by the particle.

At this point, the raw chamber information was also processed. This was used later to determine the trajectories of the particles and was done using the ADC values of the cathode strips on each of the cathode planes as well as the wire number of the anodes which fired.

The first step of preprocessing the chamber data was to determine which anode wires fired and their position. Next, dead cathode strips were filled with interpolated values from neighboring strips. The reconstruction code then iterated through each of the cathode planes looking for peaks corresponding to an amount of charge of a certain threshold left by the passage of an ionizing particle. If too many peaks on a cathode plane were found (more than four), the threshold was raised and the peak search was repeated.

After the peaks were found and identified on the cathode planes, the possible permutations of matches between the inner and outer cathode place were compared to determine which permutation was optimal. The ϕ positions of the crossings for each permutation were compared with the ϕ values of wires that fired. If a wire had fired, that pairing of inner and outer planes was taken as the correct match. If, because of ambiguities, there were two possible wire matchings, both were retained as possible matches. The permutation which resulted in the largest number of matchings was selected as the correct matching. If more than one permutation had the maximum number of matchings, the best permutation was chosen by a least squares fit of the integrated strength of the peaks' pairings. This assumed that peaks formed by the same particle had the same strength. Later, the track reconstruction portion of the code must match the optimal permutations on each chamber with particles determined in particle building.

3.1.2 Particle Building

A detector supplies information about which counters have fired and in what configuration. The experimenter, on the other hand, is interested in particles and their number, type, energies, and trajectories in each event. Particle building, when combined with track reconstruction, helps to provide this information for the scientist.

The event topology was determined in a section of code called "counter-to-particle" (CTP). In the first step, the code looped over cylinder ΔE counters counting each one that fired as a charged particle. The light from E-blocks directly behind a fired ΔE was associated with the same charged particle. If an E-block fired with no associated ΔE, its energy was assigned to a neutral particle.

The next step was the reconstruction of particles in the endcap. This was slightly more difficult because the endcap ΔE counters overlap with adjacent endcap E-blocks, but the principle was the same. Again, a charged particle was associated with each ΔE that fired and the light in any E-block behind the ΔE was associated with the charged particle. Then any E-block which fired without a ΔE was identified as a neutral particle.

After particles were assigned to cylinder and endcap counters, the next step was to deal with neutral particles adjacent to charged particles. It was possible for a particle to scatter from one sector to another. In fact, for an energetic proton the likelihood was about 30%. Because of this, any neutral particle sector which was adjacent to a charged sector was reassigned to be from the charged particle. There was one difficulty with removing adjacent neutrals, namely that, events which had real neutrons nearly parallel with real protons (for example soft-FSI events) were redefined instead to be a single charged particle.

Finally, with regard to particle building, punch-through particles were reconstructed. "Punch-throughs" were particles which intersected both the endcap and the cylinder. These particles were selected by determining if a signal in both the endcap and cylinder were consistent with a single particle.

3.1.3 Trajectory Building

With all of the plastic counters assigned to particles, the next step was to assign the wire chamber hits to charged particles and determine particle trajectories and an event vertex if possible. This was done using the various L_TRACKS* subroutines.

The first step in determining particle trajectories was to loop over the cylinder charged particles determined by CTP (those particles which had an associated fired cylinder ΔE). Possible hits were assigned to all particles with outer chamber hits within a certain ϕ and z tolerance. Then particles that had only one possible outer chamber hit were matched. After the unambiguous hits were assigned, particles with two or more possible outer chamber hits were assigned with preference given to hits that had an associated wire hit. Finally, assignments were made to outer chamber hits which had no cylinder ΔE associated. These were done in a manner essentially the same as described above. At this point all the outer chamber associations were done.

The next step was to associate inner chamber hits (both inner chambers) with particles which had an outer chamber hit. Similar to above, all hits that fell within a certain ϕ tolerance were assigned to particle hits in the outer chamber. If there were enough possible tracks to find a two track vertex, then all the possible hits were looped over until two tracks were found that traced back to a common point (within 4cm of the beam axis). The distance of closest approach of the two tracks was assigned as the event vertex. After an event vertex was formed, the other inner chamber hits were assigned by minimizing the track distance to the vertex and the ϕ differences between the outer and inner chambers.

If it was not possible to form a vertex with two tracks, all matches that had exactly a one-to-one correspondence were assigned. If there is greater than one match, preference was given to the non-punch-through match. The intersection of this track with the beam axis was defined to be the event vertex.

At this point all that were left over were inner chamber hits which did not have an associated outer chamber hit. If the plastic had only one possible inner chamber hit, the hit was associated with that particle. For ambiguous matches, preference was given to associations in which both inner chambers fired. The remaining ambiguous matches were assigned by a global fit which minimized the ϕ differences.

3.1.4 Particle Identification

After trajectory building, there was enough information to determine the particle identification (PID). Both time-of-flight (TOF) *vs.* energy and dE/dx *vs.* energy information were used to determine PID.

$E - dE/dx$ used the fact that when a particle traverses a thin scintillator (*i.e.* loses only a small fraction of its energy) the amount of energy deposited is approximately proportional to the square of the ratio between the charged particle's mass and its velocity. When a particle stops in a scintillator, on the other hand, all of the energy is deposited. Since a particle's kinetic energy is a function of its mass and velocity, it was possible to use the above measurement of the particle's kinetic energy (E) and its velocity (dE/dx) to determine the charged particle,s mass.

$E - TOF$, on the other hand, used the particle's β as the measure of the particles velocity. The plots otherwise were quite similar (see Figure 3-3.)

There were four separate PID tests used to determine particle types.

- dE/dx *vs.* E in the cylinder

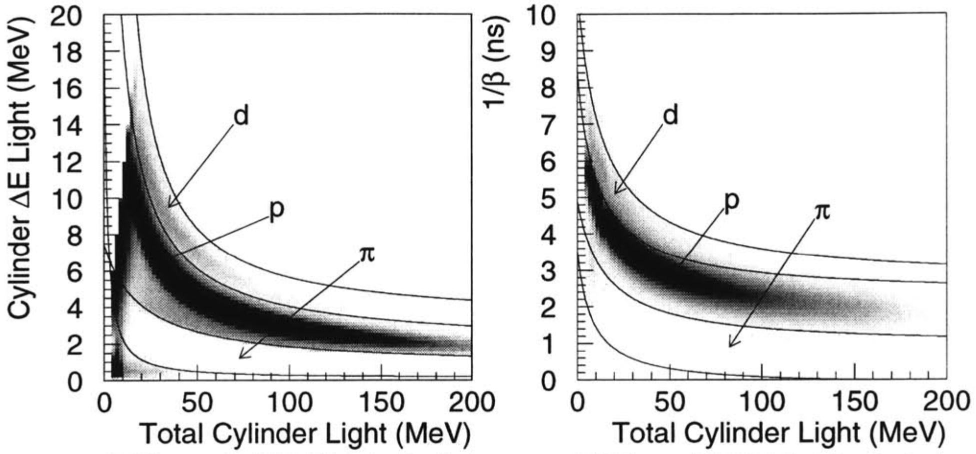

dE/dx vs. E PID Plot (cylinder)

TOF vs. E PID Plot (cylinder)

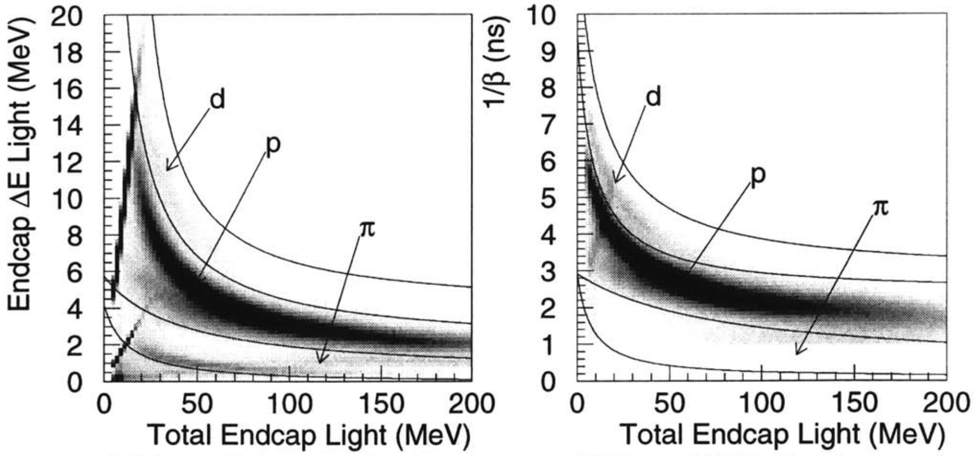

dE/dx vs. E PID Plot (endcap)

TOF vs. E PID Plot (endcap)

Figure 3-3: Example of the PID curves used in this analysis. The histograms are reconstructed from partially processed experimental data, and therefore most of the pion events are rejected.

- TOF *vs.* E in the cylinder
- dE/dx *vs.* E in the endcap
- TOF *vs.* E in the endcap

To determine which method was used in PID, a strict hierarchy was followed.

- If the charged particle deposited at least 10 MeV of light in a cylinder E-block, the dE/dx *vs.* E method was used.
- If the charged particle did not deposit 10 MeV of light in the cylinder E-blocks but did so in the endcap E-blocks, then the dE/dx *vs.* E method in the endcap was used.
- If neither of the above was true, but the endcap ΔE fired and β was calculable for the endcap, the TOF *vs.* E in the endcap method was used.
- If none of the above was true, then TOF *vs.* E in the cylinder was used to determine PID.

The above method was also used for clean punch-through particles, *i.e.* those which had not reacted in the E-block causing multiple cylinder ΔEs to have fired. For non-clean punch-throughs, the endcap dE/dx *vs.* E method was given most precedence, then

TOF vs. E in the endcap, followed by dE/dx *vs.* E in the cylinder, and finally *TOF vs.* E in the cylinder.

3.1.5 Energy Loss

Now that the particles were identified and their trajectories determined, it was possible to determine their energy at the event vertex. There were two major factors which must be corrected for, saturation of the scintillator and energy loss in non-scintillating material.

Saturation of the plastic scintillator comes about because the light output of the scintillator is not a linear function of the converted kinetic energy of the detected particle. A charged particle passing through plastic scintillator ionizes the material leaving electron-holes. These holes are filled with electrons from the electron sea in the material. It is this de-excitation of the sea electrons which determines the light output. If any energy above the ionization potential is carried off by the initial excited electron, it will not cause an increase in the resulting signal, and therefore that amount of energy will be lost. Lower energy particles spend more time in the vicinity of each electron and thus more energy is typically transferred. Because of this, the light output of the scintillator is less than would be expected for the amount of deposited energy. The scintillator is said then to be "saturated". This effect is only important for the last ≈ 10 MeV of particle energy deposited, and is well known and could be accounted for with appropriate formulae [122].

Energy loss in non-scintillating material was corrected for by tracing the path of the particle through the layers of material which it should have traversed on its way to the plastic scintillator. Starting from where the particle hit the plastic in the detector, its route was traced backward and the energy that it should have lost was determined successively by calculating the energy loss from an exponential fit to energy loss and range tables. The energy loss was different for each particle type and required a different exponential fit. For particles with less than 20 MeV of detected light, a more accurate determination of the energy loss was done by an interpolation from tables.

3.1.6 Kinematic Quantities

At this point, all of the basic information for each particle that could be determined has been determined. Now various kinematic quantities, such as invariant mass and missing momenta, could be determined. The quantities determined were dependent on specific event topologies, and the quantities to be determined were largely left to the individual user through the use of various switches in the analyzer subroutines.

3.2 Calibration

Of course, all of this hard won information is useless if the detector is not calibrated so that accurate energy and trajectory information can be determined. There were, as is becoming obvious, two main detector element families that needed to be calibrated. These were the plastic scintillator counters and the wire chambers. Calibration was an iterative process with the plastics done roughly at first so that the wire chambers could be calibrated. The calibrated wire chambers were then used to improve upon the plastic calibration.

3.2.1 Wire Chamber Calibration

The calibration of the wire chambers involved two steps. In the first step, the positions of components within individual chambers were adjusted. The second step involved positioning the chambers relative to the LADS detector. The intra-chamber calibrations involved adjusting the relative positions of the cathode strips with respect to each other and with respect to the anode wires. This was necessary because the origin of the wire chamber coordinate system (0° and $z = 0$) was defined in the software as the point where the first wire ends on the upstream edge of the chamber. The software also assumed that the first inner and outer cathode strips intersected at this origin. Physically this was not the case, so offsets of the cathode strips were adjusted until the correct active length for the chamber was achieved.

Once the intra-chamber calibration was complete, the chambers were positioned correctly relative to each other. This was done using the reaction ^{2}H(π^+,pp) and exploiting its back-to-back nature. The chambers ϕ and z positions were adjusted in software until the outgoing protons were 180° apart in θ and ϕ in the $\pi - {}^2$H CM system. With the chambers properly calibrated, angular resolutions on the order of 1° in both θ and ϕ were achieved. Also, because of the calibration, vertex resolutions better than 1mm were achieved.

3.2.2 Plastic Calibration

Aside from a rough plastic calibration, there were two major steps involved in calibrating the plastic counters. These were an absolute calibration and a fine calibration. Absolute calibration was done using reactions which could be kinematically determined using only wire chamber information. The main calibration reaction was ^{2}H(π^+,pp). Also used were ^{3}He(π^+,ppp) and ^{4}He(π^+,ppd). These systems are kinematically determined if one knows the particle type, so a very rough initial plastic calibration was needed to proceed.

In the absolute calibration step, linear transformations of ADC values to energy were determined for each of the individual counters. Using the polar and azimuthal angles of the particles, the vertex energy of the particles could be calculated. The particles were traced from the interaction point to the scintillator counters, and a procedure similar to L_ELOSS was used to track the particles through the material in the detector to determine the amount of light deposited in each scintillator counter. Other than saturation effects which were corrected for, the light was assumed to be a linear function of the amount of energy that a charged particle deposited. The absolute gain was the ratio of the expected light to the measured light in a counter.

Because a particle which deposits zero energy would not get a detector response, only a scale factor for each sector i had to be determined. For the cylinder, the effect of light attenuation along the length of the scintillator material was negated by using the geometric mean of the light detected by each PMT. This allowed the gains for two PMTs to be adjusted simultaneously and self-consistently. It was desired, though, to calibrate each PMT individually, so the MWPCs were used to determine where each particle hit the plastic counter to obtain an attenuation length for each sector and therefore calculate the scale factor for each individual PMT.

The TDC calibration of the ΔE counters was also accomplished using kinematically determined systems of charged particles. The calculated times-of-flight were compared with the measured times-of-flight to determine the TDC offsets. It was not possible to use charged particles to calibrate the E-blocks because of their deceleration on the way to the counter. Instead, the neutron from the kinematically overdetermined system $^4\mathrm{He}(\pi^+, pppn)$ was the preferred particle for TDC calibration of the E-blocks. It was also possible to use the photons from SCX reactions to calibrate the TDCs as their times-of-flight were independent of their energy.

The above calibration method allowed for energy calibrations with a FWHM of about 6% for an absorption event. This was not nearly as good as the 2.5% obtained during the design phase of the detector using mono-energetic protons to test the cylinder E-block setup. To obtain energy resolutions much closer to that which was achieved when testing a prototype of the E-block counter system, a fine calibration procedure was developed. In this procedure, the ADC signals were corrected for non-linearities due to geometric and electronic effects. The light output for each counter group was calculated from kinematically overdetermined systems and was compared to the measured value. A second order polynomial was then fit to this correlation which improved the achieved energy resolution greatly. In fact, the energy resolution achieved was the same as that specified in the design goal of the LADS detector, with the summed energy peak of the two outgoing protons following absorption on the deuteron having a FWHM of 2.5% and for ^{3}He, 3.0%.

Chapter 4

Data Analysis and Partial Cross Section Results

The goal of this thesis is two-fold. One is to obtain an accurate measurement of the pion total absorption cross section on Xe for incident pion energies across the Δ resonance. The other goal is to determine the decomposition of pion absorption on Xe into various reaction channels. This chapter will describe the procedures used to extract absorption events from the data taken as well as the procedures followed to obtain the beam normalization. Then this chapter will discuss how the total absorption cross section can be obtained through an extrapolation over unmeasured regions of phase space.

The total absorption cross section is defined as:

$$\sigma_{abs}(\text{mb}) = \frac{N_{abs}}{N_{\pi} \times \rho_{target} \times L_{target}} \times \frac{1}{\Omega} \times 10^{-27}. \tag{4.1}$$

Where N_{abs} is the number of events detected which do not have a pion in the final state, N_{π} is the number of pions incident on the target cell, ρ_{target} is the number of target nuclei per cubic centimeter, L_{target} is the length of the target in centimeters and Ω is the acceptance of the detector.

The determination of Ω depended upon the specific channels which contributed to the total detected absorption cross section and will be described later in this thesis in Sec. 4.4. Because each of the competing channels had a different acceptance based upon the kinematic distributions of the particular channels, the determination of the total absorption cross section required that it be decomposed into the competing channels. This can be represented as the sum over all the competing channels i as follows:

$$\sigma_{abs}(\text{mb}) = \frac{1}{N_{\pi} \times \rho_{target} \times L_{target}} \times \sum_{i=1}^{N_{chan}} \frac{N^{i}_{abs}}{\Omega_i} \times 10^{-27}, \tag{4.2}$$

where N^{i}_{abs} is the number of events from a particular channel i and Ω_i is the acceptance for that particular channel.

Determining N_{abs} required isolating the events which have come from the target gas and then eliminating those with a pion in the final state. Charged pions were eliminated relatively easily with charged particle PID. Events with neutral pions were suppressed by rejecting events containing high energy γs, as well as subtracting from the measured yields the expected SCX contamination based upon the measured γ detection efficiency of the LADS detector.

4.1 First Stage Analysis – Writing Raw Ntuples

The extraction occurred in three separate steps. First, the data were processed by LADYBIRD which rejected bad beam events, required that the events originate from within the target cell, performed charged particle identification, and rejected events which contained a charged pion. The data from this extraction were written into a file in PAW NTUPLE format and included the variables necessary for further analysis. Also during the first stage of analysis, the determination of beam normalization as well as correction factors due to event prescaling and dead time were done with the aid of LADYBIRD.

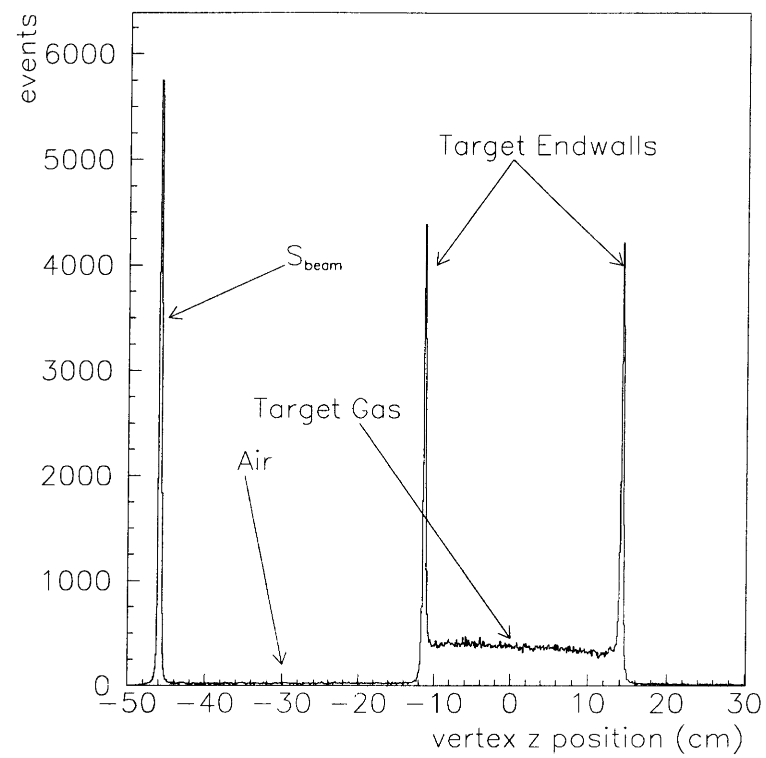

Figure 4-1: The z-position of the event vertex. The target gas as well as the target end walls are clearly seen.

4.1.1 Isolation of Events Coming from within the Target

The first step in the analysis involved the elimination of events which did not come from within the central region of the target (see Figure 4-1). Events which did not originate within the central 20 cm of the target were eliminated. Performing this cut eliminated the background from the target end walls, the air and the beam defining counter. Also, to isolate events which occurred within the target, a cut on the radius of the event vertex was performed, rejecting events which were determined to come from farther than 1.5 cm from the longitudinal axis of the target. This had the effect of eliminating background from the target walls.

While an accurate determination of the z-position of the target could be made with an event that had only one charged particle which had hits in the inner and outer chambers, the r-position of the event could not be determined as accurately unless two tracks were used to form an event vertex. Because of this, a requirement was set later in the analysis to require two-track vertices. While every absorption final state must have at least one charged particle, mandating a two track vertex required that two charged particles be in the detector. Events excluded by the two track requirement must be corrected for by extrapolation.

4.1.2 Charged Particle Identification

Charged particle PID was performed using the standard LADYBIRD PID machinery as described in the previous chapter. Using this machinery, the events which contained charged pions were removed from further analysis. In addition, protons and deuterons were identified for use later in the analysis.

4.1.3 Beam Normalization

In order to obtain a cross section, the amount of beam incident on the target was determined. The number of incident pions during the experiment were counted by the beam scaler. A correction factor to the amount of beam hitting the target had to be applied because there were cuts applied to the beam counter's ADC and TDC values to ensure that only events which contained good pions were analyzed. Typical cuts are shown in Figures 4-2 and 4-3. The ADC cuts were used to reject events where the ADC failed to fire and events in which the beam pion lost too much energy in the beam counter. The TDC cuts rejected events in which the pion did not pass through the beam counter as well as rejecting events which were caused by electron and muon contamination in the beam. To determine the fraction of the beam removed by the ADC and TDC cuts, events which were triggered only by the beam counter were passed through the same ADC and TDC cuts. The uncertainty in the number, which was negligible for the 1993 experimental run, was statistical and therefore only depended upon the amount of beam sample taken during the experiment.

Also affecting the beam normalization was the fact that pions could have decayed on the way from the beam counter to the target. The percentage of the beam which decayed depended upon: the velocity of the pion, the distance from S_{beam} to the target cell, and of course its mean lifetime, by the relation $N/N_0 = e^{(-lm_\pi/\tau p)}$ where l is the

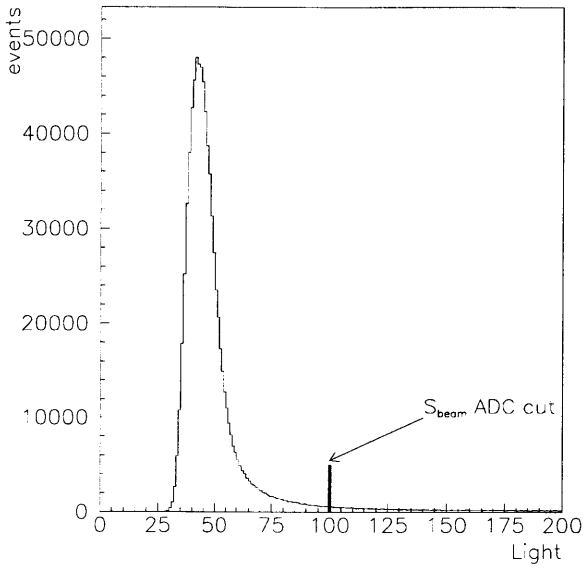

Figure 4-2: Typical cut applied to the ADC value of the S_{beam} counter.

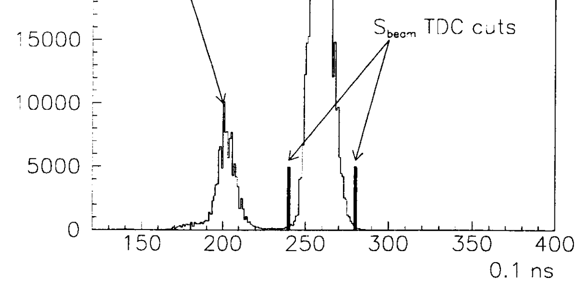

Figure 4-3: Typical cuts applied to the TDC values of the S_{beam} counter.

distance to the target, τ is the mean lifetime, and p is the pion's momentum. The largest uncertainty was the distance to the target and it was known to better than 5% which led to a negligible uncertainty in the amount of pions that decayed (about 1/10 %).

Another factor affecting beam normalization was the fact that pions could have reacted before reaching the target. By using known pion reaction cross sections for the materials which the pion passes through from S_{beam} to the target gas, it was possible to compute the percentage of beam lost due to pion reactions not in the target. The amount of materials between S_{beam} and the target gas was known to better than 10% and the total pion reaction cross sections were known to within 25%. To be generous, an uncertainty of 30% of the size correction factor was taken as the error. Because this correction was quite small, the error introduced into the beam normalization was quite small.

Any pion beam will have some muon contamination and TURTLE[123] calculations were run to determine the amount of muon contamination in the beam. From comparison with earlier experiments, it was determined that the amount of muon contamination was known to within 1%.

By far the largest source of uncertainty in the beam normalization measurement came from the correction due to the number of pions missing the target. Because of beam optic effects as well as multiple scattering of the pions, it was possible that pions which were counted by the S_{beam} completely missed the target cell. To determine the amount of beam missing the target, pion reactions in the air before and aft of the target cell were used. To reduce the number of spurious events as well as to accurately determine the $x - y$ position of the event, only events which had a vertex created from two tracks as well as wire chamber information for all charged particles were considered. In addition, the distance of closest approach of the track forming the event vertex was required to be less than 1.5 cm. The reconstructed vertices were examined both before and aft of the target cell. The fraction of the beam missing the target was determined by using the average of the upstream and downstream values of the ratio

$$R_{miss} = \frac{\text{events within 1.5 cm of the } z - \text{axis}}{\text{events within 4 cm of the } z - \text{axis}} \tag{4.3}$$

(see Figure 4-4). Events which had a vertex outside of 4cm from the z-axis were assumed to be misreconstructions. This correction factor assumed that the beam spread linearly from the upstream end to the downstream end of the target and that the amount of misreconstructed vertices was much less than correct vertex reconstructions. The uncertainty associated with the R_{miss} measurement was taken to be one third the value of the difference between the upstream and downstream measurements. The correction factors as well as the total uncertainty in the beam normalization are summarized in Table 4.1.

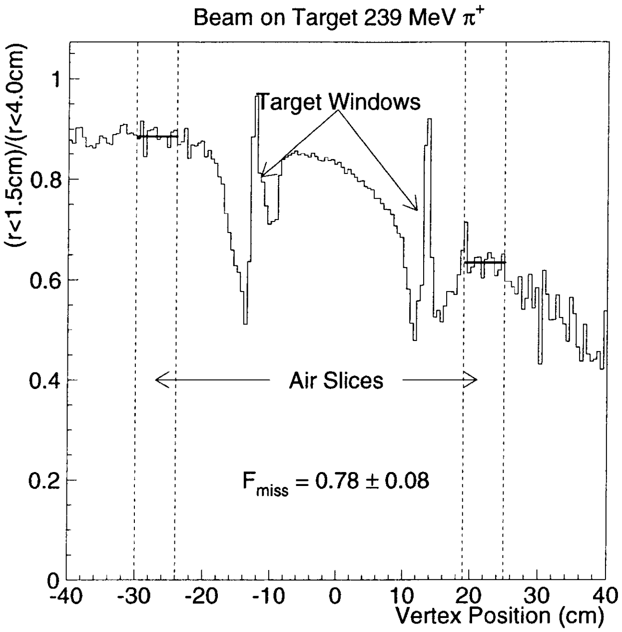

Figure 4-4: The ratio of beam inside and outside of the target radius cut showing the position of the slices used to determine the amount of beam missing the target.

Beam Corrections						
Energy (MeV)	$R_{S_{Beam}cut}$	R_{contam}	R_{react}	R_{decay}	R_{miss}	R_{Total}
118	0.84	0.98	0.982	0.973	0.67 ± 0.15	0.53 ± 0.12
162	0.74	0.982	0.978	0.975	0.70 ± 0.13	0.485 ± 0.09
239	0.81	0.982	0.983	0.979	0.78 ± 0.08	0.597 ± 0.06

Table 4.1: Correction factors applied to the S_{Beam} scaler.

4.1.4 Prescaling and Dead Time Corrections

The final set of quantities determined in the first stage of the data analysis was the prescale and dead time correction factors. The prescale factors were set during the data taking to emphasize potentially interesting triggers and to deemphasize the potentially less interesting triggers. The all neutral and single charged trigger types were prescaled the most, and the $\geq$3c trigger type was prescaled the least. The dead time correction factors reflect the fact that the events of different triggers types took different amounts of time to be processed by the DAQ and written to tape. The prescale factor was set during the experimental run and the deadtime correction factor was determined by dividing the number of valid events of a particular trigger type by the number of events of that trigger type written to tape. The prescale and dead time correction factors are summarized in Table 4.2

4.2 Second Stage Analysis

The second stage of data analysis involved determining event kinematics, performing neutral particle identification, and determining the particle multiplicities for each event type. The final stage of the experimental data analysis, discussed in Sec. 4.3, consisted of counting the particle multiplicities for each event.

Prescale and Deadtime Corrections				
Trigger Type	Prescale Factor	Deadtime Correction Beam Energy (MeV)		
		118	165	239
0c1n	256	1.87	3.11	6.63
1c0n	256	1.88	3.01	6.51
1c1n	32	1.85	3.03	6.53
2c0n	4	1.68	2.66	5.79
0c≥2n	128	1.87	3.12	6.60
2c≥1n	4	1.74	2.59	5.48
1c≥2n	32	1.87	3.09	6.53
≥3c	1	1.89	3.13	6.65

Table 4.2: Prescale and deadtime correction factors for the various trigger classes.

During the second stage of analysis, only events with vertices calculated from two tracks were accepted so that a reliable radius cut on the event vertex could be made. In addition, each event was checked to verify that it indeed was good, *e.g.* the event vertex was within 1.5 cm of the beam axis and all charged particles had an associated wire chamber hit. In addition, if the particle happened to be in the punch-through region, the PID was adjusted accordingly.

Each event was then processed on a particle by particle basis, verifying for protons and deuterons that: each particle's kinetic energy was above the minimum threshold of 30 MeV; and, to eliminate events near the edge of the detector's acceptance, that each track's polar angle was within 15° and 165°; and finally, that each track pointed back to the event vertex. If the above conditions were not met, the particle was ignored in further

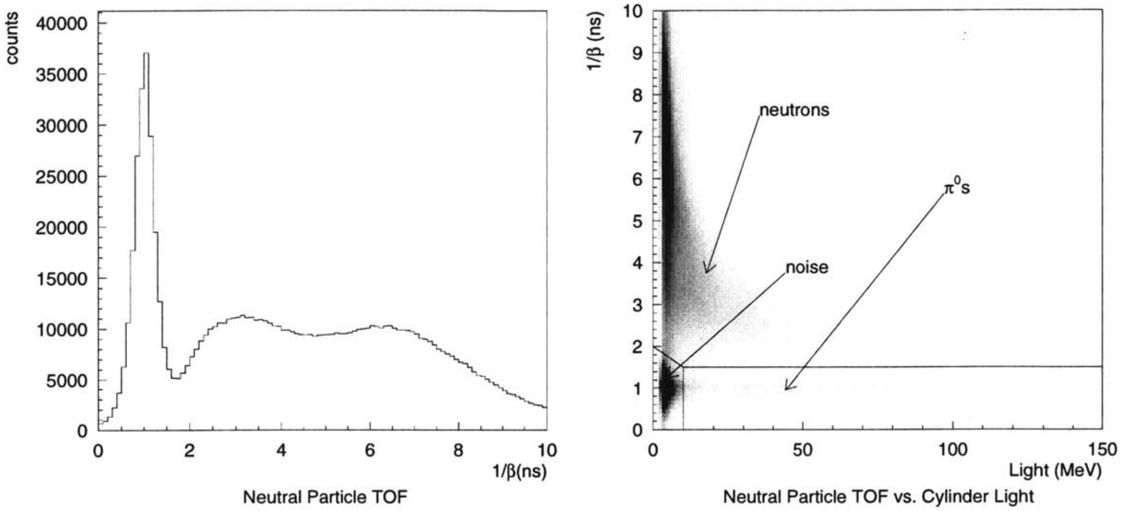

Figure 4-5: Neutral PID plots. The left plot is the reduced time of flight $(1/\beta)$ of neutral particles. The right plot shows the contours used to identify neutral particles in the second stage of the analysis. "Noise" also includes γs from nuclear de-excitation.

analysis. The cut on the polar angle reduced the angular acceptance of the detector to $\sim 96\%$ of 4π.

Neutral particles were first processed by assigning a particle ID according to the contours in the right plot of Figure 4-5. For each particle determined to be a neutron, its kinetic energy was checked to see that it was above 30 MeV. Any neutron with less than 30 MeV kinetic energy was considered an evaporation neutron. Also, the non-evaporation neutron's angular information was verified. Similar to charged particles, if the neutral particle failed these checks, it was ignored in further analysis.

Finally any charged pions that managed to make it this far through the analysis chain were examined. If their kinetic energy was less than 15 MeV, they were assumed to be noise and ignored. Events which had higher energy charged pions were rejected.

During this neutral particle identification, angle verification, and threshold application, the number of particle types p, d, n, γ and π^0 in each event were counted for inclusion in the output ntuple. The particles were then sorted according to energy and particle type and the various event kinematics – including the total energy, the missing momentum, the missing mass, and the total kinetic energy – were calculated.

4.3 Experimental Particle Multiplicities

The third and final stage of the data extraction was the determination of the particle multiplicities. In this stage, the events were weighted according to their trigger type determined in the first stage of the analysis and various kinematic quantities were plotted for each class of events *e.g.* $2p$, $2p1n$, $2p2n$, $2p3n$, $3p$. These quantities were the kinetic energy and polar angle of every detected particle as well as the missing energy and missing momentum for each event. For this analysis, the missing energy was defined as:

$$E_{miss} = T_\pi + m_\pi - \sum_{i=1}^{n} T_i + Q, \tag{4.4}$$

where T_π is the pions kinetic energy, m_π is the pions mass, T_i is the kinetic energy of the detected particle i, and Q is the reactions Q-value, which is the energy required to remove the n particles from the target nucleus. For states where all of the emitted particles are detected, E_{miss} is the excitation energy of the nucleus minus its kinetic energy (which is small). In addition, the missing momentum was defined as:

$$\vec{P}_{miss} = \vec{p}_\pi - \sum_i \vec{p}_i, \tag{4.5}$$

where $\vec{p}_i$ is the momenta for a particular detected particle i.

To determine the yield for each event class, the polar angle distribution of the charged particle (proton, if possible, otherwise the deuteron) was integrated and corrected for the charged particle multiplicity. For the $2n$ events, obviously, the neutron was used. The raw experimental yield was then obtained for each event class. Combining the experimental yield with the beam normalization information from the first stage of the analysis as well as the target density described below, determined the detected multiplicity cross sections as well as a total non-acceptance corrected experimental cross section. Also determined at this stage was the amount of background due to undetected SCX events.

4.3.1 SCX subtraction

While LADS had a reasonable detection efficiency for photons in the energy range of those produced by the decay of the π^0, it was not 100%. Therefore, the cuts used to remove the SCX events underestimated the SCX contamination in the data sample. To correct for this, the data were analyzed looking specifically for events in which a high energy γ was detected. These events were subtracted from the signal data. A factor accounting for the amount of SCX events that were missed because a γ was not detected was determined and applied to this correction. If the detection efficiency for γs, ϵ_γ, is known, the probability of detecting only one γ is:

$$P_{1\gamma} = 2\epsilon_\gamma(1 - \epsilon_\gamma), \tag{4.6}$$

which is the probability of detecting either of the γs $(2\epsilon_\gamma)$ times the probability of not detecting any $(1 - \epsilon_\gamma)$. The probability to detect two γs is simply:

$$P_{2\gamma} = \epsilon_\gamma^2, \tag{4.7}$$

and the probability of detecting neither γ is

$$P_{0\gamma} = (1 - \epsilon_\gamma)^2. \tag{4.8}$$

The correction factor is then the probability of detecting neither γ, $P_{0\gamma}$, over the probability of detecting one or both of the γs, $P_{\geq 1\gamma}$, and is:

$$f_{SCX} = \frac{P_{0\gamma}}{P_{\geq 1\gamma}} = \frac{(1-\epsilon_\gamma)^2}{2\epsilon_\gamma(1-\epsilon_\gamma)+\epsilon_\gamma^2}. \tag{4.9}$$

Each of the detected particle multiplicity channels $XpYnZd$ has the SCX contamination subtracted in the following manner

$$\sigma_{XpYnZd} = \sigma^{0\gamma}_{XpYnZd} - f_{SCX}\sigma^{\geq 1\gamma}_{XpYnZd}. \tag{4.10}$$

For the LADS detector, the average gamma detection efficiency, ϵ_γ, was determined to be 27 ± 4 %, 27 ± 4%, and 29 ± 4% at 118, 162, and 239 MeV, respectively, leading to correction factors, f_{SCX}, of $1.14^{+0.32}_{-0.23}$, $1.14^{+0.32}_{-0.23}$, and $1.02^{+0.28}_{-0.20}$.

The above assumes that the two γs from the decay of the π^0 are not correlated. This, of course, is not the case, since the directions and energies of the two photons are kinematically linked. If, for example, one of the two photons goes down the beam pipe, the other is less likely to do so than if the two photons were not correlated. Since LADS covers nearly 4π steradians, the method is sufficiently accurate.

4.3.2 Target Density

The z-vertex cut applied in the first stage of the data analysis determined the active length of the target. Once this was known, the target density was simply a function of the pressure of the gas and its temperature. The pressure in the target cell was monitored by a high precision gas gauge, and the temperature was monitored at the upstream and downstream ends of the LADS detector as well as on the target cell itself. The uncertainty of the pressure measurement was 1%. Heat from the photo multiplier tubes caused a small temperature gradient within the active volume of the LADS detector, causing the temperature registered by the temperature gauges to vary by a few degrees. The temperature gradient contributed to a 1% uncertainty in the temperature measurement of the target. The target pressures used in this experiment were high enough to cause a deviation from the ideal gas law requiring a modification due to compressibility of the target gas. The modified gas law has the form:

$$PV = Z(P,T)nRT. \tag{4.11}$$

The compressibility factor $Z(P,T)$ used in this work was calculated from an interpolation from tables in *Encyclopedie des Gaz* [124]. The total uncertainty in the target density was 1%.

4.3.3 Determination of Uncertainties

As is typical of most experiments, arriving at a number to be used as a result is relatively easy. What is difficult is applying uncertainties to the measured value. This work is no exception to that rule. For most channels, statistical uncertainties were negligible and systematic uncertainties dominated, except in the channels which had very few counts. The sources of systematic uncertainties include not knowing the detection efficiency of the π^0 and of neutrons to better than about 4%, as well as failure of the PID identifying some protons as deuterons and vice versa.

4.3.3.1 SCX Subtraction Uncertainties

As stated earlier in this thesis, LADS was not 100% efficient at detecting photons from the decay of the π^0. In fact, the detection efficiency was closer to 30%. The gamma detection efficiency also was dependent upon the number of charged particles in the final state as well as on the incident energy of the pion beam. From the work of Rowntree [125] it was determined that the γ detection efficiency was 27 ± 4%, 27 ± 4%, and 29 ± 4% for incident pion energies of 118, 162, and 239 MeV. These led to the correction factors stated earlier of $1.14^{+0.32}_{-0.23}$, $1.14^{+0.32}_{-0.23}$, and $1.02^{+0.28}_{-0.20}$. To determine the effect that this uncertainty had on the detected multiplicities, the SCX subtraction was done on the data at the determined correction factor as well as the extremes. The deviation of this measurement from the mean for each multiplicity channel was taken as the uncertainty due to SCX subtraction uncertainty. This was an extremely minor effect, $\leq 1\%$, in the detected multiplicity channels.

4.3.3.2 Neutron Detection Efficiency and Uncertainty

Uncertainty in the neutron detection efficiency was a more significant and complicated matter. The neutron detection efficiency was a function of both neutron energy and neutron angle (see Figure 4-6) and could not be measured directly from the Xe data as a kinematically complete detected final state was required. Instead, earlier measurements of the neutron detection efficiency using the reaction $^4\mathrm{He}(\pi^+, pppn)$ were used.[126, 111] In this analysis, it was not only the detection efficiency that was important, but also how well the Monte Carlo(MC) simulation (described later) reproduced the neutron detection efficiency since the MC was used to extrapolate over unmeasured regions of phase space.

The average neutron detection efficiency was about 35% and the uncertainty was approximately 4% when taking into account the change in the energy dependence of the detection efficiency as well as the ability of the Monte Carlo to reproduce the neutron efficiency data. To determine how this affects the observed multiplicities, the cross section for each neutron multiplicity was determined using 35% efficiency. This determined cross section was then used to produce expected neutral multiplicities based on the limits of

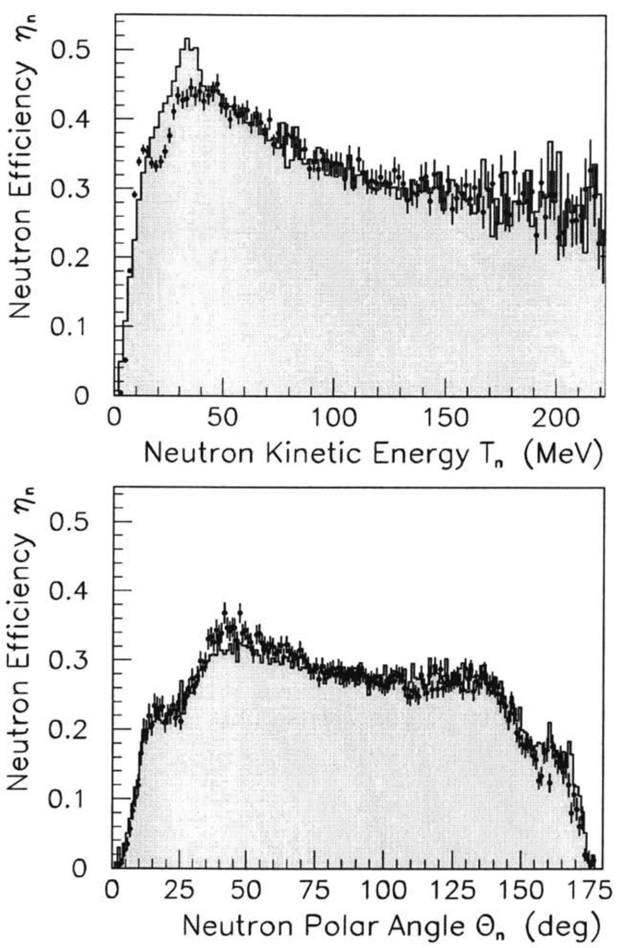

Figure 4-6: The energy and angular dependence of the neutron detection efficiency. From Lehmann *et al.* [110].

the neutron detection efficiency. The deviation of the values at the limits from the mean was taken as the uncertainty in the detected cross sections for each multiplicity caused by neutron detection efficiency.

As an example, consider a case where at most two neutrons were detected. The cross sections for the $XpYd2n$, $XpYd1n$, and $XpYd0n$ channels are given by:

$$\sigma_{XpYd2n} = \frac{N_{XpYd2n}}{\epsilon_n} \text{ , and } \sigma_{XpYd1n} = \frac{N_{XpYd1n}}{\epsilon_n} \text{ , and } \sigma_{XpYd0n} = N_{XpYd0n}, \tag{4.12}$$

where N_{XpYd2n}, N_{XpYd1n}, and N_{XpYd1n} are the number of events which are *produced* by the two-neutron, one-neutron and zero-neutron emission processes for various charge channels $XpYd$. Then, making the assumption that lower neutron multiplicities do not cause counts in higher neutron multiplicity channels, the number of *produced* events can be determined from the number of *observed* counts as follows: for the $XpYd2n$ channel,

$$N^{obs}_{XpYd2n} = N_{XpYd2n}. \tag{4.13}$$

For the $XpYd1n$ channel,

$$\begin{aligned} N^{obs}_{XpYd1n} &= N_{XpYd1n} + 2\epsilon_n(1-\epsilon_n)\cdot\sigma_{XpYd2n} \\ &= N_{XpYd1n} + 2\epsilon_n(1-\epsilon_n)\cdot\frac{N_{XpYd2n}}{\epsilon_n^2}, \end{aligned}$$

(4.14)

so using the results for $XpYd2n$,

$$N_{XpYd1n} = N^{obs}_{XpYd1n} - \frac{2\epsilon_n(1-\epsilon_n)}{\epsilon_n^2} \cdot N^{obs}_{XpYd2n}. \tag{4.15}$$

For the $XpYd0n$ channel,

$$\begin{aligned} N^{obs}_{XpYd1n} &= N_{XpYd0n} + (1-\epsilon_n)\sigma_{XpYd1n} + (1-\epsilon_n)^2\sigma_{XpYd2n} \qquad (4.16) \\ &= N_{XpYd0n} + \frac{(1-\epsilon_n)}{\epsilon_n} N_{XpYd1n} + \frac{(1-\epsilon_n)^2}{\epsilon_n^2} N_{XpYd2n}, \end{aligned}$$

which again using the above results gives the following,

$$\begin{aligned} N_{XpYd0n} &= N^{obs}_{XpYd1n} \\ &- \frac{(1-\epsilon_n)}{\epsilon_n}\left[N^{obs}_{XpYd1n} - \frac{2\epsilon_n(1-\epsilon_n)}{\epsilon_n^2} \cdot N^{obs}_{XpYd2n}\right] \qquad (4.17) \\ &- \frac{(1-\epsilon_n)^2}{\epsilon_n^2} N^{obs}_{XpYd2n}. \end{aligned}$$

The *detected* multiplicities are then recalculated using the calculated *production* multiplicities and the uncertainties in the neutron detection efficiency. The deviation about the mean of individual particle multiplicities was taken as the uncertainty caused by the neutron detection efficiency. The amount of uncertainty determined varied from the 2% level in the zero neutron channels to the 30% level in the channels with 3 or more neutrons. This behavior was typical for all three pion energies.

4.3.3.3 Proton/Deuteron PID uncertainty

The PID cuts used to identify charged particles were not 100% efficient. There were a certain number of protons which got misidentified as deuterons and vice versa. The Monte Carlo simulation indicated that about 1%-2% of the protons were identified incorrectly as deuterons, and about 2%-3% of the deuterons were incorrectly identified as protons. This was consistent with the mixing value of 2.7% determined by Rowntree[125] for pion absorption on light nuclei. Ideally, this misidentification was accounted for with the Monte Carlo simulation, but to be conservative, a mixing factor of 3% for both the deuterons and the protons was assumed. The data were then corrected for PID errors by subtracting the proton and/or deuteron contamination in one channel, and adding the contribution that this particular channel fed into others. The assumption was made that charged PID errors did not affect the neutral channels, so the correction was done for all channels that contributed to a particular $XcYn$ channel. An an example, the $2c0n$ channel was populated by the following final states $1p1d$, $2p$, and $2d$. In the $1p1d$ channel, there was contamination from the $2p$ channel as well as the $2d$ channel. These counts had to be removed from the $1p1d$ yield. In addition, the $1p1d$ channel contributed some counts to the $2p$ and the $2d$ channel which also had to be removed from those channels and reattributed to the $1p1d$ channel. This was done as follows

$$\begin{aligned} 1p1d' &= (1+\delta_d+\delta_p)1p1n - 2\delta_p 2p - 2\delta_d 2d && (4.18) \\ 2p' &= (1+2\delta_p+\delta_p^2)2p - \delta_d 1p1d - \delta_d^2 2d && (4.19) \\ 2d' &= (1+2\delta_d+\delta_d^2)2d - \delta_p 1p1d - \delta_p^2 2p && (4.20) \end{aligned}$$

where δ_d was the fractional deuteron PID error and δ_p was the fractional proton PID error. The difference between the "corrected" counts and the "uncorrected" counts was taken as the uncertainty. This effect contributed an uncertainty as high as about 50% in the $2d$ channels to about 20% in the $1d$ channels to about 5% in the $0d$ channels. This behavior was also consistent across the incident pion energies.

4.3.4 Experimentally Observed Multiplicities

With the total amount of beam on target measured, as well as knowing the target density, it was possible to determine the observed particle multiplicity cross sections. These are presented in tables 4.3 and 4.4 and are the non-acceptance corrected experimentally observed multiplicity cross sections with the requirement that outgoing particles have $>$ 30 MeV kinetic energy. The uncertainties described in this chapter lead to a total

Observed Multiplicity Cross Sections (mb)			
Experimental	Incident Energy		
Channel	118 MeV	162 MeV	239 MeV
1p1n	11.7 ± 1.0	16.5 ± 1.3	17.6 ± 1.2
1p2n	0.6 ± 0.3	1.2 ± 0.3	2.4 ± 0.4
1p3n	< 0.3	< 0.3	< 0.3
1p4n	< 0.3	< 0.3	< 0.3
1p1d	37.7 ± 7.0	45.0 ± 8.0	34.7 ± 6.7
1p1d1n	2.7 ± 0.6	5.6 ± 1.0	8.6 ± 1.5
1p1d2n	< 0.3	< 0.3	0.8 ± 0.3
1p1d3n	< 0.3	< 0.3	< 0.3
1p2d	0.6 ± 0.3	1.4 ± 0.5	2.2 ± 0.8
1p2d1n	< 0.3	< 0.3	0.3 ± 0.3
2p	151.3 ± 8.1	175.2 ± 9.5	143.2 ± 8.2
2p1n	10.7 ± 1.1	20.1 ± 2.0	30.2 ± 2.9
2p2n	0.3 ± 0.3	0.7 ± 0.3	2.4 ± 0.4
2p3n	< 0.3	< 0.3	< 0.3
2p4n	< 0.3	< 0.3	< 0.3
2p1d	3.9 ± 0.4	8.8 ± 0.8	13.4 ± 1.5
2p1d1n	< 0.3	0.5 ± 0.3	1.8 ± 0.3
2p1d2n	< 0.3	< 0.3	< 0.3
2p2d	< 0.3	< 0.3	0.3 ± 0.3

Table 4.3: (Part 1) The observed particle multiplicity cross sections. The total error in the values from normalization is not included. The uncertainties quoted are from statistics, from SCX subtraction, from neutron detection uncertainties, and from PID. These values are for a 30 MeV minimum energy threshold on the outgoing particles and have not been corrected to reflect the acceptance of LADS.

Observed Multiplicity Cross Sections (mb)			
Experimental Channel	Incident Energy		
	118 MeV	162 MeV	239 MeV
3p	7.7 ± 0.6	17.7 ± 1.3	28.5 ± 2.3
3p1n	< 0.3	0.9 ± 0.3	3.8 ± 0.4
3p2n	< 0.3	< 0.3	< 0.3
3p3n	< 0.3	< 0.3	< 0.3
3p1d	< 0.3	< 0.3	0.9 ± 0.3
3p1d1n	< 0.3	< 0.3	< 0.3
4p	< 0.3	< 0.3	1.1 ± 0.3
4p1n	< 0.3	< 0.3	< 0.3
4p2n	< 0.3	< 0.3	< 0.3
4p1d	< 0.3	< 0.3	< 0.3
5p	< 0.3	< 0.3	< 0.3
5p1n	< 0.3	< 0.3	< 0.3
1d1n	1.5 ± 0.3	2.3 ± 0.3	2.6 ± 0.3
1d2n	< 0.3	< 0.3	0.4 ± 0.3
2d	2.4 ± 1.1	3.0 ± 1.3	2.3 ± 1.0
2d1n	< 0.3	0.4 ± 0.3	0.6 ± 0.3
2n	< 0.3	0.3 ± 0.3	0.5 ± 0.3
total	231.6 ± 0.50	300.0 ± 1.0	299.6 ± 1.8

Table 4.4: (Part 2)The observed particle multiplicity cross sections. The uncertainty stemming from normalization is not included. The uncertainties quoted are from statistics, from SCX subtraction, from neutron detection efficiency, and from PID uncertainty. These values are for a 30 MeV minimum energy threshold on the outgoing particles and have not been corrected to reflect the acceptance of LADS.

normalization uncertainty of 22%, 19%, and 10% for incident pion energies of 118, 162 and 239 MeV, respectively, so all of the values in the table should be assumed to have such an uncertainty. The explicitly stated uncertainty includes statistical uncertainty, the uncertainty from the SCX subtraction, uncertainties in the neutron detection efficiency, and from PID. The values presented in the table were not corrected for the acceptance of the LADS detector and do not directly represent the underlying processes. In addition, the $1pXn$ and $1dXn$ channels are most certainly events with at least two charged particles where one or more was not detected by the ΔE counter. Later sections and chapters will describe how to obtain the underlying partial cross sections as well as the total absorption cross section corrected for detector acceptance.

Also determined were the charged multiplicity cross sections for 1, 2, 3, 4, and 5 charged particles in the final state and any number of neutral particles. These numbers were not as sensitive to SCX subtraction as the observed particle multiplicities and were unaffected by the neutron detection efficiency or PID errors and are presented in Table 4.5. The errors presented include the effects of SCX subtraction and statistical uncertainties.

Observed Multiplicity Cross Sections (mb)			
Charge Channel	Incident Energy		
	118 MeV	162 MeV	239 MeV
1*c*	13.9 ± 0.3	20.3 ± 0.3	23.1 ± 0.3
2*c*	205.5 ± 0.4	250.3 ± 0.8	223.1 ± 1.5
3*c*	12.4 ± 0.3	28.8 ± 0.3	50.3 ± 0.3
4*c*	< 0.3	0.5 ± 0.3	2.4 ± 0.3
5*c*	< 0.3	< 0.3	< 0.3

Table 4.5: The observed charged particle multiplicity cross sections. The values are the sums of the 1,2,3,4, and 5 charged particle channels. The error bars include SCX subtraction uncertainty and statistical uncertainty. The errors do not include normalization uncertainties.

4.4 Partial Cross Sections

One of the goals of this work is to determine the particle multiplicities of events which contribute to the total absorption cross section on Xe. The experimental multiplicities determined in the previous chapter do not correctly represent the underlying processes which contributed to the observed partial cross sections. To determine what the contributing partial cross sections are requires simulating the detector's response with numerous models of the underlying processes and fitting the results of the simulations to the observed partial cross sections. This section will explain the method used to extract the partial cross sections.

4.4.1 Monte Carlo Simulation

The LADS detector was modeled with a GEANT based simulation package developed by the LADS collaboration. The Monte Carlo simulation was designed to take the laboratory frame 4-vector values of particles from different event generators. The simulation code contained the best knowledge of the geometry of LADS, including the position and sectorization of materials in the cylinder and endcaps, the target cell materials, and the specific geometry of the MWPCs including the cathode strips and anode wires.

The LADS Monte Carlo simulation used events generated from an extended target and assumed a gaussian beam distribution. The simulation produced data files which were functionally identical to the data files produced by the experiment. The simulated data were then processed through the same analysis chain as the experimental data to determine the overall detector acceptance for a particular process as well as to determine how each modeled process filled the detected multiplicities. By processing the simulated data through the same analysis chain as the experimental data, various detector inefficiencies were folded into the determination of the acceptance. These inefficiencies included, but were not limited to, misreconstructed event vertices, MWPC inefficiency caused by crossing cathode strips, and losses due to non-ionizing reactions of the protons in the plastic scintillator.

4.4.2 Event Generators

Twenty seven different event generators were run through the simulation to model the processes that could have contributed to the detected particle multiplicities. These event generators include numerous phase space simulations of final states as well as semi-classical models of quasi-deuteron absorption (QDA) and QDA either preceded by πn or πp initial-state-interactions (ISI) or followed by pn or pp final-state-interactions (FSI). The phase space generators modeled events with the finals states of pd, pdn, $pdnn$, pdd, pp, ppn, $ppnn$, $ppnnn$, ppd, $ppdd$, $ppdn$, ppp, $pppn$, $pppnn$, $pppd$, $pppdn$, $pppp$, $ppppn$, $ppppp$, dd, and, ddn. In addition, QDA was modeled based on the parameterization of Ritchie[22]. Also modeled were πn-ISI-QDA and πp-ISI-QDA, where the initial elastic scattering of the pion was calculated with the phase shift code SCATPI[127] and QDA-pFSI and QDA-nFSI where the "hard" nucleon scattering was modeled as elastic scattering weighted with SAID[128]. In the FSI models, a minimum momentum transfer of 150 MeV/c was required and in all four cascade models the energy needed to remove the participating nucleons (Q-value) was included in the kinematics of the absorption step. All of the models had a weighting included to represent the spectator momentum. This weighting factor was

$$\exp[-0.5 * (P_{recoil}/\sqrt{3} * P_0)^2] \tag{4.21}$$

where P_{recoil} is the recoil momentum of the nucleus and P_0 reflects the width of the Fermi distribution. For this analysis, the value of P_0 was adjusted to 210 MeV/c in an attempt to reproduce the average missing momentum. Because the residual nucleus could also be left in an excited state, events were generated with a flat excitation energy distribution from 0 to 140, 180, and 200 MeV for incident pion energies of 118, 162 and 239 MeV, respectively. Figure 4-7 shows the missing energy and missing momentum spectra for the 3p detected channel. It was not possible to determine the optimum missing energy to better than ± 30 MeV. The missing energy could not be set arbitrarily high as the amount of energy left in the nucleus directly affects the acceptance for each generator. To account for this uncertainty, the simulations were run with missing energy values 30 MeV greater than and 30 MeV less than the optimum determined value. The fluctuations that this caused in the obtained fit parameters were used as the contribution from missing energy uncertainty to the partial cross section error bars.

The other uncertainty introduced directly by the Monte Carlo simulation came from the fact that the contribution from the cascade processes could only be roughly determined. For the QDA, *ppp*-ISI, *ppp*-FSI, *ppn*-ISI, and *ppp*-FSI event generators, there were enough kinematic structures to allow a simple fit to the kinetic energy and the polar angle distributions to roughly fix their amounts relative to others. For the 2p channel, the generators were the *pp*-phase space and the QDA model, for the 2pn channel, the generators were the *ppn*-phase space, *ppn*-ISI, and *ppn*-FSI models, and for the 3p channel, the

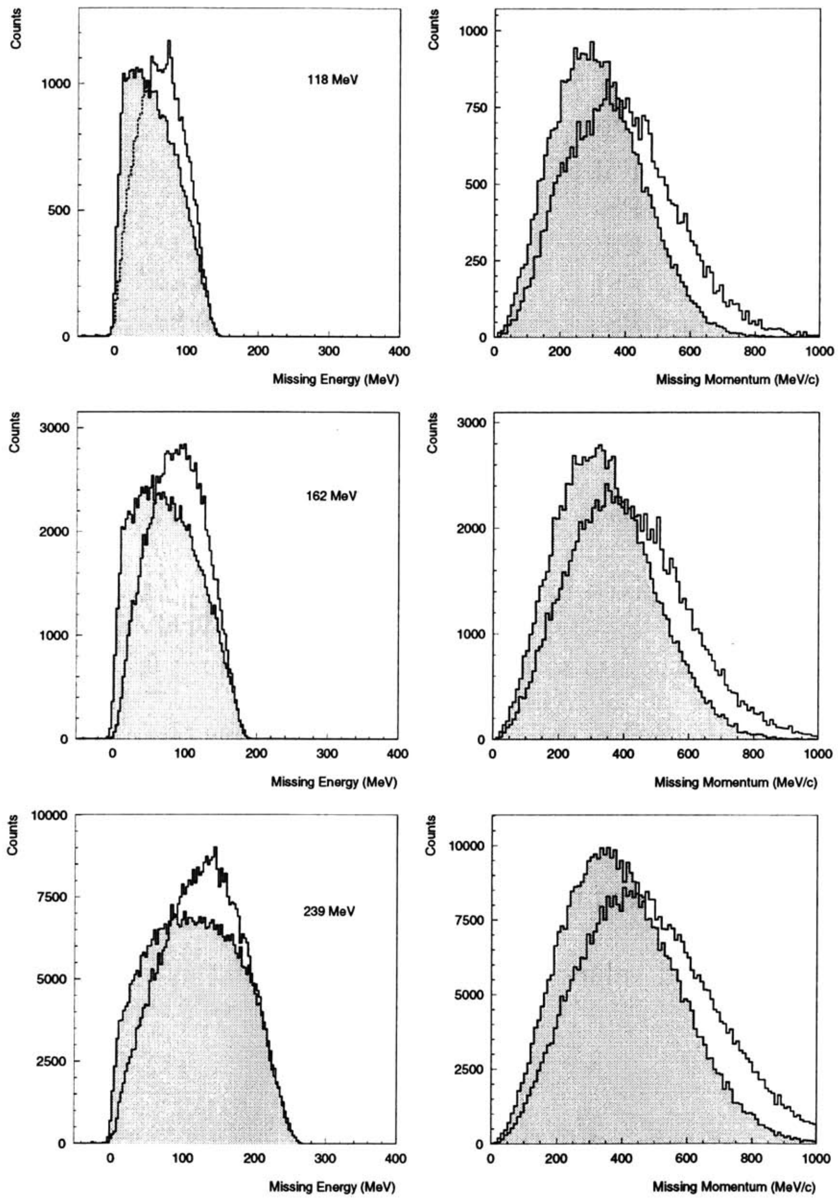

Figure 4-7: The missing energy and missing momentum for the detected $3p$ channel. The shaded portion is the sum of the Monte Carlo contributions.

Cascade Model Mixing Ratios			
Model	Incident Energy		
	118 MeV	162 MeV	239 MeV
QDA	0.5	0.8	0.8
2p PS	0.5	0.2	0.2
ppn ISI	0.0	0.0	0.0
ppn FSI	0.6	0.7	0.7
ppn PS	0.4	0.3	0.3
ppp ISI	0.0	0.0	0.4
ppp FSI	0.5	0.5	0.6
ppp PS	0.5	0.5	0.0

Table 4.6: The mixing of phase space and the cascade processes used in fitting the data.

generators were *ppp*-phase space, *ppp*-ISI and *ppp*-FSI. The relative proportions of these models to each other were fixed in their respective channels. The mixing fractions used are listed in Table 4.6. The fits to the observed experimental multiplicities determined the amount of each model that was required to reproduce the observed experimental multiplicity distributions. Because these mixing fractions could only be roughly determined, the fit was also run with only phase space generators as input. The difference between the two sets of determined values was included in the final uncertainty in the channels affected by this mixing.

4.4.3 Fits to the data.

The output of the Monte Carlo simulation was processed through the same analysis chain as the data applying the same cuts applied to the data to obtain "observed" multiplicities for each generator. These "observed" multiplicities were then fit, *via* a χ^2 minimization method, to the experimentally observed multiplicities. A sampling of the results is shown in Figures 4-8, 4-9, 4-10, 4-11. These figures show the measured kinetic energy and polar angle distributions for the three incident pion energies compared with the results of the Monte Carlo simulation. Figure 4-8 is for the $2p$ detected channel, Figure 4-9 the $2p1n$ detected channel, Figure 4-10 the $3p$ detected channel, and Figure 4-11 the $3p1n$ detected channel. In general the Monte Carlo reproduces these variables well with the exception that there is slightly greater experimental yield at the lower proton energies than the Monte Carlo predicts. The contributions from each model are summarized in Table 4.7 and are the partial cross sections extrapolated to 0 MeV.

The uncertainties in the fits do not include normalization uncertainties, but do include uncertainties coming from SCX subtraction uncertainties, neutron detection uncertainties, effects from PID errors and effects from modeling the data including missing energy and cascade model uncertainties. It was computationally impossible to run enough data to make MC uncertainties negligible so, to address Monte Carlo uncertainties coming from different random seeds, which governs how the multiplicities are distributed, the

Particle Multiplicity Cross Sections (mb)			
Model	Incident Energy		
	118 MeV	162 MeV	239 MeV
pd	44.9 ± 10.3	32.0 ± 9.6	14.3 ± 5.7
pdn	57.4 ± 11.8	75.4 ± 11.9	11.0 ± 10.0
pdnn	0.0 ± 2.1	9.8 ± 7.0	63.0 ± 17.5
pdd	4.0 ± 1.5	5.1 ± 1.9	1.3 ± 1.1
pddn	2.1 ± 1.0	6.6 ± 2.5	10.0 ± 3.4
pp	175.3 ± 15.5	143.3 ± 17.2	74.2 ± 12.0
ppn	224.5 ± 59.5	297.0 ± 58.2	154.6 ± 39.7
ppnn	< 0.3	26.7 ± 25.2	108.2 ± 24.4
ppnnn	< 0.3	< 0.3	15.6 ± 20.1
ppd	21.7 ± 2.1	28.0 ± 3.2	11.3 ± 2.9
ppdn	5.0 ± 6.0	32.5 ± 4.2	46.4 ± 6.4
ppdd	0.6 ± 0.3	1.8 ± 0.6	3.0 ± 0.8
ppp	41.4 ± 8.5	58.1 ± 10.7	37.1 ± 6.6
pppn	13.8 ± 2.6	42.4 ± 5.7	56.0 ± 6.8
pppnn	< 0.3	< 0.3	30.6 ± 9.8
pppd	< 0.3	5.1 ± 0.3	5.4 ± 0.4
pppdn	9.9 ± 10.9	1.0 ± 0.8	9.0 ± 1.5
pppp	1.3 ± 1.5	2.3 ± 0.7	5.5 ± 0.8
ppppn	1.0 ± 0.3	4.1 ± 0.7	11.4 ± 1.6
ppppp	0.1 ± 1.5	0.6 ± 0.7	0.4 ± 0.3
dd	2.5 ± 1.3	1.8 ± 1.1	< 0.3
ddn	3.7 ± 1.9	6.4 ± 2.8	5.0 ± 2.8

Table 4.7: The particle multiplicity cross sections determined from fits of the MC simulation to the experimental data. The values are the amount of each simulation that is necessary to reproduce the observed experimental multiplicities and are the partial cross sections extrapolated to 0 MeV particle detection threshold. The errors do not include normalization uncertainties.

Particle Multiplicity Cross Sections(mb) 239 MeV Incident Energy			
Model	Incident Energy		
	N	Ar	Xe
pd	1.2 ± 0.3	4.2 ± 1.0	14.3 ± 5.7
pdn	2.9 ± 1.0	10.6 ± 2.5	11.0 ± 10.0
pdnn	0.8 ± 1.0	6.0 ± 1.5	63.0 ± 17.5
pdd	-	0.7 ± 0.2	1.3 ± 1.1
pddn	1.3 ± 1.0	3.6 ± 1.0	10.0 ± 3.4
pp	23.6 ± 3.0	43.6 ± 5.2	74.2 ± 12.0
ppn	31.4 ± 6.1	75.0 ± 10.0	154.6 ± 39.7
ppnn	2.5 ± 1.2	21.0 ± 8.0	108.2 ± 24.4
ppnnn	-	0.0 ± 1.0	15.6 ± 20.1
ppd	4.1 ± 0.6	7.9 ± 1.5	11.3 ± 2.9
ppdn	6.0 ± 1.0	19.0 ± 4.0	46.4 ± 6.4
ppdd	1.7 ± 0.3	2.4 ± 0.5	2.9 ± 0.8
ppp	5.6 ± 1.7	28.4 ± 4.0	37.1 ± 6.6
pppn	3.1 ± 2.3	33.2 ± 7.5	56.0 ± 6.8
pppnn	0.6 ± 0.6	1.5 ± 1.7	30.6 ± 9.8
pppd	3.2 ± 0.4	5.5 ± 1.1	5.4 ± 0.4
pppdn	4.8 ± 1.0	6.3 ± 1.3	9.0 ± 1.5
pppp	2.3 ± 0.4	5.1 ± 1.0	5.5 ± 0.8
ppppn	4.0 ± 1.0	7.4 ± 1.8	11.4 ± 1.6
ppppp	0.33 ± 0.05	0.64 ± 0.13	0.4 ± 0.3
dd	-	0.0 ± 0.1	< 0.3
ddn	0.1 ± 0.1	0.9 ± 1.8	5.0 ± 2.8

Table 4.8: The particle multiplicity cross sections determined from fits of the MC simulation to the experimental data. The values are the amount of each simulation that is necessary to reproduce the observed experimental multiplicities and are the partial cross sections extrapolated to 0 MeV. The N and Ar data are from Kotlinski *et al.* [129].

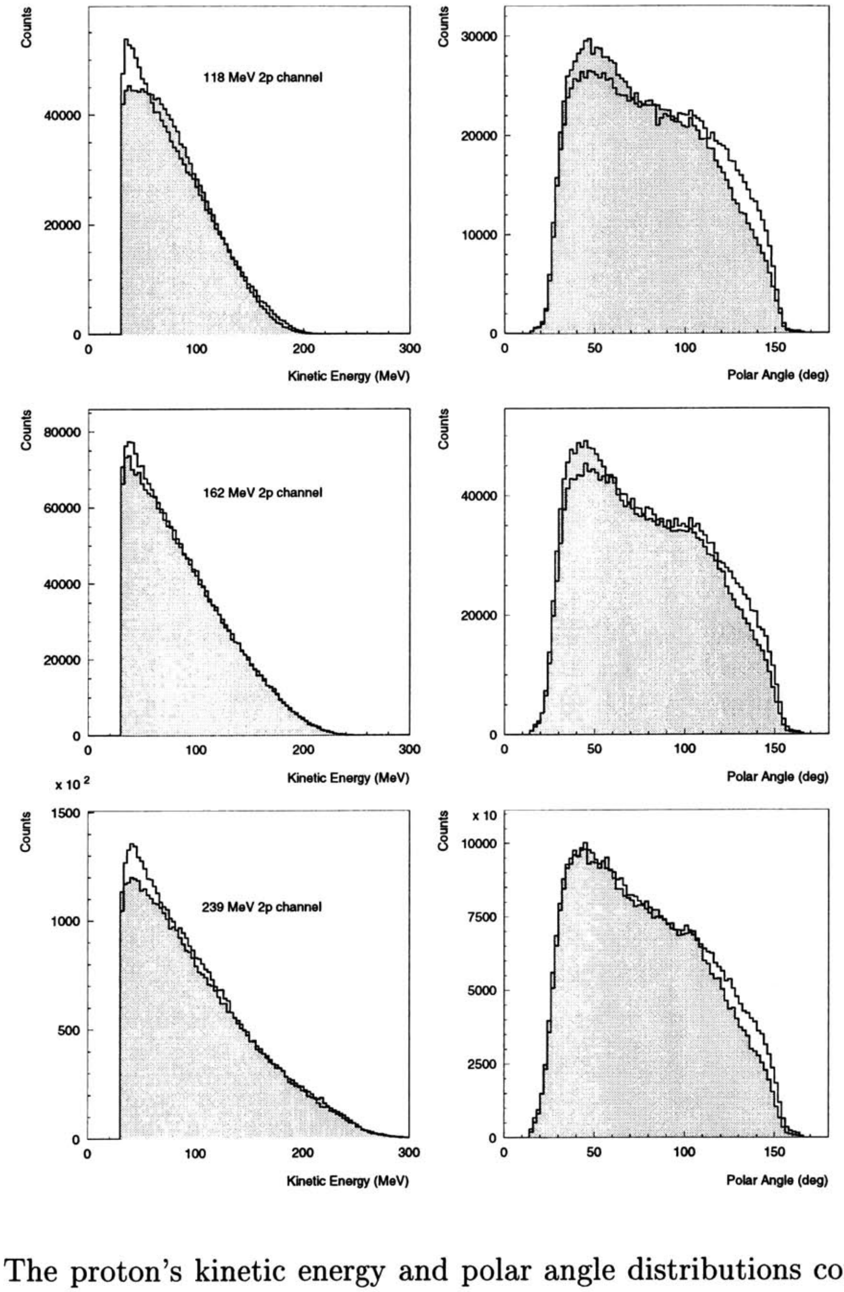

Figure 4-8: The proton's kinetic energy and polar angle distributions compared to the Monte Carlo simulation for the $2p$ detected channel. The shaded portion is the sum of the Monte Carlo contributions.

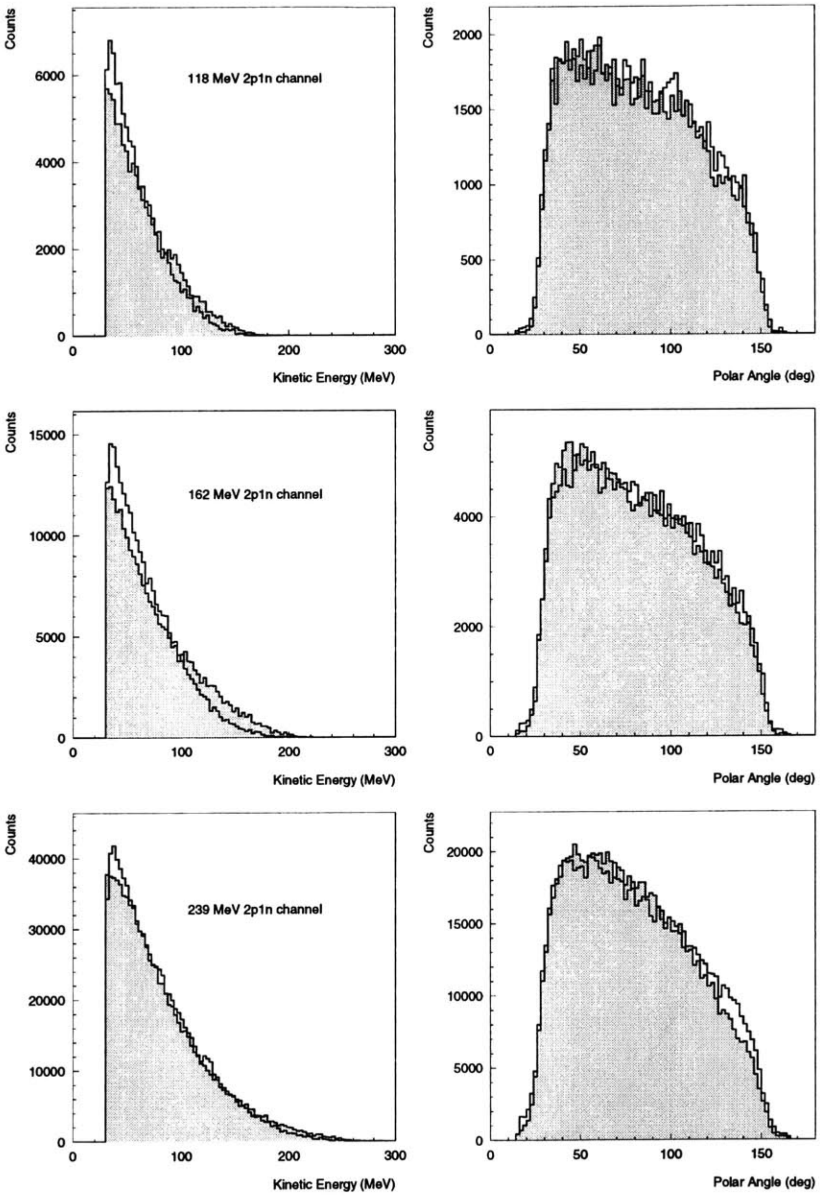

Figure 4-9: The proton's kinetic energy and polar angle distributions compared to the Monte Carlo simulation for the $2p1n$ detected channel. The shaded portion is the sum of the Monte Carlo contributions.

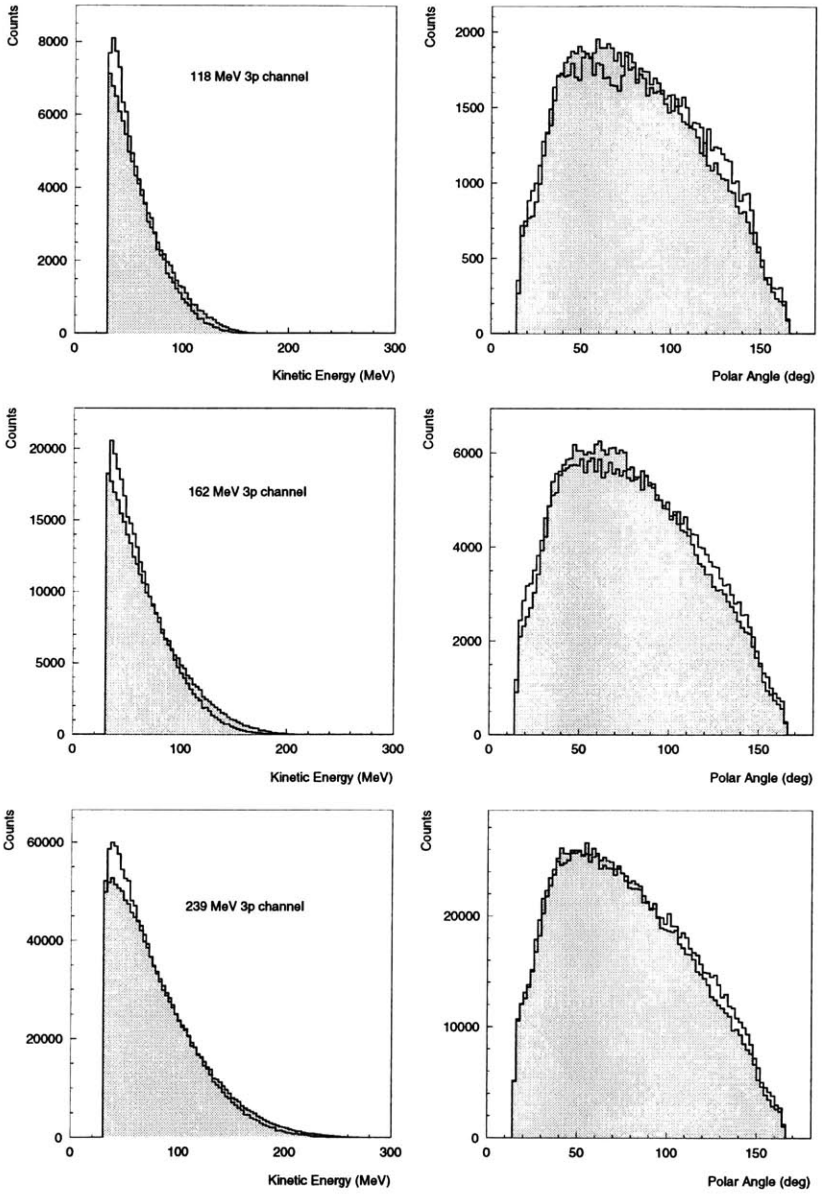

Figure 4-10: The proton's kinetic energy and polar angle distributions compared to the Monte Carlo simulation for the $3p$ detected channel. The shaded portion is the sum of the Monte Carlo contributions.

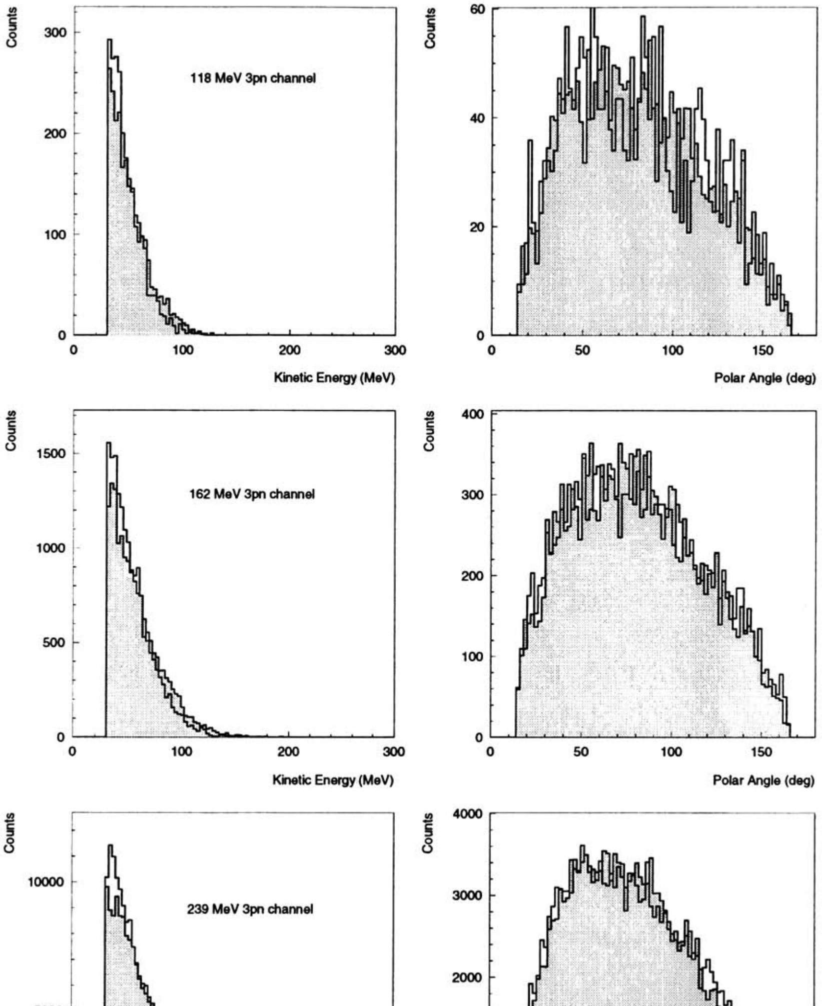

Figure 4-11: The proton's kinetic energy and polar angle distributions compared to the Monte Carlo simulation for the $3p1n$ detected channel. The shaded portion is the sum of the Monte Carlo contributions.

Charged Multiplicity Cross Sections (mb)			
Model	Incident Energy		
	118 MeV	162 MeV	239 MeV
$2c$	508.3 ± 53.2	592.1 ± 70.8	447.1 ± 38.9
$3c$	88.0 ± 2.7	172.6 ± 9.9	192.4 ± 8.6
$4c$	12.7 ± 10.0	14.6 ± 1.1	34.2 ± 1.3
$5c$	0.1 ± 1.5	0.3 ± 0.7	0.4 ± 0.3

Table 4.9: The charged multiplicity cross sections determined from fits of the MC simulation to the experimental data. The values are sums over the different charge channels of the fit and are the charged particle multiplity cross sections acceptance corrected and extrapolated to 0 MeV particle theshold. The errors do not include normalization uncertainties.

Monte Carlo simulation was run with different random seeds fed into GEANT. The results were averaged and reported as the cross section for each process. The deviation of the results is included in the uncertainties. Other simulation uncertainties were addressed in the PID uncertainty and the neutron detection efficiency uncertainty discussed earlier.

Also determined were the cross sections for charge multiplicities of 2, 3, 4, and 5 charged particles in the final state. These cross sections were somewhat less sensitive to the above uncertainties and are presented in Table 4.9. The uncertainties presented include fit, SCX, model and neutron detection uncertainties, but do not include overall normalization uncertainties.

Finally, the particle multiplicities were determined by summing the events which contained the same number of final state particles with deuterons being treated as a

Particle Multiplicity Cross Sections (mb)			
Particle Number	Incident Energy		
	118 MeV	162 MeV	239 MeV
2	224 ± 53	177 ± 39	88 ± 16
3	348 ± 110	470 ± 118	220 ± 54
4	28 ± 19	127 ± 46	298 ± 61
5	8 ± 11	6 ± 2	67 ± 30

Table 4.10: The particle multiplicity cross sections determined from fits of the MC simulation to the experimental data. The values are sums over the different channels with the same number of particles and are particle multiplicity cross sections acceptance corrected and extrapolated to 0 MeV particle threshold. The errors do not include normalization uncertainties.

single particle. The results from the Xe data are presented in Table 4.10. The 239 MeV data are compared with the Kotlinski *et al.*[129] results in Table 4.11. Again the uncertainties presented do not include normalization uncertainties.

Several trends are obvious in the results. One, the number of nucleons apparently involved in absorption increases with the incident pion's energy. Two, something odd, which is most likely a problem with this method of determining partial cross sections, is apparent at the highest incident pion energy. While at the lower energies the higher neutron multiplicity channels are small and consistent with zero contribution from $\geq$ $2n$ channels, at the highest energy this is no longer the case to the point where the $2n$ channel almost dominates. This is clearly bogus. Even though, with increasing pion energy, more phase space opens up for the $Xc2n$ channels, one clearly expects the $1n$ channels to have more strength. This behavior has also been seen in the very similar

Particle Multiplicity Cross Sections(mb)			
Particle Number	Target Nuclei		
	N	Ar	Xe
2	25	48	88 ± 16
3	54	124	220 ± 54
4	30	96	298 ± 61
5	9	16	67 ± 30

Table 4.11: The particle multiplicity cross sections determined from fits of the MC simulation to the experimental data. The values are sums over the different channels with the same number of particles and are particle multiplicity cross sections acceptance corrected and extrapolated to 0 MeV particle threshold. The N and Ar data are from Kotlinski *et al.* [129]. The errors do not include normalization uncertainties.

analysis of Kotlinski *et al.* and similar behavior has been seen in Ar, though not nearly as severely.[129] Three, while the vast majority of events come from the $2c$ channels, when combined with the particle multiplicity results indications are that events with neutrons in the final state comprise a significant portion of the total absorption cross section.

Earlier work with small and medium solid angle detectors on carbon was unclear on the processes which contributed to the detected cross section [88, 89, 113] to the point of self-contradiction. In fact, in Tacik *et al.*[113] the claim is that 3NA is not needed at all and that all of the absorption cross section comes from ISI-2NA and 4NA (defined as $3p1n$ and $4p$). While Xe is not carbon, significant strength was found in the 3 particle final states in this analysis at all energies, indicating disagreement with the conclusions of Tacik *et al.* The fact that the largest possible correction factor based upon detecting at least two charged particles in the final state from any of the generators is 10 from the *ppnnn* generator modeling the reaction for absorption of 118 pions, and most correction factors are on the order of 2 to 3, indicates even the most severe case here has less extrapolation uncertainties associated with it than the Tacik results which have correction factors of about 1000. Clearly, large solid angle studies are required to extract the underlying processes.

4.4.4 Comparison with Previous Large Solid Angle Measurements

Unfortunately, most of the early large solid angle studies did not attempt to extract the underlying processes [102, 104, 125, 130], although the work of Rowntree [125, 130] does attempt to make a complete and precise measurement of the observed partial and total absorption cross sections with minimal extrapolations over unmeasured regions of phase space.

It is possible to make some comparison to the previous large-solid-angle measurements of the partial cross sections which were done by the BGO-Ball collaboration and were presented in Ransome *et al.* [102] and Jones *et al.* [104] To compare with the BGO-Ball data, it was necessary to make adjustments to the partial cross sections on Xe. First and most importantly, the BGO-Ball results were presented in terms of $3p$ inclusive and $2p$ inclusive cross sections. An event was included in an Xp inclusive cross section if it had $\geq X$ protons, no identified pions and less than 2 neutral particles. There was no restriction placed upon deuterons, low energy charged particles or unidentified particles. The equivalent set of LADS events to the $3p$ inclusive for the partial cross sections presented here was *ppp*, *pppn*, *pppd*, *pppdn*, *pppp*, *ppppn*, *ppppp*. The $2p$ inclusive included everything in the $3p$ inclusive as well as *pp*, *ppn*, *ppd*, *ppdn*, *ppdd*. These partial cross sections were summed and compared with the BGO-Ball data. To make the comparison, two factors were applied. One was to adjust the cross section because the data were taken on different nuclei. This factor was $(A_{LADS}/A_{BGO})^n$ where n is the exponent in the power law fit described in Section 5.1. The other correction that was made was to account for the data not being taken at the same energy. This factor was taken from Figure 7 in Ashery *et al.*[78]. The inclusive cross sections as well as the multiplicative factor used to scale the LADS data are presented in Tables 4.12 and 4.13. The uncertainty in the BGO-Ball points was reported to be about 20%. Given the crudeness of the comparison, the agreement between the data sets is rather good, except at the lower energies (70, 118, 162 MeV) in the 3p inclusive cross section where the LADS results are 3 to 4 times larger than the BGO-Ball results. There are several factors which can contribute to the discrepancy, not the least of which is the scaling factor, since there is no reason to expect that the partial cross sections follow the behavior of the total absorption cross section. Another was the fact that neutral particles were treated differently by LADS and BGO-Ball. LADS was able to identify neutrons and γs as well as differentiate low energy γs caused by nuclear excitation from the high energy photons from the decay of a

3p Inclusive Cross Sections				
LADS			BGO-Ball	
Target/T_π(MeV)	Scaling	σ(mb)	Target/T_π(MeV)	σ(mb)
N/239	0.83	36 ± 3	N/250	25
Ar/70	0.96	12 ± 4	Ni/50	3.1
Ar/118	1.11	59 ± 10	Ni/100	12
Ar/162	1.28	120 ± 17	Ni/150	33
Ar/239	1.21	105 ± 11	Ni/250	99
Ar/330	1.80	106 ± 11	Ni/300	128
Xe/118	0.90	66 ± 23	Sn/100	12
Xe/162	0.92	114 ± 28	Sn/150	31
Xe/239	0.84	105 ± 17	Sn/250	112

Table 4.12: The 3p inclusive cross sections (described in the text) compared with the results of the BGO-Ball [102, 104]. The LADS data include this work (Xe) and that of Kotlinski *et al.* [129]. The LADS data are scaled by the scaling factor which is described in the text.

2p Inclusive Cross Sections				
LADS			BGO-Ball	
Target/T_π(MeV)	Scaling	σ(mb)	Target/T_π(MeV)	σ(mb)
N/239	0.83	91 ± 6	N/250	73
Ar/70	0.96	146 ± 25	Ni/50	100
Ar/118	1.11	309 ± 40	Ni/100	240
Ar/162	1.28	411 ± 40	Ni/150	300
Ar/239	1.21	283 ± 18	Ni/250	99
Ar/330	1.80	241 ± 17	Ni/300	310
Xe/118	0.90	494 ± 135	Sn/100	280
Xe/162	0.92	614 ± 145	Sn/150	320
Xe/239	0.84	344 ± 58	Sn/250	380

Table 4.13: The 2p inclusive cross sections (described in the text) compared with the results of the BGO-Ball [102, 104]. The LADS data include this work (Xe) and that of Kotlinski *et al.* [129]. The LADS data are scaled by the scaling factor which is described in the text.

neutral pion. The SCX contribution could therefore be subtracted, and the low energy γs from nuclear de-excitation ignored. BGO-Ball, on the other hand, could only tell that a neutral particle of some sort was present, so that while their yield contained SCX events, they rejected events with two or more low energy γs (from nuclear de-excitation) which were unrelated to the absorption process.

This thesis has attempted to determine, at some level, the processes that have contributed to the observed particle multiplicities. One limitation of this study is that most processes were modeled as phase-space. While cascade models were used also in channels where they were known to contribute, this analysis did not attempt to perform a detailed study of the contributions of the cascade processes and therefore nothing can be said regarding the amounts that were determined.

4.4.5 Average Number of Energetic Nucleons

Knowing what the 0 MeV particle multiplicities were, it was a simple matter to determine the average number of nucleons per event by summing over the partial cross sections times the number of nucleons in each channel using the following:

$$N_{avg} = \sum_{i=1}^{N_{chan}} \frac{N_i \cdot \sigma_i}{\sigma_{tot}} \tag{4.22}$$

Average Number of Nucleons per Event.			
	Incident Energy		
	118 MeV	162 MeV	239 MeV
Observed	2.3 ± 0.01	2.4 ± 0.01	2.6 ± 0.01
Fit	2.95 ± 0.03	3.23 ± 0.07	3.80 ± 0.1

Table 4.14: The average number of nucleons participating in a absorption event. The uncertainty in the observed quantity comes from propagation of the normalization uncertainty and from uncertainty in the SCX subtraction. The uncertainty in the fit values comes from flucuations observed from fits to different sets of simulations.

The results are summarized in Table 4.14 and presented in Figure 4-12. The rapidity analysis of McKeown *et al.* [75] observed from 2.5 to about 6 nucleons per absorption event increasing fairly strongly with atomic mass number. The reported results were averaged over the incident π^+ energies of 100, 160 and 220 MeV. One of the members of the LADS collaboration (Rowntree [125, 130]) performed an analysis of the A dependence of pion absorption in the Δ resonance region and determined much lower average numbers of nucleons per event for the incident pion energies of 118, 162 and 239 MeV [125, 130]. The Rowntree results also indicated that the average number of nucleons involved was not increasing nearly as rapidly with A as the results of McKeown *et al.* The results on Xe continue this trend although there seems to be a systematic shift to slightly higher average numbers of nucleons. This increase is likely due to the fact that events with one charged particle were excluded in the extrapolated partial cross section analysis. What is clear is that the results on Xe are not consistent with the number of nucleons participating as determined by McKeown *et al.* The results of McKeown *et al.* likely overestimate the

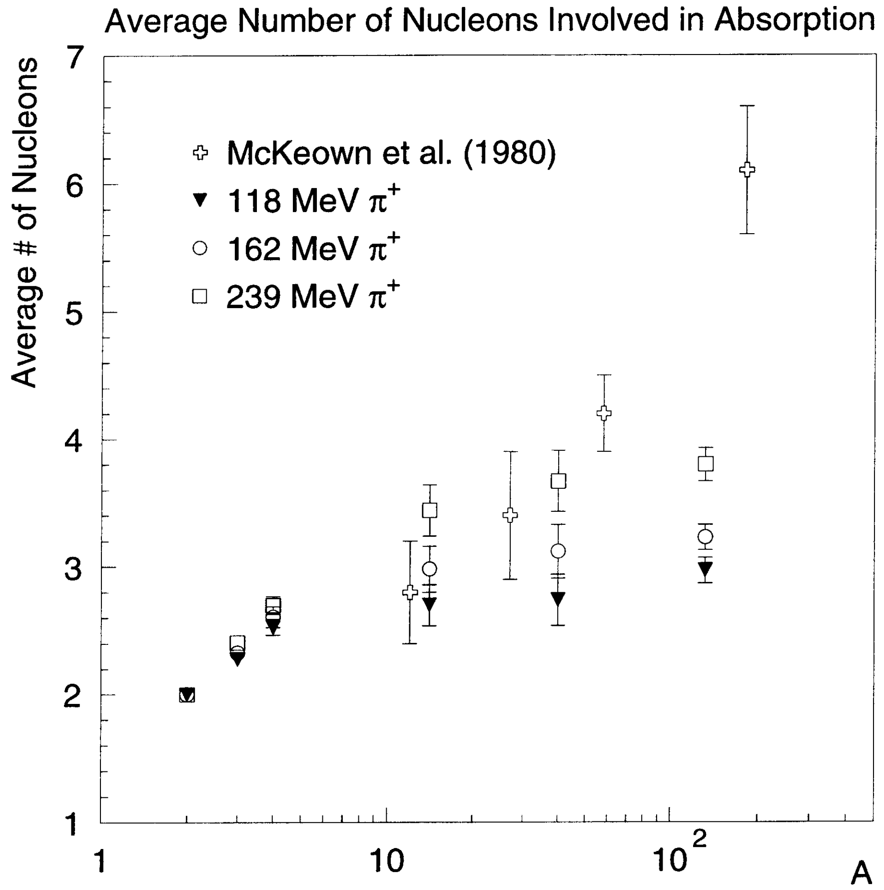

Figure 4-12: The average number of nucleons participating in an absorption event. The crosses are from [75]. The LADS points other than the Xe are from [125] and [130].

number of participating nucleons as the probability of an event being included in the data sample depended on the detection of a proton and will therefore increase with the number of final state protons. Thus, events with more protons in the final state will be weighted more strongly when calculating the average. The current results indicate that perhaps no special mechanisms are required to explain pion absorption. QDA followed by FSI could very likely be sufficient. Obviously, a problem is that as more nucleons get involved, it becomes more difficult to separate phase-space like processes, where all of the pion's energy is immediately shared with N nucleons, and cascade processes where N-nucleons are involved.

4.4.6 Partial Cross Sections – 30 MeV Threshold

Finally, I present the acceptance corrected cross sections. These are the partial cross sections corrected for the acceptance of LADS but not extrapolated to 0 MeV and which therefore have, in general, smaller uncertainties. This was accomplished by generating events from each of the simulated processes which only had a 30 MeV threshold on particle detection and no other detector or reconstruction code specific inefficiencies. The result of this generation was the ideal "observed" particle multiplicities for a 30 MeV requirement on the detected particle. These were not simply $3p$ events for the $3p$ generator, though. When a threshold was applied, some of the $3p$ channel fed into the $2p$ and $1p$ channels and similarly for other event generators. What this meant in computing the acceptance corrected/non-extrapolated partial cross sections was that all of the "observed" channels were somewhat intertwined. To extract the 30 MeV acceptance corrected partial cross sections, the "observed" channels were summed over all of the generators that contributed to each channel with weighting factors given by the parameters determined in the fits of the full Monte Carlo output to the data as follows:

$$\sigma_j = \sum_{i=1}^{N_{mod}} p_i \sigma_j^i, \tag{4.23}$$

where i is a particular generator (*e.g.* *pp*-QFA, *ppp*, *pd*), j is the observed channel (*e.g.* $2p$, $2pn$, $3p$), p_i is the parameter from the fit to 0 MeV threshold for a specific model i, and N_{mod} is the number of models used. The results are given in Tables 4.15 and 4.16

Partial Cross Sections (mb)(30 MeV threshold)			
Experimental Channel	Incident Energy		
	118 MeV	162 MeV	239 MeV
1p1d	55.7 ± 11.3	54.4 ± 11.8	25.4 ± 7.4
1p1d1n	17.8 ± 3.9	36.0 ± 6.3	34.5 ± 6.3
1p1d2n	< 0.3	1.0 ± 0.7	14.7 ± 4.1
1p2d	1.3 ± 0.5	2.6 ± 1.0	2.5 ± 1.0
1p2d1n	< 0.3	0.6 ± 0.3	2.3 ± 0.8
2p	228.7 ± 25.5	235.2 ± 31.5	131.8 ± 17.7
2p1n	66.6 ± 10.4	122.1 ± 13.6	138.9 ± 10.3
2p2n	< 0.3	2.9 ± 2.7	34.8 ± 8.5
2p3n	< 0.3	< 0.3	1.1 ± 1.5
2p1d	7.5 ± 0.7	14.9 ± 1.5	15.2 ± 2.1
2p1d1n	0.6 ± 0.3	3.3 ± 0.5	12.4 ± 1.8
2p2d	< 0.3	< 0.3	0.7 ± 0.2
3p	13.2 ± 1.2	26.4 ± 2.4	35.3 ± 4.2
3p1n	1.0 ± 0.3	5.2 ± 0.7	20.9 ± 2.3
3p2n	< 0.3	< 0.3	2.2 ± 0.8
3p1d	< 0.3	0.5 ± 0.3	1.7 ± 0.3
3pdn	< 0.3	< 0.3	0.6 ± 0.3
4p	< 0.3	0.4 ± 0.3	2.1 ± 0.3
4p1n	< 0.3	< 0.3	0.8 ± 0.3
5p	< 0.3	< 0.3	< 0.3
2d	3.4 ± 1.7	3.6 ± 1.8	1.2 ± 0.6
2dn	1.2 ± 0.6	2.8 ± 1.2	3.9 ± 1.9
totals	397.21 ± 27.37	512.00 ± 34.51	484.70 ± 19.56

Table 4.15: The partial cross sections for the pion absorption reaction on Xe at 118, 162, 239 MeV incident pion energy. The results are acceptance corrected and have a 30 MeV kinetic energy threhold. The uncertainties presented do not include normalization uncertainties.

Partial Cross Sections (mb)(30 MeV threshold)			
Experimental Channel	Incident Energy		
	N	Ar	Xe
1p1d	2.9 ± 0.6	9.8 ± 1.7	25.4 ± 7.4
1p1d1n	4.4 ± 1.0	13.0 ± 2.4	34.5 ± 6.3
1p1d2n	0.2 ± 1.0	1.6 ± 1.0	14.7 ± 4.2
1p2d	0.1 ± 0.1	1.3 ± 0.2	2.5 ± 1.1
1p2d1n	0.4 ± 1.0	0.9 ± 1.0	2.3 ± 0.8
2p	35.3 ± 2.8	72.9 ± 5.8	131.8 ± 17.7
2p1n	24.4 ± 2.5	62.9 ± 6.6	138.9 ± 10.3
2p2n	1.0 ± 1.0	5.6 ± 1.0	34.8 ± 8.5
2p3n	-	0.0 ± 1.0	1.1 ± 1.3
2p1d	5.5 ± 1.0	10.3 ± 1.2	15.2 ± 2.1
2p1d1n	3.2 ± 1.0	6.0 ± 1.0	12.4 ± 1.8
2p2d	0.6 ± 0.1	0.5 ± 0.1	0.7 ± 0.3
3p	15.2 ± 1.2	26.8 ± 2.5	35.3 ± 4.2
3p1n	6.8 ± 1.0	11.9 ± 1.3	20.9 ± 2.4
3p2n	0.1 ± 1.0	0.1 ± 1.0	2.2 ± 0.8
3p1d	1.5 ± 0.1	1.7 ± 0.2	1.7 ± 0.3
3pdn	0.6 ± 1.0	0.4 ± 1.0	0.6 ± 0.3
4p	1.3 ± 0.1	2.0 ± 0.2	2.1 ± 0.3
4p1n	0.5 ± 1.0	0.1 ± 1.0	0.8 ± 0.3
5p	0.035 ± 0.003	0.04 ± 0.01	< 0.3
2d	0.0 ± 0.3	0.4 ± 1.0	1.2 ± 0.6
2dn	0.2 ± 1.0	0.9 ± 1.8	3.9 ± 1.9
totals	106 ± 8	230 ± 28	484.70 ± 19.56

Table 4.16: The partial cross sections for the pion absorption reaction on N, Ar, and Xe 239 MeV incident pion energy. The results are acceptance corrected and have a 30 MeV kinetic energy threhold. The N and Ar data are from Kotlinski *et al.* [129].

Chapter 5

Total Absorption Cross Section

One of the advantages of performing an experiment that covers so much of phase space is that the extrapolations over unmeasured regions are relatively small. This enabled a reasonably precise measurement of the total absorption cross section somewhat independent of the imprecision of the measurement of the underlying processes. Unfortunately, the quality of the beam that impinged on the Xe target was somewhat poor which affected the normalization uncertainties rather severely. Nevertheless, a further refinement of the measurement of the behavior of the total absorption cross section with respect to the atomic mass number of the absorbing nucleus was still possible. The total absorption cross sections were determined by summing over the determined partial cross sections. The results are given in Table 5.1. The uncertainties stated include normalization uncertainties as well as the systematic uncertainties.

Total π^+ absorption cross sections on Xe	
Incident Energy	Cross Section (mb)
118 MeV	602 ± 140
162 MeV	772 ± 150
239 MeV	668 ± 70

Table 5.1: The pion total absorption cross section for incident pion energies of 118, 162 and 239 MeV.

5.1 Behavior of the Total Absorption Cross Section

Figure 5-1 shows the pion total absorption cross section on Xe at 118, 162, and 239 MeV. Also plotted is the parameterization of the absorption of the pion on the deuteron by Ritchie [22], scaled by 2.2, 4.3, 15, 32, 75 for ^{3}He, ^{4}He, N, Ar, Xe respectively. The other total absorption cross section numbers are from measurements of the LADS collaboration [112, 109, 110, 125, 126, 131]. While for nuclei up to ^{4}He, the data follow the ^{2}H parameterization well, for heavier nuclei the deviation from this resonance behavior is obvious. This is not unexpected if pion absorption is dominated by the formation of a Δ, since in nuclei with higher A it is more likely for the pion to lose energy to processes such as ISI. If the pion starts above resonance, it can still scatter off nucleons in the nucleus many times and not fall below the peak of the absorption cross section. Also possible are the opening up of other absorption channels such as 3NA or 4NA, although Smith *et al.* [93], Mukhopadhyay *et al.* [94], and earlier results of the LADS collaboration [105, 106]

Energy Dependence of Exponent n				
Incident Energy	Including ^{4}He		Excluding ^{4}He	
	σ_0 (mb)	n	σ_0 (mb)	n
118 MeV	20 ± 2.2	0.78 ± 0.04	43 ± 16	0.55 ± 0.13
162 MeV	18 ± 2.6	0.79 ± 0.05	26 ± 8	0.69 ± 0.11
239 MeV	7.9 ± 0.8	0.94 ± 0.03	8.3 ± 0.8	0.82 ± 0.08

Table 5.2: The scaling factor and exponent from a MINUIT fit of $\sigma_{abs} = \sigma_0 A^n$ to the measured total absorption cross section. The uncertainties are the parabolic errors reported by MINUIT.

on light nuclei demonstrated that the 3NA part of the pion absorption cross section had about the same resonance behavior as the 2NA portion.

Table 5.2 presents the results of fitting the Xe and other data from the LADS collaboration to the power law:

$$\sigma = \sigma_0 A^n. \tag{5.1}$$

From the earlier studies of pion absorption [69, 78] it was seen that for the heavier nuclei, pion absorption exhibits a power law behavior. In fact, this seems to be clear from Figures 5-2 to 5-4.

Earlier experimental work of pion absorption on nuclei indicated that near the energy region of the $\Delta(1232)$ resonance, the nucleus behaves like a black disk with the exponent of the power law being on the order of 2/3. This is not inconsistent with the current measurement. One thing to note is that the exponent is much closer to 1 for the 239 MeV

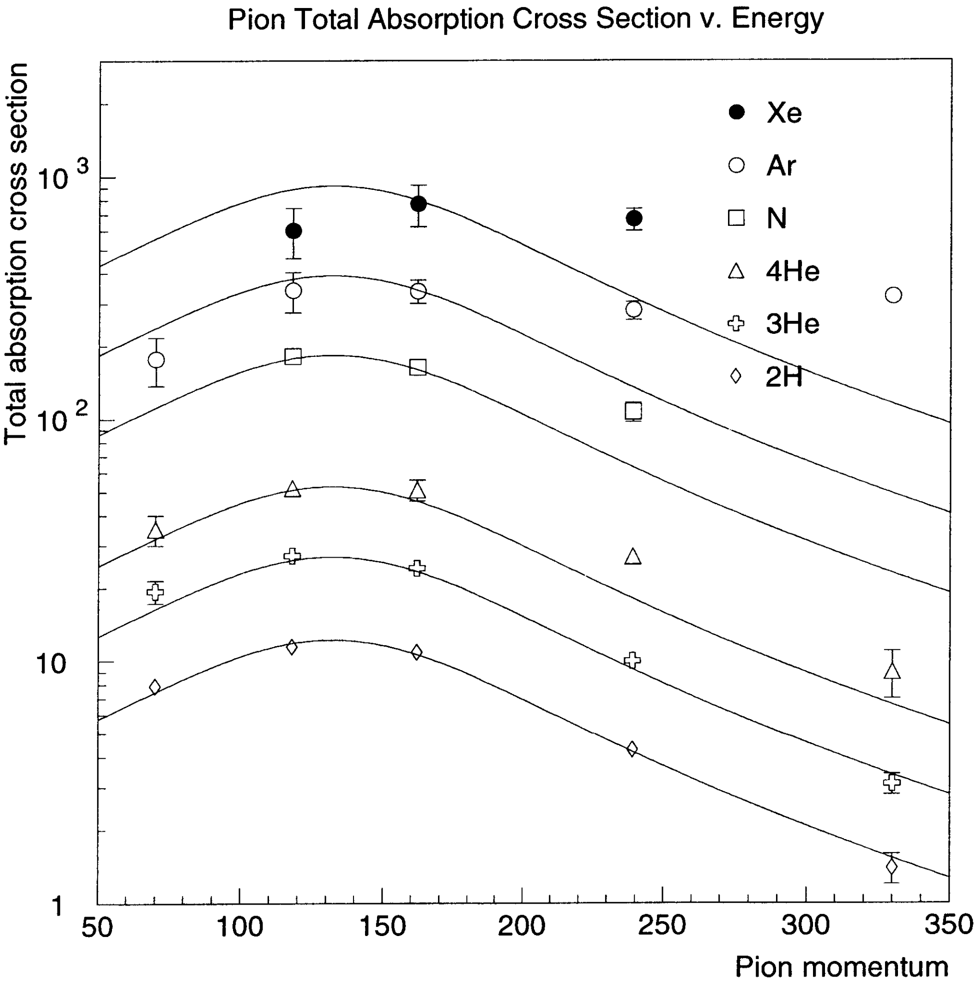

Figure 5-1: The pion total absorption cross section *vs.* incident pion energy. The other data are from LADS measurements. The curves are the Ritchie parameterization from [22].

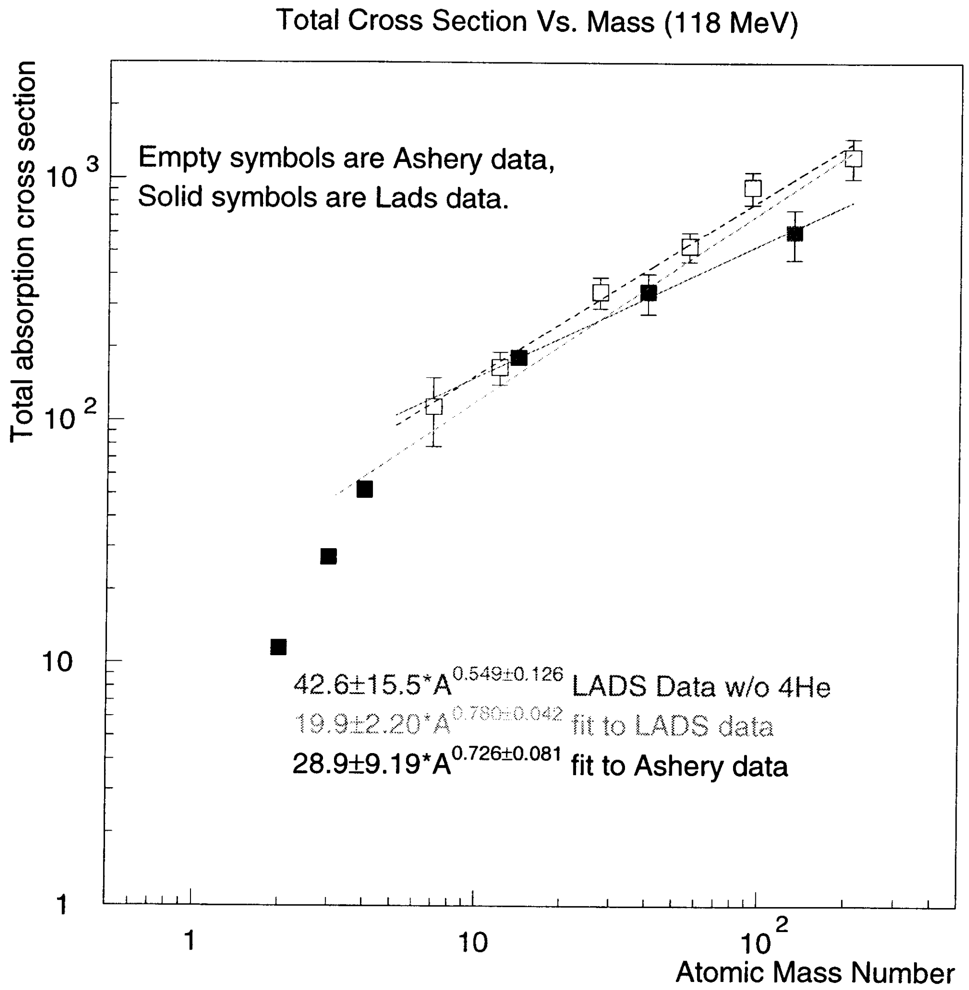

Figure 5-2: Total absorption cross section *vs.* A for $T_\pi = 118$ MeV. The solid squares are the data from the LADS collaboration, the open from Ashery *et al.*[78].

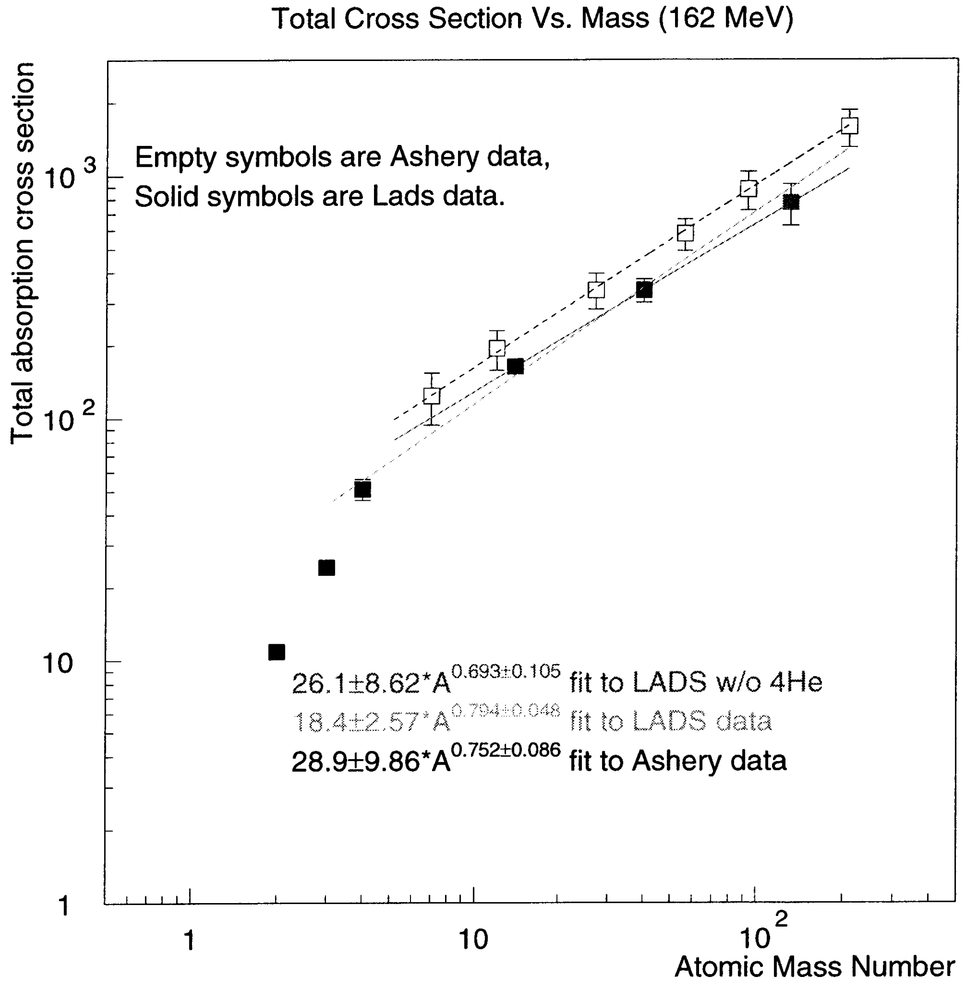

Figure 5-3: Total absorption cross section *vs.* A for $T_\pi = 162$ MeV. The solid squares are the data from the LADS collaboration, the open from Ashery *et al.*[78].

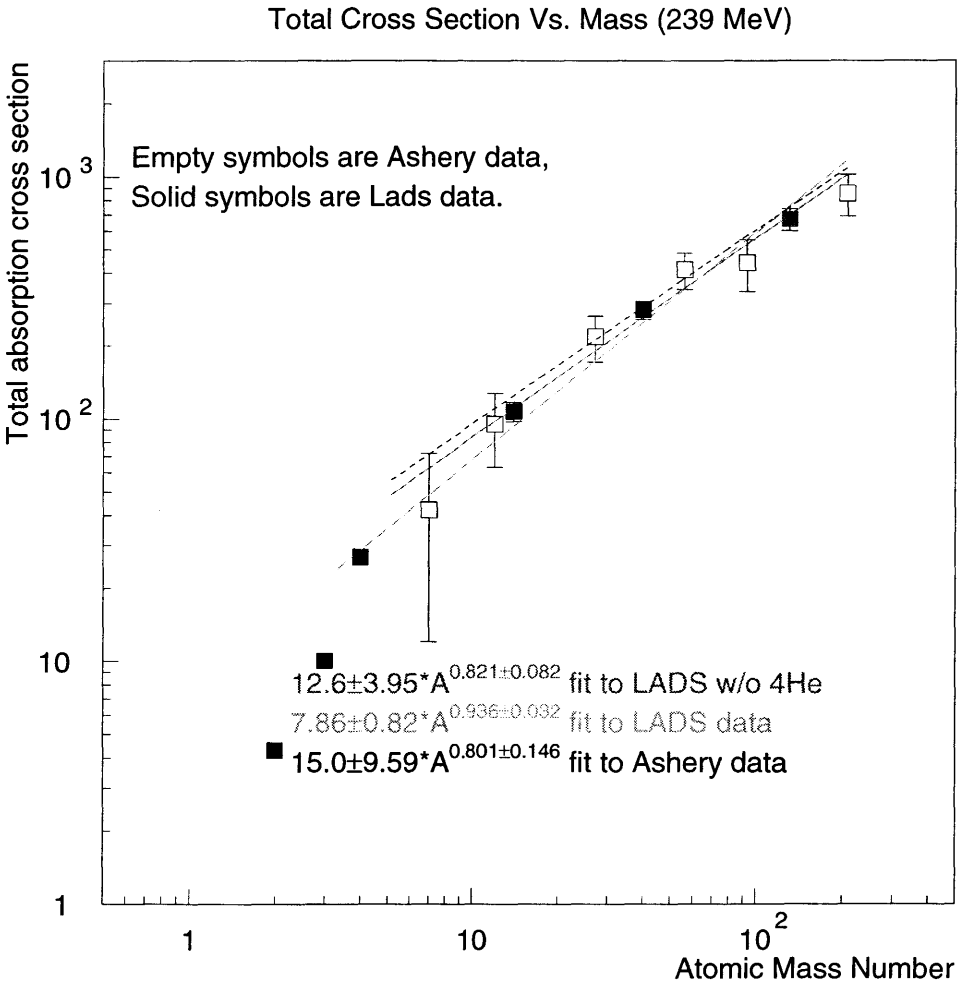

Figure 5-4: Total absorption cross section *vs.* A for $T_\pi = 239$ MeV. The solid squares are the data from the LADS collaboration, the open from Ashery *et al.*[78].

point. This indicates that the pion is much more penetrating when its energy is above the $\Delta(1232)$ resonance since an A dependence like $\sigma = \sigma_0 A^1$ would mean that the cross section is scaling like the number of nucleons and therefore the volume of the nucleus. Another feature of the exponent to notice is its energy dependence. The exponent is steadily increasing with incident pion energy indicating that more of the nucleus is being probed by the pion. This is in contrast to the results of Ashery *et al.* who found that except at pion energies below 100 MeV, the exponent was essentially constant. In addition, the SCX estimate used by Ashery *et al.* to extract the absorption cross sections was too small and led to an overestimation of the absorption cross sections, which meant that the Ashery *et al.* data could not be used to improve the fits to the power law.

Chapter 6

Summary and Conclusions

The total pion absorption cross section and the pion absorption partial cross sections have been measured on Xe. Also measured were the charge multiplicity cross sections and the average number of nucleons involved in an absorption event. Other than systematic error due to beam normalization, the total absorption measurement has been made to the 10% level demonstrating that this technique is more than adequate to perform a precision measurement of the total absorption cross section. The largest source of systematic uncertainty other than normalization comes from difficulty in modeling the excitation energy of the residual nucleus. Even a 25% uncertainty in determining the excitation energy at the lowest incident pion energy only causes a 10% uncertainty in the final cross section.

Trends in the partial cross sections can be investigated at least on the qualitative level also. For example, on Xe the pure 2p cross section drops from a level of 20% of the total absorption cross section at 118 MeV to 10% of the total absorption cross section at 239 MeV. The two particle partial cross section which includes the *pd* final state shows similar behavior, dropping from 40% of the total absorption cross section at 118 MeV to 15% of the total absorption cross section at 239 MeV. Similarly, events with 3 particles in the final state decrease in importance with increasing incident pion energy.

On the other hand, the 4 particle final states increase in importance in their contribution from 4.5% at 118 MeV to 45% at 239 MeV. The 5 particle partial cross section similarly increases from $\sim$ 1% at 118 MeV to 10% at 239 MeV. Whether the increase in the contributions of states with higher particle multiplicities is due to more phase space available for multiple cascade processes or from genuine multi-nucleon absorption modes cannot be determined.

When the Xe results at 239 MeV are compared with the N and Ar results of Kotlinski *et al.* [129] at this same energy, more conclusions about the partial cross sections can be made. The 2 particle final state fraction is essentially constant as a function of A. The 3 particle and 4 particle final state fractions also are roughly constant as a function of A.

The particle multiplicity partial cross sections indicate that at the higher incident pion energy, the final state multiplicities are becoming saturated even in nuclei as light as nitrogen. This could be a direct effect of nuclear shadowing and the mean free path of the pion in the nucleus and indicates that, even in nitrogen, the pion does not probe much more than the surface of the nucleus.

The average number of nucleons involved in an absorption event was determined much more precisely. In fact, despite not being able to determine the specific partial cross sections very well, the determined average number of nucleons was quite stable. The average number of nucleons in an absorption event is much lower than the trend suggested by McKeown *et al.*[75], and in fact the average number of nucleons produced in an absorption event seems to be approaching a limit, reflecting the apparent saturation of available final states discussed above. This work shows that there is significant 3 particle and 4 particle contribution to the total absorption cross section, although it is possible that some contribution could have come from FSI. With no clear kinematic signatures of FSI, it is not possible to separate a cascade FSI process from a genuine multi-nucleon absorption process.

While the total absorption cross sections determined in this analysis were affected by uncertainties due mainly to beam quality during the 1993 data run, useful information has been extracted. The analysis of the Xe data completed the LADS measurements of the absorption cross sections for pion energies in the region of the Δ resonance. There now exist measurements of the total and partial absorption cross sections on ^{2}H, ^{3}He,

^{4}He, N, Ar, and Xe, and these are the only pion absorption measurements over this range of nuclei not requiring large extrapolations over unmeasured regions of phase space. This allowed for the behavior of the total absorption cross section with A to be investigated. It is seen that the LADS data indicates that the exponent in the power law behavior of the total absorption cross section is steadily increasing as the incident pion energy increases. This is in contrast to the results of Ashery *et al.* [78], who determined an exponent that was consistent with a constant value of about 0.8.

This work points to the difficulty of analyzing the heavy target data from LADS. The uncertainties in the extrapolated partial cross sections are sometimes as large as the determined values; nevertheless, it is still possible to make a reasonably precise total absorption cross section measurement. In fact, analyzing the heavy targets points to the need for large acceptance studies of pion absorption to extract information about the underlying processes. Small angle studies are simply not able to extract enough useful information about the absorption process. One difficulty in furthering the survey done by LADS is finding suitable targets to study.

The survey of pion absorption on nuclei by the LADS collaboration is now complete. High precision data are available from the light nuclei and good information from the heavy targets is also present. Hopefully the existence of the LADS data set will encourage further theoretical work on pion absorption.

Bibliography

[1] H. Yukawa. "On the Interaction of Elementary Particles I," *Proc. Phys. Math. Soc. Japan*, **17**, 48 (1935).

[2] C. Anderson and S. Neddermeyer. "Note on the Nature of Cosmic Ray Particles," *Phys. Rev.*, **51**, 884 (1937).

[3] C. Street and E. Stevenson. "Penetrating Corpuscular Component of the Cosmic Radiation," *Phys. Rev.*, **51**, 1005 (1937).

[4] C. Street and E. Stevenson. "New Evidence for the Existence of a Particle of Mass Intermediate between the Proton and Electron," *Phys. Rev.*, **52**, 1003 (1937).

[5] S. Tomonaga and G. Araki. "Effect of the Nuclear Coulomb Field on the Capture of Slow Mesons," *Phys. Rev.*, **58**, 90 (1940).

[6] M. Conversi, E.Pancini, and O.Piccioni. "On the Disintegration of Negative Mesons," *Phys. Rev.*, **71**, 209 (1947).

[7] C. Lattes, G. Occhialini, and C. Powell. "Observations on the Tracks of Slow Meson in Photographic Emulsions.," *Nature*, **159**, 694 (1947).

[8] R. Bjorkland, W. Crandall, B. Noyer, and H. York. "High Energy Photons from Proton-Nucleus Collisions," *Phys. Rev.*, **77**, 213 (1950).

[9] A. Carlson, J.E.Hooper, and D. King. "Nuclear Transmutations Produced by Cosmic-Ray Particles of Great Energy - Part V. The Neutral Meson," *Phil. Mag.*, **41**, 701 (1950).

[10] J. Steinberger, W. Panofsky, and J. Steller. "Evidence for the Production of Neutral Mesons by Photons," *Phys. Rev.*, **78**, 802 (1950).

[11] W. Barkas, F. Smith, and E. Gardner. "Meson to Proton Mass Ratios," *Phys. Rev.*, **82**, 102 (1952).

[12] W. Panofsky, R. Aamodt, and J. Hadley. "The Gamma-Ray Spectrum Resulting from Capture of Negative π-Mesons in Hydrogen and Deuterium.," *Phys. Rev.*, **81**, 565 (1951).

[13] B. Jeckelmann, P. Goudsmit, and H. Leisi. "The mass of the negative pion," *Phys. Lett.*, **B335**, 326 (1994).

[14] R. Plano, A. Prodall, N. Samios, M. Schwartz, and J. Steinberger. "Parity of the Neutral Pion," *Phys. Rev. Lett.*, **3**, 525 (1959).

[15] R. Marshak. "Meson Reactions in Hydrogen and Deuterium," *Phys. Rev.*, **82**, 313 (1951).

[16] W. B. Cheston. "On the Reactions $\pi^+ d \leftrightarrows p + p$," *Phys. Rev.*, **83**, 1118 (1951).

[17] D. Clark, A. Roberts, and R. Wilson. "Cross Section for the Reaction $\pi^+ d \rightarrow pp$ and the spin of the π^+ Meson," *Phys. Rev.*, **83**, 649 (1951).

[18] R. Durbin, H. Loar, and J. Steinberger. "The Spin of the Pion via the Reaction $\pi^+ + d \rightleftharpoons p + p$," *Phys. Rev.*, **83**, 646 (1951).

[19] E. Moniz. "Δ-Nucleus Interactions," *Nucl. Phys.*, **A354**, 535 (1981).

[20] M. Gell-Mann and K. Watson. "The Interactions Between π-mesons and Nucleons," *Ann. Rev. of Nuc. Sci.*, **4**, 219 (1954).

[21] B. Ritchie. "Parameterization of the total cross section for $\pi d \rightarrow pp$ below 330 MeV," *Phys. Rev.*, **C28**, 926 (1983).

[22] B. Ritchie. "Parameterization of the total cross section for $\pi d \rightarrow pp$ below 1 GeV," *Phys. Rev.*, **C44**, 533 (1991).

[23] R. Marshak. *Meson Physics*. McGraw-Hill, New York, 1952.

[24] D. Perkins. "Mechanisms of π-meson Disintegration," *Phil. Mag.*, **40**, 601 (1949).

[25] F. Adelman and S. Jones. "Stars in Photographic Emulsions Initiated by π^- Mesons," *Science*, **111**, 226 (1950).

[26] W. Cheston and L. Goldfarb. "Disintegration of Nuclei by π^--Mesons," *Phys. Rev.*, **78**, 683 (1950).

[27] M. Menon, Muirhead, and Rochat. "Nuclear Reactions Produced by Slow Negative π Mesons," *Phil. Mag.*, **41**, 583 (1950).

[28] F. Adelman. "Fast Protons from the Capture of π^- Mesons in Photographic Emulsions," *Phys.Rev.*, **85**, 249 (1952). Also Ph.D. Thesis, University of California, 1950.

[29] W. Crandall, K. Crowe, B. Moyer, W. Panofsky, R. Phillips, and D. Walker. "Analysis of Neutral meson Gamma-Ray Spectra from Carbon," *Phys. Rev.*, **83**, 771 (1952).

[30] G. Bernardini, E. Booth, L. Lederman, and J. Tinlot. "On the Nuclear Interaction of π^- Mesons in Nuclear Emulsions," *Phys. Rev.*, **82**, 105 (1951).

[31] G. Bernardini, E. Booth, and L. Lederman. "Nuclear Absorption of Negative Pi-Mesons at Different Energies," *Phys. Rev.*, **83**, 1075 (1951).

[32] G. Bernardini and F. Levy. "Capture and Scattering of π^+ Mesons," *Phys. Rev.*, **84**, 610 (1951).

[33] H. Bradner and B. Rankin. "Large Angle Scattering ad Stars Produced by π^- Mesons in Flight," *Phys. Rev.*, **81**, 649 (1951).

[34] D. Koltun. The Interaction of Pions with Nuclei. In M. Baranger and E. Vogt, editors, *Advances in Nuclear Physics, Vol. 3*, pages 71–192. Plenum Press, New York, 1969.

[35] H. Stadler. "Aborption of Positive Pions by Deuterium at 76 and 94 MeV," *Phys. Rev.*, **96**, 496 (1954).

[36] C. Cohn. "Nonradiative Absorption of Positive Pions by Deuterons at 118 MeV," *Phys. Rev.*, **105**, 1582 (1957).

[37] A. Sachs, H. Winck, and B. Wooten. "Interactions of 38- and 61-MeV Positive Pions in Deuterium," *Phys. Rev.*, **109**, 1733 (1958).

[38] B. Neganov and L. Parfenov. "Investigation of the $\pi^+ + d \rightarrow 2p$ reaction for 174=307 MeV π^+ Mesons," *JETP Sov. Phys.*, **7**, 528 (1958).

[39] M. Demeur, A. Huleux, and G. Vanderhaheghe. "Déintégrations des noyaux légers de l'emulsion nucléaire par des mésons π^- lents," *Nuovo Cimento*, **4**, 509 (1956).

[40] S. Azimov, U. Guliamov, E. Zamchalova, M. N. ans M.I. Podgoreskii, and A. Iuldashev. "Investigation of σ-stars Induced by Negative π-Mesons," *JETP Sov. Phys.*, **4**, 632 (1957).

[41] P. Ammiraju and L. Lederman. "A Diffisuion Chamber Study of Very Slow Mesons. IV Absorption of Pions in Light Nuclei," *Nuovo Cimento*, **4**, 283 (1956).

[42] P. Fedotov. "Absorption of Stopped π^- Mesons by Carbon Nuclei," *Sov. J. Nucl. Phys.*, **2**, 335 (1966).

[43] A. Barkow, C. Edmund, F. Penaranda, H. Kane, and Z. O'Friel. "The Energy Spectra of Neutrons from stopped π^- Interactions in Emulsions," *Nuovo Cimento*, **28**, 673 (1963).

[44] G. Campos Venuti, E. Knapp, V. Perez-Mendez, and W. Perkins. "The Absorption of Negative Pions by Complex Nuclei (Copper, Tin, and Lead)," *Nuovo Cimento*, **34**, 1446 (1964).

[45] H. Anderson, E. Hinks, C. Johnson, C. Rey, and A. Segar. "Energy Spectra of Neutrons Emitted Following π^- Capture in C, Al, Cd, Pb, and U," *Phys. Rev.*, **133**, B392 (1964).

[46] K. L. Couteur. "THe Evaporation Theory of Nuclear Disintegrations," *Proc. Phys. Soc.*, **A63**, 259 (1950).

[47] K. L. Couteur. "Statistical Fluctuations in Nuclear Evaporation," *Proc. Phys. Soc.*, **A65**, 718 (1952).

[48] P. Fowler. "π-mesons versus cancer," *Proc. Phys. Soc.*, **85**, 1051 (1965).

[49] M. Nordberg Jr., K. Kinsey, and R. Burman. "Two-Nucleon Emission Following Absorption of Stopped Negative Pions," *Phys. Rev.*, **165**, 1096 (1968).

[50] S. Ozaki, R. Weinstein, G. Glass, E. Loh, L. Neimala, and A. Wattenberg. "π^- Capture in COmplex Nuclei and Nuclear Pair Correlations," *Phys. Rev. Lett.*, **4**, 533 (1960).

[51] M. Balandin, O. Ivanov, V. Moiseenko, and G. Sokolov. "Absorption of 40-70 MeV $\pi^{\pm}$ Mesons by Carbon in a Propane Bubble Chamber," *JETP Sov. Phys.*, **19**, 279 (1964).

[52] B. Anafasev and V. Ostroumov. "The $N^{14}(\pi, 2p)3\alpha$ Reaction with 80 MeV π^{+} Mesons," *Sov. J. Nucl. Phys.*, **1**, 463 (1965).

[53] G. Charpak, G. Gregoire, L. Massonet, J. Saudinos, J. Favier, M. Gusakow, and M. Jean. "Study of Two-Hole States in Light Nuclei by means of $(\pi^{+}, 2p)$ Reactions," *Phys. Letters*, **16**, 54 (1965).

[54] G. Charpak, J. Favier, L. Massonet, and C. Zupancic. Nuclear Structure Effects in $(\pi^{+}, 2p)$ Reactions. In *Proc. International Phys. Conf - Gatlinburg 1966*, page 465, New York, 1967. Academic Press.

[55] J. Favier, T. Bressani, G. Charpak, L. Massonet, W. Meyerhof, and C. Zupancic. "Nuclear Structure Effects in $(\pi^{+}, 2p)$ Reactions," *Phys. Letters*, **25B**, 409 (1967).

[56] C. Zupancic. Interactions of Low-Energy Pions with Nuclei. In G. Alexander, editor, *High-Energy Physics and Nuclear Structure*, page 188. John Wiley and Sons, Ney York, 1967.

[57] R. Burman and M. Nordberg. "reaction $^{6}(\pi^{+}, pp)\mathrm{He}^{4}$ and $T = 1$ states in He^{4}," *Phys. Rev. Letters*, **21**, 229 (1968).

[58] H. Davies, H. Muirhead, and J. Woulds. "The reaction $(\pi^{-}, 2n)$ in ^{6}Li and ^{7}Li," *Nucl. Phys.*, **78**, 663 (1966).

[59] A. Vaisenberg, , E. Kolynova, and N. Rabin. "Mass Spectrum of Charged Particles Emitted in the Absorption of π-mesons by Photographic Emulsion Nuclei," *JETP Sov. Phys.*, **20**, 854 (1965).

[60] T. Witten, M. Blecher, and K. Gotow. "Single-Proton Emission Folowing Positive Pion Absorption in Carbon," *Phys. Rev.*, **174**, 1166 (1968).

[61] J. Hüfner. "Pions Interact with Nuclei," *Phys. Reports*, **21**, 1 (1975).

[62] J. Favier, J. Bressani, G. Charpak, L. Massonnet, W. Meyerhof, and Č. Zupančić. "The (π^{+},2p) Reaction in Light Nuclei," *Nucl. Phys.*, **A169**, 540 (1971).

[63] S. Treiman and C. Yang. "Tests of the Single-Pion Exchange Model," *Phys. Rev. Lett.*, **8**, 140 (1962).

[64] C. Lazard, J. Ballot, and J.Favier. "Theoretical Investigation of Pion Absorption on ^{4}He.," *Nuovo Cimento*, **A63**, 1001 (1969).

[65] V. Balashov, A. Boyarkina, and I. Rotter. "look up this cite.," *Nucl. Phys.*, page 417 (1964).

[66] T. Kopaleishvili, I. Machabeli, G. S. Gogsadze, and N. Krupennikova. "The Reaction (π^+, NN) and Two-Hole Excitation of Light Nuclei," *Sov. J. Nucl. Phys.*, **7**, 198 (1968).

[67] T. Kopaleishvili. "Absorption of moving $\pi^\pm$ Mesons by Light Nuclei with the Emission of Two Nucleons and Nuclear Structure," *Sov. J. Nucl. Phys.*, **4**, 382 (1967).

[68] E. Bellotti, D. Cavilla, and C. Matteuzzi. "Positive-Pion Absorption by C Nuclei at 130 MeV," *Nuovo Cimento*, **A18**, 75 (1973).

[69] H. Jackson, S. Kaufman, L. Meyer-Schützmeister, J. Schiffer, S. Tabor, S. Vigdor, J. Worthington, L. Rutlidge,Jr, R. Segel, R. Burman, P. Gram, and R. R. ans M.A. Yates. "Energetic charged particle yields induced by pions on complex nuclei," *Phys. Rev.*, **C16**, 730 (1977).

[70] C. Ingram. "Pion-Nucleus Interactions," *Nucl. Phys.*, **A374**, 319c (1982).

[71] R. Redwine. "Pion-Nucleus Interactions," *Nucl. Phys.*, **A434**, 239c (1985).

[72] D. Ashery and J. Schiffer. "Pion Absorption in Nuclei," *Ann. Rev. Nucl. and Part. Sci.*, **36**, 207 (1986).

[73] H. Weyer. "Pion Absorption in Light Nuclei," *Phys. Reports*, **195**, 295 (1990).

[74] T. Ericson and W. Weise. *Pions and Nuclei.* Clarendon Press, Oxford, 1988.

[75] R. McKeown. "How Many Nucleons are Involved in Pion Absorption in Nuclei?," *Phys. Rev. Lett.*, **44**, 1033 (1980).

[76] K. Nakai, T. Kobayashi, T. Numao, T. Shibata, J. Chiba, and K. Masuani. "Measurements of Cross Section for Pion Absorption by Nuclei," *Phys. Rev. Lett.*, **44**, 1446 (1980).

[77] I. Navon, E. Piasetzky, D. Ashery, A. Altman, G. Azuelos, F. Schlepütz, and H. Walter. "True Absorption and Scattering of Pions on ^{16}O and ^{18}O," *Phys. Lett.*, **95B**, 365 (1980).

[78] D. Ashery, I. Navon, G. Azuelos, H. Walter, H. Pfeiffer, and F. Schlepütz. "True Absorption and Scattering of Pions on Nuclei," *Phys. Rev.*, **C23**, 2173 (1981).

[79] D. Gotta, M. Dörr, W. Fetscher, G. Schmidt, H. Ullrich, G. Backenstoss, W. Kowald, I. Schwanner, and H. Weyer. "Kinematically Complete Measurment of the Absorption of Stopped Pions in ^{3}He," *Phys. Lett.*, **112B**, 129 (1982).

[80] A. Altman, E. Piasetzky, J. Lichtenstadt, A. Yavin, D. Ashery, R. Powers, W. Bertl, L. Felawka, H. Walter, and R. W. amd J.v.d. Pluym. "Observation of a Quasideuteron Component in the Reaction $^{12}C(\pi^{+}.2p)$," *Phys. Rev. Lett.*, **50**, 1187 (1983).

[81] A. Altman, D. Ashery, E. Piasetzky, J. Lichtenstadt, A. Yavin, W. Bertl, I. Felawka, H. Walter, R. Powers, R. Winters, and J. v.d. Pluym. "Isotopic Effects in the $(\pi^{+}, 2N)$ Reactions on ^{16}O and ^{18}0," *Phys. Lett.*, **144B**, 337 (1984).

[82] B. Ritchie, N. Chant, and P. Roos. "Role of pion absorption on quasi-deuterons in $^{12}C(\pi^{+}, 2p)$," *Phys. Rev.*, **C30**, 969 (1984).

[83] A. Altman, D. Ashery, E. Piasetzky, J. Lichtenstadt, A. Yavin, W. Bertl, I. Felawka, H. Walter, R. Powers, R. Winters, and J. v.d. Pluym. "$(\pi^{\pm}, 2N)$ reactions at 165 and 245 MeV," *Phys. Rev.*, **C34**, 1757 (1986).

[84] W. Burger, E. Beise, S. Gilad, R. Redwine, P. Roos, N. Chant, H. breuer, G. Ciangaru, J. Silk, G. Blanpied, B. Preedom, B. Ritchie, M. Blecher, K. Golow, D. Lee, and H. Ziock. "Reaction $^{58}Ni(\pi^{+}, 2p)$ at 160 MeV," *Phys. Rev. Lett.*, **57**, 58 (1986).

[85] W. Burger, E. Beise, S. Gilad, R. Redwine, P. Roos, N. Chant, H. breuer, G. Ciangaru, J. Silk, G. Blanpied, B. Preedom, B. Ritchie, M. Blecher, K. Golow, D. Lee, and H. Ziock. "Reaction $^{58}Ni(\pi^{+}, pp)$ at 160 MeV," *Phys. Rev.*, **C41**, 2215 (1990).

[86] S. Hyman, D. Mack, H. Breuer, N. Chant, F. Khazaie, B. Ritchie, P. Roos, J. Silk, P.-A. Amaudruz, T. S. Bauer, C. Ingram, G. Kyle, D. Renker, R. Chumacher, U. Sennhauser, and W. Burger. "$^{16}O(\pi^{+}, 2p)$ reaction at 165 MeV," *Phys. Rev.*, **C41**, R409 (1990).

[87] G. Backenstoss, M. Izycki, P. Salvisberg, P. Weber, H. Weyer, S. Cierjacks, S. Ljunfelt, H. Ullrich, M. Furić, and T. Petković. "Evidence for a Direct Three-Nucleon Pion-Absorption Process," *Phys. Rev. Lett.*, **55**, 2782 (1985).

[88] R. Tacik, E. Boschitz, W. Gyles, W. List, and C. Ottermann. "Measurement of three protons in coincidence following absorption of 228 MeV π^+ in carbon," *Phys. Rev.*, **C32**, 1335 (1985).

[89] R. Tacik, E. Boschitz, W. Gyles, W. List, C. Ottermann, M. W. ler, U. Wiedner, and R. Johnson. "Three nucleon pion absorption in Carbon," *Phys. Rev.*, **C40**, 256 (1989).

[90] H. Yokota, K. Nakyama, K. Ichimaru, Y. Takahata, F. Suekane, R. Chiba, K. Nakai, I. Arai, H. En'yo, S. Sasaki, T. Nagae, and M. Sekimoto. "Detueron emission from pion absorption at $T_\pi = 65$ MeV," *Phys. Lett.*, **B175**, 23 (1986).

[91] G. Backenstoss, M. Izycki, P. Salvisberg, M. Steinacher, P. Weber, H. Weyer, S. Cierjacks, R. B, H. Ullrich, M. Furić, T. Petković, and N. Simićević. "Observaton of a Quasifree Three-Nucleon-Absorption Mode of Pions in ^{4}He," *Phys. Rev. Lett.*, **59**, 767 (1987).

[92] G. Backenstoss, D. Brodbeck, M. Izycki, P. Salvisberg, M. Steinacher, P. Weber, H. Weyer, A. Hoffart, R. B, H. Ullrich, D. Bosnar, M. Furić, and T. Petković. "New Pion Absorption Modes Observed from Triple Coincidences in ^{4}He," *Phys. Rev. Lett.*, **60**, 463 (1988).

[93] L. Smith, R. Minehart, D. Ashery, E. Piasetsky, M. Moinester, I. Navon, D. Geesaman, J. Schiffer, G. Stephans, B. Zeidman, S. Levinson, S. Mukhopadhyay, R. Segel, B. Anderson, R. Madey, J. Watson, and R. Whitney. "Reaction ^{3}He(π^+,pp)p at $T_\pi = 350$ and 500 MeV," *Phys. Rev.*, **C40**, 1347 (1989).

[94] S. Mukhopadhyay, S. Levenson, R. Segel, G. Garino, D. Geesaman, J. Schiffer, G. Stephans, B. Seidman, E. Ungricht, H. jackson, R. Kowalczak, D. Ashery, E. Piasetsky, M. Moinester, I. Navon, L. Smith, R. Meinhart, G. Das, R. Whitney, R. Mckeown, B. Anderson, R. Madey, and J. Watson. "Pion absorption by ^{3}He atthe Δ-resonance energy," *Phys. Rev.*, **C43**, 957 (1991).

[95] D. Mack, P.G.Roos, N. Chant, S. Hyman, F. Khazaie, B. Ritchie, J. Silk, G. Kyle, P. Amaudruz, T. Bauer, C. Ingram, , D. Renker, R. Schumacher, U. Sennhauser, and W. Burger. "Dominance of the two-nucleon mechanism in ^{16}O(π^+,pp) at 115 MeV," *Phys. Rev.*, **C45**, 1767 (1992).

[96] B. Rzehorz, G. Backenstoss, M. Džemidžić, M. Furić, A. Hoffart, T. Petković, H. Ullrich, H. Weyer, D. Weiser, and M. Wildi. "Evidence for pion absorption on four nucleons," *EuroPhys. Lett.*, **34**, 103 (1996).

[97] W. Brückner, H. Döbbeling, P. Gugelot, F. Güttner, H. Kneis, S. Majewski, M. Nomachi, S. Paul, B. Povh, R. Ransome, T. Shibata, M. Treichel, T. Walcher, P. Amaudruz, T. Bauer, J. Domingo, R. Frey, Q. Ingram, H. Jantzen, G. Kyle, D. Renker, and R. Schumacher. "π^+ absorption on ^{12}C in the $\Delta(1232)$ region," *Nucl. Phys.*, **A469**, 617 (1987).

[98] F. Adimi, H. Breuer, B. Flanders, M. Khandaker, M. Khayat, P. Roos, D. Zhang, T. S. Bauer, J. Konijn, C. de Laat, G. Kyle, S. Mukhopadhyay, M. Wang, and R. Tacik. "Two-nucleon absorption of π^+ in ^{4}He at T_π =114 and 162 MeV," *Phys. Rev.*, **C45**, 2589 (1992).

[99] T. S. Bauer, R. Hamers, P. Boberg, H. Breuer, R. van Dantzig, F. Geerling, S. Hyman, J. Konijn, C. de Laat, Y. Lefevere, A. Taal, J. Visschers, and R. Ykema. "Pion absorption followed by multinucleon emission," *Phys. Rev.*, **C46**, R20 (1992).

[100] R. Ransome, C. Morris, V. Cupps, R. Fergerson, J. McGill, D. Waston, J. Zumbro, B. Ritchie, J. Comfort, J. Tinsley, R. Loveman, S. Dawson, A. Green, P. Gugelot, and C. F. Moore. "Charged-Particle Multiplicities following Pion Absorption on ^{6}Li," *Phys. Rev. Lett.*, **64**, 372 (1990).

[101] R. Ransome, C. Morris, V. Cupps, R. Fergerson, J. McGill, D. Waston, J. Zumbro, B. Ritchie, J. Comfort, J. Tinsley, R. Loveman, S. Dawson, A. Green, P. Gugelot, and C. F. Moore. "Systematics of pion absorption on ^{6}Li," *Phys. Rev.*, **C42**, 1500 (1990).

[102] R. Ransome, C. Morris, V. Cupps, R. Fergerson, J. McGill, D. Waston, J. Zumbro, B. Ritchie, J. Comfort, J. Tinsley, R. Loveman, S. Dawson, A. Green, P. Gugelot, and C. F. Moore. "Pion absorption in neavy nuclei," *Phys. Rev.*, **C45**, R506 (1992).

[103] R. Ransome, C. Morris, M. Jones, B. Ritchie, D. Watson, J. McGill, K. Pujara, D. Clayton, I. Brown, P. Campbell, and C. F. Moore. "Pion absorption in light nuclei," *Phys. Rev.*, **C46**, 273 (1992).

[104] M. Jones, R. Ransome, V. Cupps, R. Fergerson, C. Morris, J. McGill, J. Zumbro, J. Comfort, B. Ritchie, J. Tinsley, P. Gugelot, and C. F. Moore. "Pion absorption above the $\Delta(1232)$ resonance," *Phys. Rev.*, **C48**, 2800 (1993).

[105] T. Alteholz, D. Androić, G. Backenstoss, D. Bosnar, H. Breuer, A. Brković, H. Döbbeling, T. Dooling, W. Fong, M. Furić, P. Gram, N. Gregory, J. Haas, A. Hoffart, C. Ingram, A. Klein, K. Koch, J. Köhler, B. Kotliński, M. kroedel, G. Kyle, A. Lehmann, Z. Lin, G. mahl, A. Mateos, K. Michealian, S. Mukhopadhyay, T. Petković, R. Redwine, D. Rowntree, R. Schumacher, U. Sennhauser, N. Šimičević, F. Smit, G. van der Steenhoven, D. Tieger, R. Trezeciak, H. Ullrich, M. Wang, M. Wang, H. Weyer, M. Wildi, and K. Wilson. "Large-Solid-Angle Study of Pion Absorption on ^{3}He," *Phys. Rev. Lett.*, **73**, 1336 (1994).

[106] G. Backenstoss, D. Bosnar, H. Breuer, H. Döbbeling, T. Dooling, M. Furić, P. Gram, N. Gregory, A. Hoffart, C. Ingram, A. Klein, K. Koch, J. Köhler, B. Kotliński, M. Kroedel, G. Kyle, A. Lehmann, A. Mateos, K. Michealian, T. Petković, R. Redwine, D. Rowntree, U. Sennhauser, N. Šimičević, F. Smit, G. van der Steenhoven, D. Tieger, R. Trezeciak, H. Ullrich, M. Wang, M. Wang, H. Weyer, M. Wildi, and K. Wilson. "Contribution of initial state interactions to the three-nucleon absorption of pions by ^{3}He," *Phys. Lett*, **B379**, 60 (1996).

[107] J. Köhler. "Pion Absorption in Helium with the LADS detector," *Few-Body Sys. Suppl.* (1995). for the LADS collaboration.

[108] D. Androić, G. Backenstoss, D. Bosnar, H. Breuer, H. Döbbeling, T. Dooling, M. Furić, P. Gram, N. Gregory, A. Hoffart, C. Ingram, A. Klein, K. Koch, J. Köhler, B. Kotliński, M. Kroedel, G. Kyle, A. Lehmann, A. Mateos, K. Michealian, T. Petković, R. Redwine, D. Rowntree, U. Sennhauser, N. Šimičević, R. Trezeciak, H. Ullrich, M. Wang, M. Wang, H. Weyer, M. Wildi, and K. Wilson. "Evidence of initial state interaction in multinucleon pion absorption," *Phys. Rev.*, **C53**, R2591 (1996).

[109] B. Kotliński, D. Androić, G. Backenstoss, D. Bosnar, H. Breuer, H. Döbbeling, T. Dooling, M. Furić, P. Gram, N. Gregory, A. Hoffart, C. Ingram, A. Klein, K. Koch, J. Köhler, M. Kroedel, G. Kyle, A. Lehmann, A. Mateos, K. Michealian, T. Petković, M. Planinić, R. Redwine, D. Rowntree, U. Sennhauser, N. Šimičević, R. Trezeciak, H. Ullrich, H. Weyer, M. Wildi, and K. Wilson. "Initial State Interactionin the $(\pi^+, 3p)$ Reaction on N, Ar and Xe," *Eur. Phys. J.*, **A1**, 435 (1998).

[110] A. Lehmann, D. Androić, G. Backenstoss, D. Bosnar, H. Breuer, H. Döbbeling, T. Dooling, M. Furić, P. Gram, N. Gregory, A. Hoffart, C. Ingram, A. Klein, K. Koch, J. Köhler, B. Kotliński, M. Kroedel, G. Kyle, A. Mateos, K. Michealian, T. Petković, M. Planinić, R. Redwine, D. Rowntree, U. Sennhauser, N. Šimičević, R. Trezeciak, H. Ullrich, M. Wang, M. .Wang, H. Weyer, M. Wildi, and K. Wilson. "Pion absorption on ^{3}He and ^{4}He with emission of three energetic protons," *Phys. Rev.*, **C55**, 2931 (1997).

[111] A. Lehmann, D. Androić, G. Backenstoss, D. Bosnar, H. Breuer, H. Döbbeling, T. Dooling, M. Furić, P. Gram, N. Gregory, A. Hoffart, C. Ingram, A. Klein, K. Koch, J. Köhler, B. Kotliński, M. Kroedel, G. Kyle, A. Mateos, K. Michealian, T. Petković, M. Planinić, R. Redwine, D. Rowntree, U. Sennhauser, N. Šimičević, R. Trezeciak, H. Ullrich, M. Wang, M. .Wang, H. Weyer, M. Wildi, and K. Wilson. "Multinucleon pion absorption on ^{4}He into the pppn final state," *Phys. Rev.*, **C56**, 1872 (1997).

[112] A. Mateos, D. Androić, G. Backenstoss, D. Bosnar, H. Breuer, H. Döbbeling, T. Dooling, M. Furić, P. Gram, N. Gregory, A. Hoffart, Q. Ingram, A. Klein, K. Koch, J. Köhler, B. Kotliński, M. Kroedel, G. Kyle, A. Lehmann, K. Michealian, T. Petković, M. Planinić, R. Redwine, D. Rowntree, U. Sennhauser, N. Šimičević, R. Trezeciak, H. Ullrich, M. Wang, M. .Wang, H. Weyer, M. Wildi, and K. Wilson. "Multinucleon pion absorption on ^{4}He into the pppn final state," *Phys. Rev.*, **C56**, 1872 (1997).

[113] R. Tacik, F. F. amd E.L. Mathie, P. Amaudruz, J. Brack, L. Felawka, R. Meier, D. Ottewell, G. Smith, G. Hoffman, M. Kermani, S. McFarland, K. Raywood, M. Sevior, F. Bonutti, P. Camerini, F. Grion, R. Rui, and E. Gibson. "Pion Absorption in ^{12}C," *Phys. Rev.*, **C57**, 1295 (1998).

[114] Swiss Institure of Nuclear Science, *SIN Users Handbook*,(1981).

[115] J. Albanese et al. "The Sin High resolutions Pion Channel and Spectrometer," *Nuclear Instruments and Methods*, **158**, 363 (1979).

[116] R. Balisger et al. "Technical Aspects of the SIN Pion CHannel and Spectrometer," *Nuclear Instruments and Methods*, **157**, 247 (1978).

[117] Angst & Pfister, Thurgauerstr. 66, CH-8050, Zurich, Switzerland. Rohacell is PMMA – polymethylmethacrylat (Acrylglas).

[118] Stesalit AG, Kunstoffwerk, CH-Zuwill SO., Switzerland. Stesalit is material 4412FG.

[119] Bicron Corporation, 12345 Kinsman Road, Newbury, Ohio 44065.

[120] Dow Corning Corporation, Box 0994, Midland, Michigan, 48686. THe main compound of the silicone epoxy was Silicone Elastomer 184.

[121] Struck, Baeckerbarg, D-2000 Tangstedt/Hamburg. Phone: (04109)550, Fax: (04109) 5533.

[122] R. Madey, F. M. Waterman, A. R. Baldwin, J. N. Knudson, J. Carlson, and J. Rapaport. "The Response of NE-228A, NE-228, NE-224, and NE-102 Scintillators to Protons from 2.43 to 19.55 MeV," *Nucl. Inst. and Meth.*, **151**, 445 (1978).

[123] D. C. Carey, K. L. Brown, and C. Iselin. DECAY TURTLE (Trace Unlimited Rays Through Lumped Elements) A Computer Program for Simulating Charged Particle Beam Transport. Technical Report SLAC-246 UC-28, Stanford Linear Accelerator, 1982.

[124] L'Air Liquide (Firm). *Encyclopedie des Gaz.* Elsevier, Amsterdam and New York, 1976.

[125] D. Rowntree. *The A-dependence of Pion ABsorption in the Energy region of the* $\Delta(1232)$ *Resonance.* PhD thesis, Massachusetts Institute of Technology, 1995.

[126] A. Mateos. *Multi-Nucleon Pion Absorption on Helium on the Delta Resonance Region.* PhD thesis, Massachusetts Institute of Technology, 1995.

[127] J. B. Walter and G. A. Rebka, Jr. *SCATPI - A Subroutine for Calculating* πN *Cross Sections and Polarizations for Incident Pion Kinetic Energies Between 90 and 300 MeV.* Technical Report LA-7731-MS, Los Alamos National Laboratory, 1979.

[128] R. A. Arndt, J. M. Ford, and L. D. Roper. "Pion-Nucleon Partial-Wave Analysis to 1100 MeV," *Phys. Rev.*, **D32**, 1085 (1985).

[129] B. Kotliński, D. Androić, G. Backenstoss, D. Bosnar, H. Breuer, H. Döbbeling, T. Dooling, M. Furić, P. Gram, N. Gregory, A. Hoffart, Q. Ingram, A. Klein, K. Koch, J. Köhler, M. Kroedel, G. Kyle, A. Lehmann, A. Mateos, K. Michealian, T. Petković, M. Planinić, R. Redwine, D. Rowntree, U. Sennhauser, N. Šimičević, R. Trezeciak, H. Ullrich, M. Wang, M. .Wang, H. Weyer, M. Wildi, and K. Wilson. Pion Aborption Reaction on N, Ar and Xe. to be published.

[130] D. Rowntree, , D. Androić, G. Backenstoss, D. Bosnar, H. Breuer, H. Döbbeling, T. Dooling, M. Furić, P. Gram, N. Gregory, A. Hoffart, Q. Ingram, A. Klein, K. Koch, J. Köhler, B. Kotliński, M. Kroedel, G. Kyle, A. Lehmann, A. Mateos, K. Michealian, T. Petković, M. Planinić, R. Redwine, , U. Sennhauser, N. Šimičević, R. Trezeciak, H. Ullrich, M. Wang, M. .Wang, H. Weyer, M. Wildi, and K. Wilson. "π^+ Absorption on N and Ar," *Phys. Rev.* (1999). To be submitted for publication.

[131] K. Wilson. *Pion Absorption on* ^{3}*He.* PhD thesis, Massachusetts Institute of Technology, 1995.